

**Synthesis and Characterisation of Aerosolised  
MIF Inhibitors for the Treatment  
of Respiratory Disease**



**Trinity College Dublin**  
Coláiste na Tríonóide, Baile Átha Cliath  
The University of Dublin

**Mohammad Doroudian**

**14338612**

**Department of Clinical Medicine, School of Medicine,  
Trinity College Dublin.**

**Supervisor: Professor Seamas C. Donnelly**

**Co-supervisors: Doctor Ciaran O' Reilly**

**2019**



## Table of Contents

Declaration of Authorship .....	v
Acknowledgements .....	vi
Abstract.....	viii
Publications and Communications .....	xi
List of abbreviations.....	xii
<b>Chapter 1.....</b>	<b>1</b>
<b>Introduction .....</b>	<b>1</b>
1.1 Macrophage migration inhibitor factor (MIF).....	2
1.1.1 MIF from genome to protein .....	2
1.1.2 Signalling and function of MIF .....	4
1.1.3 MIF and airway diseases .....	6
1.1.4 The role of MIF in lung cancer .....	7
1.1.5 The enzymatic active site of MIF; a therapeutic target.....	9
1.2 Nanomedicine applications in the lung cancer .....	11
1.2.1 Nanodrug delivery systems .....	17
1.2.2 Nano polymer-based for drug delivery.....	21
1.2.3 PLGA-based nanoparticles as a drug delivery system .....	23
1.2.4 Nebulised PLGA nanodrug delivery system.....	25
1.3 Hypothesis and Aims of the Project.....	27
<b>Chapter 2.....</b>	<b>29</b>
<b>Materials &amp; Methods.....</b>	<b>29</b>
Chemical materials and reagents used in this study .....	30

The kits, instruments, and cells used in this study.....	32
2.1 Experimental design .....	33
2.2 Synthesis of the nanoparticles.....	34
2.3 Limulus amoebocyte lysate (LAL) assay.....	35
2.4 Transmission Electron Microscope (TEM) .....	35
2.5 Scanning Electron Microscope (SEM) .....	36
2.6 Nano tracking analysis (NTA).....	36
2.7 Dynamic Light Scattering (DLS).....	37
2.8 Drug loading, drug encapsulation, and yield efficiency.....	37
2.9 Stability of the nanoparticles in simulated lung fluids .....	38
2.10 Drug Release .....	39
2.11 Cell culture .....	40
2.12 High Content Screening (HCS).....	40
2.13 Lactate dehydrogenase assay (LDH assay).....	41
2.14 Cellular uptake of nanoparticles in the cells.....	42
2.15 Confocal microscopy .....	43
2.16 Colorimetric ferrozine-based assay .....	43
2.17 The nebuliser efficiency assay.....	44
2.18 Laser diffraction .....	45
2.19 Cascade Impactor.....	46
2.20 Human Breathing Simulator and Human mechanical ventilator.....	47
2.21 Generation of recombinant MIF (rMIF) .....	48
2.21.1 Agarose gel electrophoresis .....	50

2.21.2	Extraction and purification of human rMIF .....	50
2.21.3	Sodium dodecyl sulfate polyacrylamide gel electrophoresis .....	52
2.21.4	Endotoxin removal.....	53
2.21.5	BCA protein assay .....	53
2.21.6	Cell free tautomerase assay.....	53
2.22	TNF- $\alpha$ ELISA.....	54
2.23	MTT assay .....	55
2.24	Statistical analysis.....	55
<b>Chapter 3.....</b>		<b>56</b>
<b>Synthesis and characterisation of PLGA-SCD19 nanoparticles.....</b>		<b>56</b>
3.1	Introduction .....	57
3.2	Results .....	61
3.2.1	LPS free nanoparticles .....	61
3.2.2	Size and morphology of the nanoparticles.....	62
3.2.3	Nano tracking analysis (NTA) .....	63
3.2.4	Surface charge, drug loading efficiency, drug content, and yield efficiency.....	65
3.2.5	Effect of lung artificial fluids on PLGA-SCD19 nanoparticles.....	66
3.2.6	Drug releases profile.....	68
3.2.7	Biocompatibility .....	69
3.2.8	Toxicity.....	71
3.2.9	Internalisation of NPs in alveolar epithelial cells.....	73
3.3	Discussion.....	76

<b>Chapter 4 .....</b>	<b>81</b>
<b>Characterisation of aerosolised PLGA-SCD19 nanoparticles.....</b>	<b>81</b>
4.1 Introduction .....	82
4.2 Results.....	87
4.2.1 Optimisation of PLGA-SCD19 nanoparticles for the nebuliser.....	87
4.2.2 Regional aerosol deposition in the Next Generation Impactor (NGI)	
93	
4.2.3 Drug delivery efficiency; mechanical ventilator & human breathing	
simulators .....	95
4.2.4 Discussion .....	96
<b>Chapter 5 .....</b>	<b>99</b>
<b>Drug activity after packaging into the PLGA nanoparticles .....</b>	<b>99</b>
5.1 Introduction .....	100
5.2 Results.....	101
5.2.1 Expression and purification of human recombinant MIF (rMIF)...	101
5.2.2 Endotoxin removal and enzyme activity of purified rMIF.....	105
5.2.3 Inhibition of cell proliferation in Lewis lung carcinoma cells.....	108
5.3 Discussion .....	109
<b>Chapter 6 .....</b>	<b>112</b>
<b>Discussion .....</b>	<b>112</b>
<b>Chapter 7 .....</b>	<b>121</b>
<b>Bibliography.....</b>	<b>121</b>
Appendix.....	143

## Declaration of Authorship

I declare that this thesis has not been submitted as an exercise for a degree at this or any other university and it is entirely my own work.

I agree to deposit this thesis in the University's open access institutional repository or allow the library to do so on my behalf, subject to Irish Copyright Legislation and Trinity College Library conditions of use and acknowledgement.

-----

Mohammad Doroudian

## Acknowledgements

First and foremost, I would like to express my sincere appreciation to my supervisor Professor Seamas Donnelly for his support and guidance throughout this project. I have been extremely lucky to have Professor Donnelly as my supervisor who cared so much not only about the research but also motivated my thinking and provided a variety of opportunities for my career development. I am forever grateful to him for his support and guidance throughout this project, his contributions of time, knowledge and funding during this study. Thank you for this opportunity.

I am extremely grateful and indebted to my co-supervisors Dr. Ciaran O' Reilly for his inspiring suggestions and valuable advice not only for this study but also in many other fronts without which it would have been difficult to carry out this work.

Massive thanks to all my great friends and colleagues who supported me throughout this PhD, especially to Michelle, Aisling, Aoife, Andrew, Fergus and Joanna. I will be forever grateful for their help, advice and friendship during my time in TBSI. You were always there through the good times and bad. You have truly made this journey more beautiful. A special thanks to Leona, who inspired me during a difficult time when I needed words of encouragement. Leona, you don't even know how much your help meant to me. Thank you!

I would also like to thank all my friends in the Nanomedicine and Molecular Imaging Group in St. James's Hospital and in Physiology Department at Trinity College who have assisted me in all areas of my research. A special thanks to Kieran for his advice and endless enthusiasm.

Special thanks to all my family for their help and support, but especially my Mom who was always there to motivate and encourage me.

I also thank my wonderful twins; Mahta and Mahyar. You have made me stronger, better and more fulfilled than I could have ever imagined. I love you to the moon and back.

Last but not least my final thank you is to my better-half Mahdieh. You have been there for me through thick and thin, and I'm forever grateful to have you in my life. Here's to the next chapter.

Finally, I dedicate this to my Dad. Always loved, never forgotten, and forever missed.

## Abstract

The main focus of this PhD thesis was to investigate the synthesis and characterisation of an aerosolised poly lactic-co-glycolic acid (PLGA) nanodrug delivery system for MIF enzyme inhibitors to modulate the physiological activity of macrophage migration inhibitory factor (MIF) in pulmonary diseases, particularly lung cancer.

MIF is a pro-inflammatory mediator of the immune system that plays a substantial role in the overall inflammatory cascade, tumour growth, angiogenesis, and cancer progression. Recently, we have identified a novel drug candidate, SCD19, which showed convincing results in both *in vitro* and *in vivo* studies of lung cancer. Herein we report our work to maximise local delivery of MIF therapeutics directly to the lungs through the development of an aerosolised delivery system utilising state of the art nanoparticle-based drug delivery systems.

Aerosolised nanoparticle delivery systems to the lung represent a novel future therapeutic strategy for cancer and in particular lung cancer. The use of aerosolised PLGA nanodrug delivery systems has increased markedly due to numerous advantages of this biodegradable, nontoxic and FDA approved nanodrug delivery system.

Initially, we encapsulated SCD19 into PLGA nanospheres by employing single emulsion-solvent evaporation technique. Transmission electron microscopy (TEM) and scanning electron microscope (SEM) images of PLGA-SCD19 nanoparticles showed a uniform spherical shape with smooth surfaces. The average hydrodynamic size of the PLGA-SCD19 nanoparticles, as measured by using nanoparticle tracking analysis (NTA) were  $200 \pm 20$  nm without aggregation. The drug loading efficiency, yield efficiency, and the drug content were  $63 \pm 13\%$ ,  $66 \pm 4\%$ , and  $5.7 \pm 4\%$ , respectively, which were within the acceptable range. The nanoparticles were found to be stable in both artificial lung fluid and artificial lysosomal fluid.

For the internalisation study of the nanoparticles, we co-encapsulated iron oxide nanoparticles (magnetic nanoparticles (MNPs)) and SCD19 into PLGA nanoparticles to make PLGA-MNP-SCD19. Then, we carried out different methods to investigate the cellular uptake of the PLGA-MNP-SCD19, in all of which significant accumulations of nanoparticles occurred in the cells after overnight incubation. Biocompatibility and toxicity of the nanoformulation was evaluated with high content analysis and LDH assay. There was no attributable toxicity associated with the nanoparticles and they showed a high degree of biocompatibility in human A549, murine RAW 264.7, and LLC cell lines.

In this study, we established a collaboration with Aerogen Ltd, a company specialising in the production of aerosol drug delivery devices. Initially, we optimised our nanoformulation for Aerogen's vibrating mesh nebuliser to achieve maximum drug delivery within acceptable nebulisation times. The vibrating mesh nebuliser did not affect the size nor the volume of PLGA-SCD19 nanoparticles. Also, laser diffraction method showed that the nebulised nanoparticles had an acceptable volume mean diameter (VMD) with an optimal particle size distribution for deep lung deposition. This leads to improve treatment efficiency by allowing aerosols to access the small airways with minimum waste. Moreover, in our study, the regional deposition of the aerosol nanoparticles in a mechanical human respiratory tract model, resulted in high deposition (more than 70%) in the alveolar region of the lung model with very low deposition in upper respiratory tract. Further investigation was conducted to define drug delivery efficiency. In this study we achieved 23% and 14% drug delivery efficiency from the mechanical ventilator and the breathing simulator, respectively. However, previous studies of other compounds had shown a wide range of drug delivery efficiency (from 1% to 16%). Finally, we examined the ability of our aerosolised PLGA-SCD19 nanoparticles to reduce cell proliferation in a MIF-Induced cell growth *in vitro* model which resulted in a significant reduction of cell proliferation (\*\*\*) $p < 0.001$  in the selected cancer cells.

This study has demonstrated that the developed aerosolised nanodrug delivery system may provide a novel adjunctive agent for use with anticancer drugs in the treatment of patients with lung cancer and the data obtained from characterisation studies may contribute to future drug delivery research.

## Publications and Communications

### Peer reviewed publication

- Ciaran O'Reilly, Mohammad Doroudian, Leona Mawhinney, Seamas C Donnelly. Targeting MIF in Cancer: Therapeutic Strategies, Current Developments, and Future Opportunities. *Medicinal research reviews*. 2016;36(3):440-60.

### Oral presentation

- M. Doroudian, C. O'Reilly, K. Crosbie-Staunton, R. MacLoughlin, A. Prina-Mello, Y. Volkov, S. C. Donnelly. Good things come in small packages: An aerosolized delivery system for small molecule inhibitors of macrophage migration inhibitory factor. Irish Thoracic Society Annual Scientific Meeting. Dublin, Ireland 2016.
- M. Doroudian, F. E. Poynton, C. O'Reilly, K. Crosbie-Staunton, R. MacLoughlin, A. Prina-Mello, M. E. Armstrong, L. Mawhinney, A. Tynan, A. N. McElroy, A. O'Neill, Y. Volkov, S. C. Donnelly. Aerosolised nanodrug delivery system to inhibit Macrophage migration inhibitory factor in order to treat lung cancer. Irish Thoracic Society Annual Scientific Meeting. Limerick, Ireland 2017.

### Poster presentation

- M. Doroudian, C. O'Reilly, K. Crosbie-Staunton, R. MacLoughlin, A. Prina-Mello, Y. Volkov, S. C. Donnelly. Good things come in small packages: An aerosolised delivery system for small molecule inhibitors of macrophage migration inhibitory factor. Irish Thoracic Society Annual Scientific Meeting, Dublin, Ireland 2016.

## List of abbreviations

Ab	Absorbance
AKt	Protein kinase B
ANOVA	Analysis of variance
AP1	Activator protein 1
APSD	Aerodynamic particle size distribution
ARDS	Acute respiratory distress syndrome
BAD	Bcl-2-associated death promoter
BSA	Bovine serum albumin
CD14	Cluster of differentiation 14
CD44	Cluster of differentiation 44
CD74	Cluster of differentiation 74
CdSe	Cadmium selenide
COPD	Chronic obstructive pulmonary disease
COX-2	Cyclooxygenase-2
CREB	cAMP response element-binding protein
CV	Crystal violet
Cyclin D1	Cyclin-dependent kinase 1
dH <sub>2</sub> O	Deionised H <sub>2</sub> O
DL	Drug loading
DLS	Dynamic Light Scattering
DMEM	Dulbecco's modified eagle's medium
DMSO	Dimethyl sulfoxide
DNA	Deoxyribonucleic acid
<i>E. Coli</i>	<i>Escherichia coli</i>
ECACC	The European Collection of Authenticated Cell Cultures
ELISA	Enzyme-linked immunosorbent assay
EMA	European medicines agency
ERK	Extracellular signal-regulated kinases
ETS	E26 transformation-specific
FBS	Fetal Bovine Serum
FDA	US Food and Drug Administration
Foxo3a	Forkhead box O3
FPLC	Fast protein liquid chromatography
HCS	High content screening
HIF1- $\alpha$	Hypoxia-inducible factor 1-alpha
HPLC	High Performance Liquid Chromatography
ICU	Intensive care unit
IFN- $\alpha$	Interferon alpha
IL	Interleukin
ISO-1	(S,R)-3-(4-hydroxyphenyl)4,5-dihydro-5-isoxazole acetic acid methyl ester
IUPAC	International Union of Pure and Applied Chemistry

I $\kappa$ B	Inhibitor of NF- $\kappa$ B
JAB1	c-Jun activation domain-binding protein-1
kD	Kilodalton
LB	Luria Bertani
LDH	Lactate dehydrogenase
LLC	Lewis lung carcinoma cell
LN2	Liquid Nitrogen
LPS	Liposaccharide
MAPK	Mitogen-activated protein kinases
MIF	Macrophage migration factor
MMAD	Mass median aerodynamic diameter
MNPs	Magnetic nanoparticles
MTT	Thiazolyl Blue Tetrazolium Bromide
NF- $\kappa$ B	Nuclear factor kappa-light-chain-enhancer of activated B cells
NPs	Nanoparticles
NTA	Nanoparticle tracking analysis
OD	Optical density
PBS	Phosphate-buffered saline
PEG	Poly (ethylene glycol)
PFA	Paraformaldehyde
PI3K	Phosphatidylinositol-4,5-bisphosphate 3-kinase
PLA2	Phospholipase A2
PLGA	Poly (lactic-co-glycolic) acid
PMNs	Polymorphonuclear leukocytes
PSD	Particle-size distribution
PVA	Poly (vinyl alcohol)
QD	Quantum dots
SCD-19	3-(2'-methylphenyl)-isocoumarin
SEM	Scanning electron microscope
SPION	Superparamagnetic Iron Oxide Nanoparticle
TEM	Transmission electron microscopy
TLR4	Toll-like receptor 4
TNF- $\alpha$	Tumor necrosis factor alpha
TPK	Tyrosine protein kinases

## Units

°C	Degrees Celsius
Mg	Microgram
µg/mL	Micrograms per Millilitre
µL	Microliter
Mm	Micrometre
µM	Micromolar
G	Gram
KDa	Kilodalton
L	Liter
M	Molar
min	Minutes
mL	Millilitre
mV	Millivolts
Nm	Nanometre
nM	Nanomolar
v/v	Volume per Volume
w/v	Weight per Volume
EU/mL	Endotoxin units per Milliliter

# Chapter 1

## Introduction

---

## 1.1 Macrophage migration inhibitor factor (MIF)

Macrophage migration inhibitory factor is a key proinflammatory cytokine that was discovered in the early 1960s, as one of the first cytokines to be identified [1, 2]. MIF was originally discovered during studies of the delayed-type hypersensitivity reaction as a T-cell derived cytokine that suppresses the random movements of monocytes and macrophages, hence its name macrophage migration inhibitory factor [3]. However, MIF's biological function remained unclear until the cloning of human MIF complementary DNA (cDNA) in 1989 [4]. Four years later in 1993 its rediscovery as a pituitary-derived peptide released in response to endotoxin in mice was reported [5]. Subsequently, MIF has been shown to be constitutively produced and expressed by nearly all types of circulating immune cells including macrophages [6], monocytes [7], T and B lymphocytes [8], eosinophils [9], neutrophils [10], and polymorphonuclear neutrophils (PMNs) [11], as well as structural cells including epithelial and endothelial cells. MIF is also expressed by an extensive variety of tissues such as brain, liver, heart, kidney and lung [12].

### 1.1.1 MIF from genome to protein

The MIF gene, *MIF*, is located on human chromosome 22q11.2., that contains 3 exons and 2 introns and encodes a 115-amino acid [13]. The MIF promoter is GC-rich and has no TATA box [14]. Several sequences of GC in a promoter usually contributes to the constitutive expression pattern similar to other housekeeping genes [15]. In addition, the promoter contains several consensus binding sequences for transcription factors, including AP-1, NFκB, cAMP-response element-binding protein (CREB) [16], and hypoxia inducible factor-1α (HIF-1α) suggesting that the expression of MIF could be induced under specific conditions [17]. Recently, a polymorphism in the promoter region of human MIF has been reported which varies by the presence of a CATT-tetranucleotide microsatellite at position -794, that is repeated between 5 and 8 copies in the promoter (-794 CATT<sub>5-8</sub>). It has been well demonstrated that

expression of MIF is driven by this functional polymorphism presenting in approximately 49% of the population, with carriers of the 6-, 7- and 8-CATT repeat alleles being genetically primed to produce higher levels of MIF compared to those carrying the 5-CATT repeat allele [18]. Those patients genetically primed to produce significantly enhanced MIF have been shown to have a more aggressive clinical phenotype in such a variety of acute, chronic, inflammatory and cancer diseases [12, 19]. MIF is stored in pre-formed cytosolic pools within vesicles in the cytoplasm of cells allowing for rapid release in response to stressful stimulants such as TLR antigens, mitogens, and pro-inflammatory cytokines [2]. In a recent pancreatic cancer study, it was also observed that MIF can be transported via exosomes [20]. MIF is a small protein with a molecular weight of 12.5 kDa, the secondary structure of MIF consists of two antiparallel  $\alpha$ -helices and six  $\alpha$ -sheets, the three-dimensional X-ray crystallography studies of human revealed that MIF exists as a homotrimer (Figure 1.1 A) [21]. MIF is a highly conserved protein, for instance, all mammalian MIFs including human, mouse, rat and cattle have nearly 90% homology [22]. Unlike other cytokines, MIF possesses a unique enzyme activity which is ketol-enol tautomerase activity [23]. The enzymatic active site is located between each MIF's subunits so each homotrimer has three active sites. It has been shown that there is a direct correlation between MIF biological function and its enzyme activity [24, 25]. The enzyme activity of MIF catalyses the tautomerisation of the non-physiological substrates D-dopachrome and L-dopachrome methyl ester into their corresponding indole derivatives, however the physiological substrate for MIF remain undiscovered thus far (Figure 1.1 B) [23].

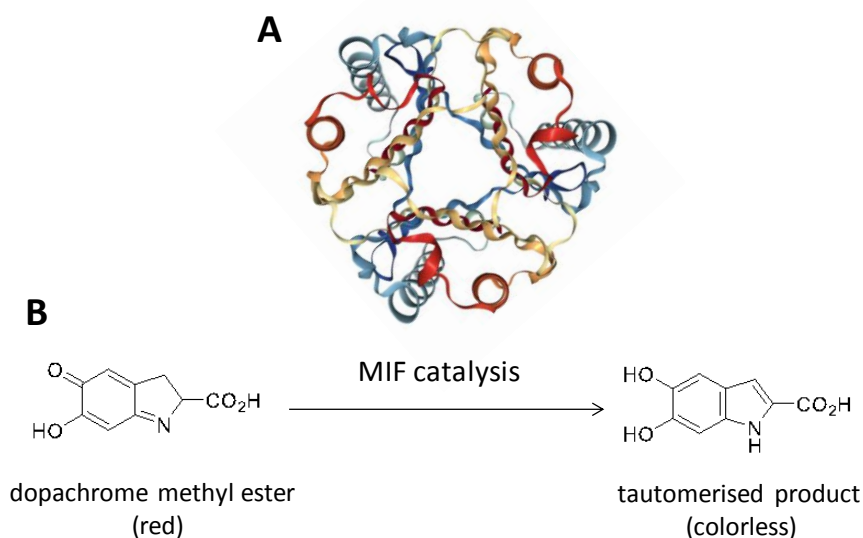


**Figure 1.1:** MIF Structure and function. A) The crystal structure of human, MIF PDB code: 1MIF. B) Chromogenic substrate (left) for the measurement of MIF enzymatic activity, and its tautomerised, colourless product (right) [19, 26].

### 1.1.2 Signalling and function of MIF

The unique biological functions associated with MIF have led to it being described as a cytokine, enzyme, hormone, and chemokine [19]. MIF functions through autocrine/paracrine loops inducing expression of pro-inflammatory cytokines such as TNF- $\alpha$ , IL-1 $\beta$ , IL-6, nitric oxide, COX2, and IFN- $\gamma$  [27]. There are multiple mechanisms by which MIF's biological function can lead to pulmonary malignancies (Figure 1.2). MIF has shown to bind to the cell surface receptor CD74 inducing a sustained MAPK/ERK activation. It negatively regulates the anti-inflammatory effects of glucocorticoids and the tumour suppressor protein p53 resulting in increased cell proliferation and reduced growth limitation [28]. It has also been shown that both endogenous intracellular MIF and exogenous MIF after endocytosis, interact and directly bind to c-Jun activation domain binding protein-1 (JAB1). MIF antagonises JAB1-stimulated AP-1 transcription and JAB1-induced JNK activity [29]. JAB1 also interacts with p27<sup>Kip1</sup>, which functions as an inhibitor of cell cycle progression. This results in promoting p27<sup>Kip1</sup> degradation and blocking the cell cycle. MIF prevents this function and

p27<sup>Kip1</sup> levels rise, dropping cell proliferation [30]. Moreover, MIF/JAB1 complexes have been detected in atherosclerotic plaque tissue [31], and pituitary tumours [32]. It has been observed that at low MIF concentrations, MIF would signal through membrane bound receptors (CD74) functioning in a pro-inflammatory fashion. However at higher concentrations of MIF it could act via the non-receptor based JAB1-mediated signalling pathway and thus have a negative effect on inflammation and cell growth [33].

HIF1 $\alpha$  (hypoxia inducible factor) is known as the master transcriptional factor which is involved in providing the environment that favours tumour growth, it forms a complex with the HRE (hypoxia responsive element) in the promoter region of the target gene which activates their expression [34]. The further investigation to understand the precise role of MIF and hypoxia has shown that MIF is required for optimal hypoxia-induced HIF-1 $\alpha$ . It has also been explained that MIF deficient cells do not allow for stabilisation of HIF-1 $\alpha$  that is hypoxia-induced [35]. Another study that was conducted to investigate MIFs role in angiogenesis related signalling pathways, revealed that MIF acts through the activation of MAP kinases which allows for the differentiation of endothelial cells to blood vessels. This showed another strategically important role for MIF in a hypoxic setting [36]. MIF, also, counter-regulates the immunosuppressive effects of glucocorticoids at transcriptional and post-transcriptional levels. MIF prevents the glucocorticoid-mediated induction of inhibitor of nuclear factor- $\kappa$ B (I $\kappa$ B) synthesis and messenger RNA destabilisation, and overrides the glucocorticoid-mediated inhibition of phospholipase A2 (PLA2) activity and arachidonic acid production [12].

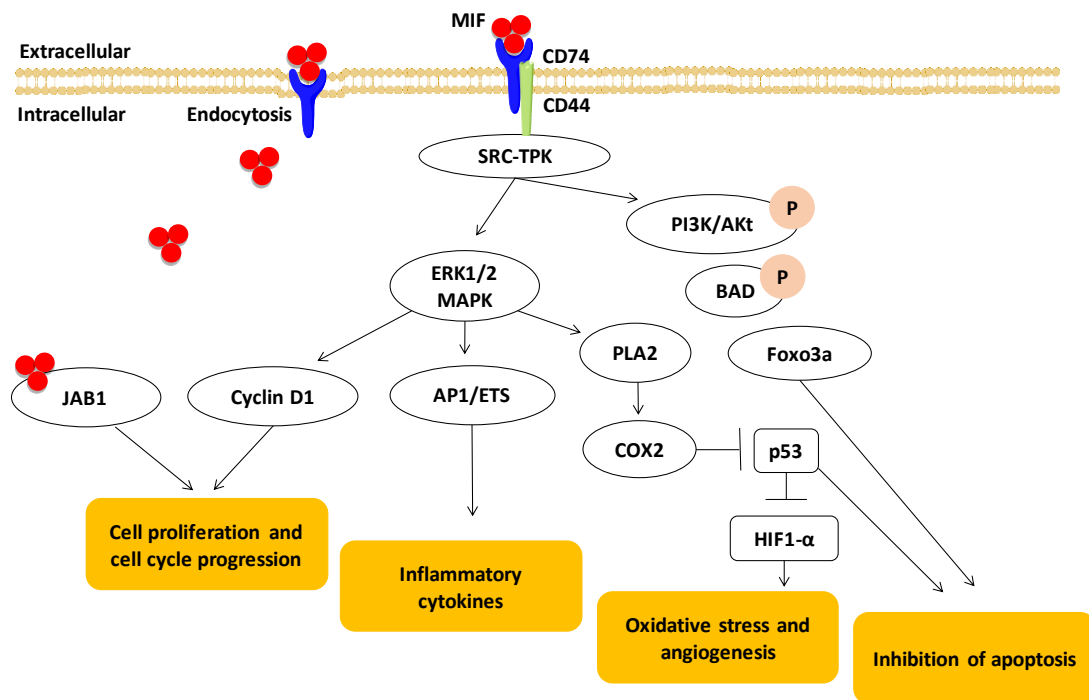


**Figure 1.2:** The role of MIF in cell signalling. MIF causes a cell signalling cascade, inducing cell cycle progression and pro-inflammatory cytokine secretion. It prevents apoptosis through down regulation of tumour suppressor factor, p53. The effect of MIF on cellular signalling is started through receptor mediated pathways and intracellular interactions; MIF forms a complex with its receptor (CD74) and coreceptor (CD44), leading to phosphorylation of ERK 1/2 and sustained MAPK ERK1/2 activation, that triggers downstream processes including the release of pro-inflammatory cytokines and cell proliferation. During this process, activation of phospholipase A2 (PLA2) and cyclooxygenase 2 (COX2) leads to the downregulation of the tumour suppressor p53 and the inhibition of apoptosis. The Akt pathway is also activated via CD74, leading to phosphorylation of proapoptotic proteins such as BAD, this further contributes to cell survival and the inhibition of apoptosis. MIF can also play a role in the stabilisation of HIF-1 $\alpha$  through a p53-dependent mechanism. HIF-1 $\alpha$  is a key transcription factor for angiogenic proteins such as VEGF. MIF also plays a role in chemotactic recruitment of cells to the sites of inflammation via its interaction with CXCR2/4. Pathway modified from reference [37].

### 1.1.3 MIF and airway diseases

MIF is a crucial mediator of host defence particularly in the context of the regulation of the inflammatory response[38]. However, in the context of excessive production in end-organs it can contribute to drive a chronic inflammatory phenotype and lead to the propagation of chronic inflammatory diseases [39, 40]. There is a growing body of evidence linking MIF in various

pulmonary diseases, and the importance of MIF has been demonstrated in many of clinically relevant lung disease models where over-expression of MIF has been associated with more aggressive clinical phenotypes [41-44]. These diseases include lung cancer [24], nasopharyngeal cancer [45], tuberculosis [46], asthma [47], cystic fibrosis [48], pneumonia [49], idiopathic pulmonary fibrosis (IPF) [43], Wegener's granulomatosis [50], pulmonary hypertension [51], obstructive sleep apnea [52] chronic obstructive pulmonary disease (COPD) [53] and acute respiratory distress syndrome (ARDS) [54] (see Figure 1.3).

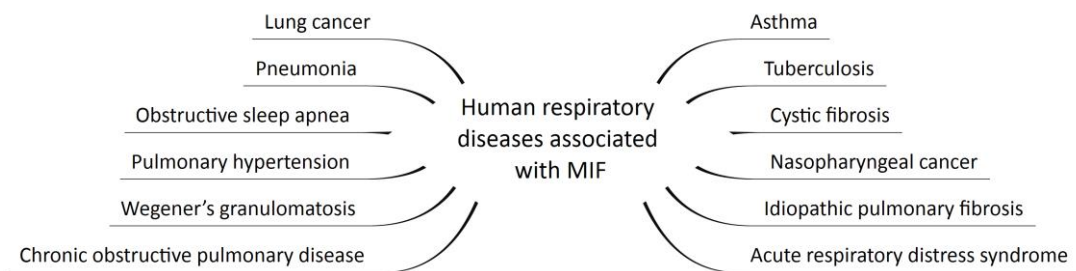


**Figure 1.3:** The association of macrophage migration Inhibitory factor (MIF) with respiratory diseases [55-57].

### 1.1.4 The role of MIF in lung cancer

lung cancer has the highest mortality rate worldwide, accounting for 14% of all cancers [58], which translates to 2.09 million new cases and 1.76 million deaths in 2018 [59]. Over the last 30 years prognosis for patients has remained poor with an average 5 years survival rate remaining relatively unchanged at of 17.8% which is much lower than that of other leading cancers [60]. Therefore, a significant global clinical unmet need is to define novel new targets and therapies for patients with this aggressive cancer.

There now is a critical mass of published work highlighting the important role MIF plays in cancer pathogenesis. MIF expression levels correlate with premalignant, malignant, and metastatic tumours in numerous cancer types, including breast, pancreas, prostate, colon, brain, skin, and lung-derived tumours. Significantly higher levels of both MIF message and protein, have been

shown in a variety of human tumours compared with their noncancerous cell counterparts [42, 61-64]. MIF can play a key role in angiogenesis, metastasis, and tumour development via distinct pathways, all highlighting the important contribution of this cytokine to cancer growth, proliferation and spread (Figure 1.4).

It is well recognised that chronic inflammatory diseases are associated with increased risk of cancer, and it has been proposed that MIF potentially is a key link between lung inflammation and cancer development [38]. MIF is released from the cells into the alveolar space which brings about upregulation of angiogenic growth factors and downregulation of apoptosis, this can have a proangiogenic effect, particularly in studies of tumorigenesis [24, 44]. In a clinical study, Kamimura et al. showed that in normal lung tissues, both MIF mRNA and protein can be found in the bronchial and alveolar epithelium, endothelium, vascular smooth muscle, and alveolar macrophages. However, in lung adenocarcinoma tissues, MIF is accumulated significantly in the alveolar epithelium relative to normal tissue concentrations [65]. It also has been shown that there is direct correlation between the levels of MIF in the nuclei of non-small cell lung cancer and a worse prognosis [62]. Moreover, MIF can act together with its newly described homolog, D-dopachrome tautomerase as a MIF family member, to upregulate the expression of CXCR8 and VEGF in non-small-cell lung carcinoma leading to angiogenesis progression contributing to tumour growth, survival, and invasion [66]. An animal model of chronic lung injury has revealed that enhanced MIF expression promoted lung tumour growth, indicating the critical role of this cytokine in lung tumour development in chronic inflammatory diseases [67].

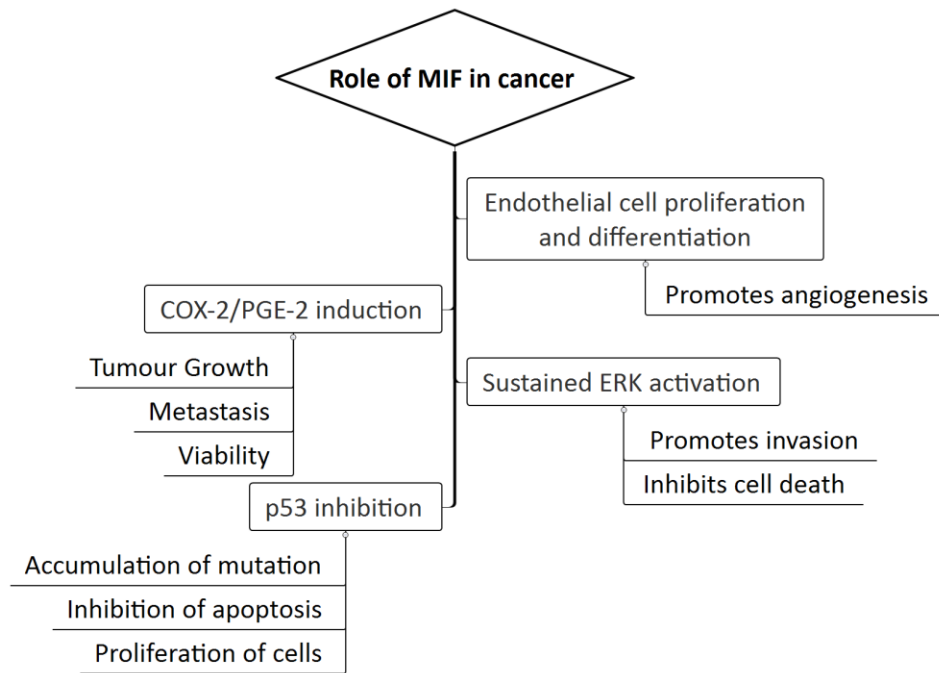


**Figure 1.4:** The role of MIF in cancer. MIF plays a critical role to develop cancers by downregulating p53 expression and stimulating angiogenesis, ERK activation, and COX-2/PGE-2 production. The graph was adapted from Ref [19].

### 1.1.5 The enzymatic active site of MIF; a therapeutic target

Experimental evidence in recent years has supported strongly a link between chronic inflammation and cancer progression/severity [38, 68]. The rational for further studies on the inhibition of MIF's biological function comes from the substantial evidence that supports the involvement of MIF in the pathogenesis of disease which makes it an attractive therapeutic target in not only cancers but also many infectious and inflammatory diseases [69]. The importance of MIF in cancer has been confirmed in several preclinically and clinically relevant cancer models where deletion of MIF or deactivation of its enzyme activity has shown a considerable reduction in the progression or mortality of cancer [70]. This includes prostate cancer [71], colorectal cancer [72], bladder cancer [73], pancreatic [74], gastrointestinal cancer [75]. To define the role for MIF's enzymatic activity in cancer pathogenesis, a tautomerase-null MIF gene knockout mouse, *Mif*<sup>P1G</sup>, was generated, in which the MIF N-terminal

proline (Pro1), the active site, encoded by exon 1 of *mif* is replaced with glycine by exchanging the codon CCT for GGC. A Lewis lung carcinoma (LLC) murine model was established in *Mif*<sup>P1G</sup>, *Mif-KO* (MIF knockout) and wild-type (WT) mice and this work showed a significant reduction in tumour growth in both *Mif*<sup>P1G</sup>, *Mif-KO*, in contrast to wildtype mice, suggesting that lung cancer depends on MIF's tautomerase action and modulating MIF's enzyme activity may be a novel therapeutic target for the treatment of cancer [24]. In fact, numerous different strategies have been undertaken in the past to inhibit/moderate MIF biological activity, including anti-MIF antibodies, indirect destabilisation of MIF, small molecule disruption of MIF activity. The inhibition of MIF's enzyme activity by using small molecules is one of the most promising approach to modulate the MIF function for the treatment of various diseases such as lung cancer [19]. Moreover, the inhibition of MIF's tautomerase activity has shown promising results in experimental sepsis, chronic inflammatory, and cancer diseases [76-79].

The three-dimensional x-ray crystallographic structure of MIF displays the existence of a catalytic site, also known as the tautomerase active site, which serves as a small-molecule binding pocket and contains highly conserved amino acid residues known to be crucial for MIF's proinflammatory activity [80]. This hydrophobic active site is of great interest for pharmacological development because it offers access to the protein's surface for design of small molecular weight inhibitors to target the catalytic site of MIF [19]. SCD-19 is a novel small-molecular-weight inhibitor targeting MIF's tautomerase activity which has shown promising results in both lung cancer and inflammatory studies. In a previous study, to examine the activity of SCD19, a subcutaneous Lewis lung carcinoma murine model was established in the mice. After tumour growth, the mice were treated by intraperitoneal (IP) injection of SCD-19 (35 mg/kg) twice weekly. The result of 30 days monitoring tumour volume showed that SCD19 reduced the tumour growth by 90% and it was dramatically more active than ISO-1, a commercial available MIF inhibitor [24]. In a different study, it was also reported

that SCD-19 significantly decreases the inflammatory response in a murine pulmonary chronic *P. aeruginosa* model, suggesting that SCD-19 might be used in both cancer and inflammatory diseases [40].

## 1.2 Nanomedicine applications in the lung cancer

The applications of nanotechnology in medicine, referred to as nanomedicine is a relatively new field commencing in the 1990s [81]. Nanomedicine as a common interpretation in pharmaceutical sciences is the study and utilisation of materials and devices below 1000 nanometers (nm) in size [82, 83]. Nanomedicine is a multidisciplinary research field with an integration of traditional sciences such as chemistry, physics, biology and materials science [84]. Food and Drug Administration (FDA) has introduced the use of nanomedicine as one the top priorities to stimulate innovation in the fields of medicine by stating “*Nanotechnology holds huge promise for the design and manufacture of many types of novel medical products—from devices to therapeutics to combination products*” [85]. It is widely believed that nanomedicine can open doors to new opportunities for the treatment of different types of cancer such as respiratory cancers [86-88]. Promising research outcomes suggest that nanomedicine will revolutionise the way we practice medicine, through the development of new approaches in therapeutic agent delivery [89], vaccine development [90], nanotechnology based medical detections [91], and therapeutic-diagnostic capabilities into one single nanoplatform (referred as theranostics) [92]. When it comes to recent clinical studies, the most active areas are drug delivery, vaccination and diagnosis (see Table 1.1). Whereas, theranostic systems have been investigated mostly in research studies thus far.

**Table 1.1:** Examples of nanomedicines employed for lung cancer in clinical trials or on the market, collected from clinicaltrials.gov. <sup>a</sup> Approved in Korea (2007) [93].

<b>Therapeutic delivery</b>				
<b>Tradename</b>	<b>Route of administration</b>	<b>Particle type/ therapeutic agent</b>	<b>Indication</b>	<b>Approval/ Status</b>
Abraxane	Intravenous	Polymeric/paclitaxel	Non-small cell lung cancer (NSCLC)	FDA approved (2012)
Genexol® PM	Intravenous	Micellar/paclitaxel	Lung cancer	(Ph II) <sup>a</sup> in US
Genexol® PM	Intravenous	Micellar/paclitaxel in combination with cisplatin	Lung cancer	NCT02667743 (Ph III)
Lipoplatin	Intravenous	Liposomal/cisplatin	Non-small cell lung cancer	(Ph III)
Opaxio	Intravenous	Polymeric/paclitaxel	Lung cancer	(Ph III)
Paclitaxel poliglumex	Intravenous	Micellar/paclitaxel	Non-small cell lung cancer	(Ph III)
nab-P/C	Intravenous	Polymeric/ paclitaxel in combination with free carboplatin	Non-small cell lung cancer	NCT02027428 (Ph III)
ONIVYDE®	Intravenous	Liposomal/ topotecan	Small cell Lung cancer	NCT03088813 (ph II/III)
Abraxane	Intravenous	Polymeric/paclitaxel in combination with pembrolizumab and carboplatin	Non-small cell lung cancer	NCT02775435 (Ph III)
Xyotax (CT-2103)	Intravenous	Polymeric/paclitaxel compared with paclitaxel	Advanced lung cancer	NCT00269828 (Ph III)
Xyotax (CT-2103)	Intravenous	Polymeric/paclitaxel in combination with carboplatin and compared with paclitaxel plus carboplatin	Advanced or recurrent non-small cell lung cancer	NCT00054210 (Ph III)
Xyotax (CT-2103)	Intravenous	Polymeric/paclitaxel compared with gemcitabine or vinorelbine	Advanced or recurrent non-small cell lung cancer	NCT00054197 (Ph III)
Xyotax (CT-2103)	Intravenous	Polymeric/paclitaxel compared with	Progressive non-small cell	NCT00054184 (Ph III)

		docetaxel	lung cancer	
Xyotax (CT-2103)	Intravenous	Polymeric/paclitaxel in combination with carboplatin	Non-small cell lung cancer	NCT00576225 (Ph III)
Xyotax (CT-2103)	Intravenous	Polymeric/paclitaxel in combination with carboplatin	Stage IIIB, stage IV, or recurrent non-small cell lung cancer	NCT00551733 (Ph III)
Xyotax (CT-2103)	Intravenous	Polymeric/paclitaxel in combination with Alimta	Advanced non-small cell lung cancer	NCT00487669 (Ph II)
Xyotax (CT-2103)	Intravenous	Polymeric/paclitaxel in combination with carboplatin	Stage III non-small cell lung cancer	NCT00352690 (Ph II)
Doxil® / Caelyx®	Intravenous	Liposomal/doxorubicin	Non-small cell lung cancer	NCT01051362 (Ph II)
SPI-77	Intravenous	Liposomal/cisplatin	Advanced non-small-cell lung cancer	(Ph II)
Abraxane	Intravenous	Polymeric/paclitaxel in combination with free carboplatin and bevacizumab	Non-small cell lung cancer	(Ph II)
OSI-211	Intravenous	lurtotecan/Topotecan	Small cell lung cancer	NCT00046787 (Ph II)
Abraxane	Intravenous	Polymeric/paclitaxel in combination with Carboplatin	Small cell lung cancer	NCT00454324 (Ph II)
CRLX101	Intravenous	Polymeric/ olaparib	Lung cancer	NCT01380769 (Ph II)
Abraxane	Intravenous	Polymeric/Gemzar	Lung cancer	NCT02449122 (Ph I/II)
Abraxane	Intravenous	Polymeric/paclitaxel in combination with free carboplatin	Advanced squamous cell carcinoma of lung	NCT01236716 (Ph I/II)
NC-6004	Intravenous	Micellar/ cisplatin in combination with free gemcitabine	Advanced solid tumours, including non-small cell lung cancer	NCT02240238 (Ph Ib/II)
Oncoprex	Oral	Lipid/ plasmid DNA encoding FUS1 (TUSC2)	Lung cancer	NCT01455389 (Ph I/II)
Oncoprex	Oral	Lipid/ plasmid DNA encoding FUS1 (TUSC2)	Lung cancer	NCT00059605 (Ph I/II)
CRLX101	Intravenous	Polymeric/olaparib in combination with free camptothecin	Non-small cell and non-small cell lung cancer	NCT02769962 (Ph I/II)
Abraxane	Intravenous	Polymeric/paclitaxel in combination with free Nintedanib	Non-small cell lung cancer	NCT03361319 (Ph I/II)

CYT-6091	Intravenous	Gold and Polymeric/ tumor necrosis factor alpha	Lung cancer	(Ph I)
SGT-53	Intravenous	Liposomal/plasmid DNA encoding wild- type p53	Solid tumours	NCT00470613 (Ph I)
TargomiRs	Intravenous	Nonviable minicells/ miRNA	Pleural mesothelioma and non-small cell lung cancer	NCT02369198 (Ph I)
Abraxane	Intravenous	Polymeric/paclitaxel in combination with free gemcitabine	Small cell and non-small cell lung cancer	(Ph I)
Abraxane	Intravenous	Polymeric/ paclitaxel	Non-small cell lung	NCT02495896 (Ph I)
BIND-014	Intravenous	Polymeric/docetaxel	advanced or metastatic cancer included lung cancer	NCT01300533 (Ph I)
AuroLase (Nanospectra Biosciences)	Intravenous	Silica-gold nanoshell /AuroLase® Therapy (hyperthermia cancer therapy)	Metastatic lung tumours	NCT01679470

## Diagnosis

Trade name	Mechanism	Nano particle type	Indication	Approval/ Status
Electronic nose	Volatile organic compounds (VOC) detection	Polymeric nanoparticles	Lung cancer	NCT01386203

## Vaccination

Trade name	Route of administration	Particle type	Vaccine antigen /Adjuvant	Approval/ Status
BLP25 (Stimuvax®)	Intravenous	Liposomal	MUC1/MPLA	NCT01015443 (Ph III)
BLP25 (Stimuvax®)	Intravenous	Liposomal	MUC1/MPLA	NCT00409188 (Ph III)
BLP25 (Stimuvax®)	Intravenous	Liposomal	MUC1/MPL	NCT00960115 (Ph I/II)

The continued progress of nanomedicines has the potential to provide numerous benefits in the field of cancer as some examples have been highlighted in Figure 1.5. The most promising application of nanomedicine in the field of lung cancer is to use nanoparticles as nanodrug delivery vehicles [94], which will be discussed in the next section of this thesis.

It has been well demonstrated that there is a direct relationship between immunity and lung cancer which might provide a new immunotherapeutic approach that can be combined with other therapeutic methods such as immunotherapy, chemotherapy, radiotherapy, and surgery to treat lung tumours [95]. In the context of lung cancer, one could envisage nanomedicine and specifically, nanocarriers possessing enhanced ability to deliver subunit vaccines made of small molecule, protein and peptides, antigens that may overcome current common vaccine industry problems including, degradation, non-specific targeting, and lack of sufficient number of antigen-presenting cells [96]. To achieve higher immunity response, nanoparticles have the capacity to present multiple peptide epitopes in a repetitive pattern, thus addressing a current challenge related to poor immunogenicity in current peptide-based subunit vaccines [97]. Recent clinical studies of nanovaccine for immunotherapy against lung cancer have shown promising results, in terms of disease stability and improvement of Overall Survival (OS) in non-small-cell lung cancer patients [98, 99].

One of the significant challenges in improving lung cancer survival relates to the late presentation, when the cancer has already spread beyond the lungs. Thus, novel methods to detect lung cancer at an earlier timepoint represents a significant global clinical unmet need. Nanoparticles offers a potential solution for improving early lung cancer diagnosis/detection as it is highly sensitive, non-toxic, and relatively non-invasive [100].

Exhaled breath volatile organic compound (VOC) analysis is one of the promising techniques for the early detection of lung cancer [101]. Recently, an

advanced nanobiosensor-based system, generally referred as nano-nose or electronic nose, has been investigated to detect and diagnosis lung cancer at the early stage [102]. Nano-nose is a chemiresistor nano-sensor array that can analyse rapidly volatile organic compounds (VOCs) from exhaled breath of patients as VOCs related to various diseases, and their composition differs from one disease to another [103]. These sensors can distinguish between the breath of a healthy and cancerous individual by detecting lung cancer biomarkers in the collected VOCs which forms the foundation for a feasible, fast and accurate method for the detection of lung cancer [104]. Nakhleh and colleagues has recently introduced a new generation of nano-nose, so called an artificially intelligent nanoarray based, that is able to detect seventeen different types of cancer at the same time with almost 90% accuracy [105]. This nano-based new array provides an easy-to-use and portable tool for personalised screening that can classify of seventeen different diseases only from exhaled breath.

The term “theranostics” is defined as combining diagnostics and therapies in a single modality and is gaining significant interest in cancer molecular imaging and therapy [106]. Numerous nanoparticle-based theranostic systems have been created over last ten years to monitor the therapy at a cellular level and to provide tracking of nanoparticles both *in vitro* and *in vivo* [107]. Theranostic agents can play critical roles in early stage drug development as well as clinical-stage therapeutic-containing drug candidates.

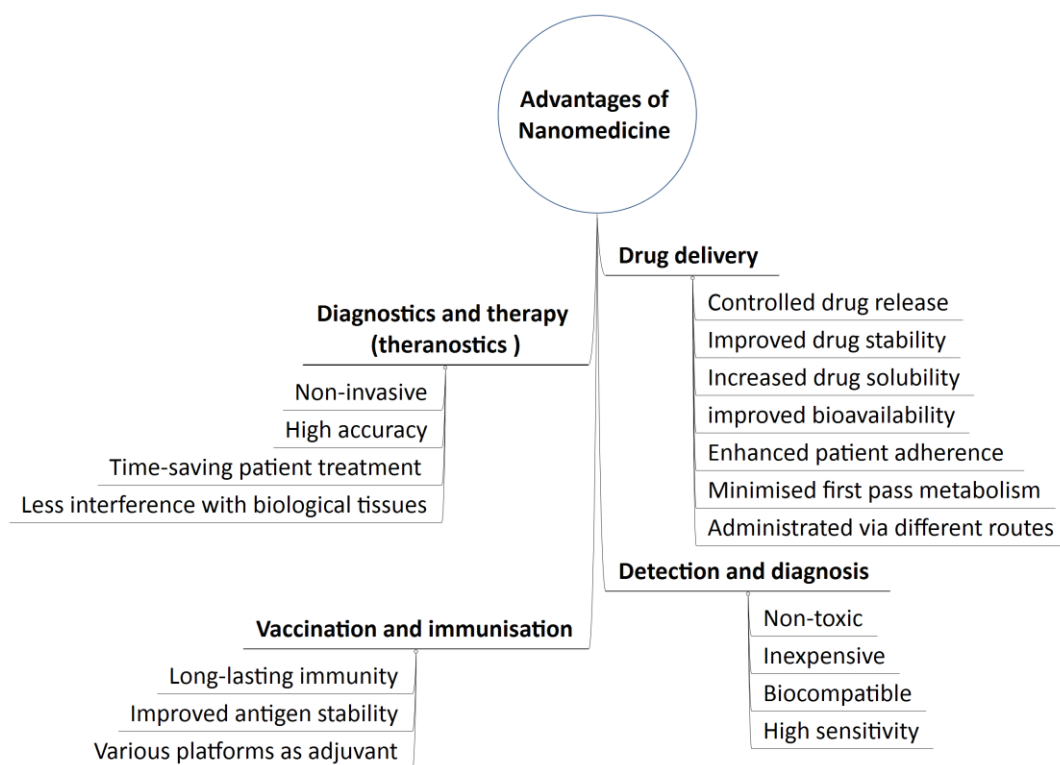


**Figure 1.5:** Benefits of nanomedicine applications for the treatment of lung cancer.

### 1.2.1 Nanodrug delivery systems

Nanodrug delivery systems are playing an increasingly important role in the field of nanomedicine [108]. Nanotherapeutics have been approved for the treatment of cancer for over 20 years, since the approval of Doxil®, a liposomal form of the chemotherapy drug doxorubicin, in 1995 for AIDS related Kaposi's syndrome. This was the first nanotherapeutic to be approved by the FDA and since then [109], has continued to motivate the development of new nanotherapeutics for the treatment of cancer, as illustrated by the dominance of cancer as the primary therapeutic indication (see Table 1.1). There are currently two nanotherapeutics approved for the treatment of lung cancer. Both contain the potent chemotherapeutic paclitaxel as the active drug component, which is widely used to treat a number of different solid tumours including ovarian, breast and lung cancer [110]. Due to its poor water solubility, paclitaxel is administered with surfactants such as Cremophor EL as solubilisers to increase

its bioavailability. But, such excipients have been associated with high toxicity and adverse events, such as hypersensitivity and neurotoxicity [86]. However, using advanced nano-drug carriers, the use of such excipients, and their associated toxicities, can be avoided. In the case of Genexol-PM, the first nanotherapeutic approved for the treatment of non-small-cell lung cancer (NSCLC) in Korea in 2007, paclitaxel is encapsulated into nano-sized polymeric micelles, which allows a significantly higher paclitaxel dose to be administered to patients without an increase in toxicity [111]. Abraxane is a protein-based nanotherapeutic, which was originally approved in 2005 for the treatment of metastatic breast cancer and gained FDA approval in 2012 as a first-line treatment of advanced NSCLC after a phase III clinical trial demonstrated the superiority of the nanotherapeutic over the free drug in combination with carboplatin [112]. In recent years, there have been ongoing clinical trials investigating the efficacy of these approved (Abraxane and Genexol-PM) nanotherapeutics in combination with other chemotherapy drugs for the treatment of lung cancer; NCT03361319, NCT02495896, NCT02667743, NCT02027428, and NCT01023347.

The use of nanoparticle-based delivery systems is the most documented area either in preclinical and clinical studies, when it comes to nanotechnology in respiratory medicine (figure 1.6 A) [113, 114]. In fact, almost 40% of currently marketed drugs and virtually 90% of small molecules being developed as novel drug candidates are poorly water-soluble [115, 116]. Solvents like dimethylsulfoxide (DMSO) and dimethylformamide (DMF) are recognized as common solvent to dissolve a wide range of insoluble drugs however their cost and toxicity pose a limitation on their use for any therapeutic purpose [117]. A promising strategy has emerged over the past three decades to address this intrinsic drawback of chemotherapeutics.

There are various types of nanoparticles derived from organic and inorganic materials, (see Figure 1.6 B) which have been used to improve water solubility for hydrophobic drug molecules [118]. Furthermore, the ability of

nanoparticles to carry therapeutic agents, including organic and inorganic, small and macromolecules has also been demonstrated to improve the stability of the drug *in vivo*, enhance the circulating half-life and increase cellular accumulation of the drug [108, 119]. It has been well demonstrated that nanoparticle delivery systems improve the stability of therapeutic agents and prevent degradation *in vivo*, thereby enabling the delivery of drugs [120]. Employing nanoparticles to deliver therapeutic agents can enhance bioavailability and overcome natural barriers, such as mucosa [121]. Moreover, nanocarriers can be administered via different routes, including intravenous [122], oral [123], and inhalation [124] (see Figure 1.6 C) and the development of nanomedicine, has allowed scientists to achieve these outcomes, without the need to modify existing drugs [89, 124]. One of the most pressing need in cancer is to design effective treatments that minimize damage to normal tissue. Anticancer drugs loaded in a nanodrug carrier tend to accumulate in tumour tissue much more than they do in normal tissues through the enhanced permeability and retention (EPR) effect which refers to the accumulation of nanoparticles (NPs) in tumour facilitated by the highly permeable nature of the tumour vasculature and poor lymphatic drainage of the interstitial fluid surrounding a tumour [125].

Nanodrug carriers can also be targeted, so called smart drug carriers, to enhance the accumulation of drug compounds in specific disease site and limit the exposure to healthy tissues, thereby, reducing drug side effects, and reducing the required dose to be administered to the patient [126]. It has been shown that overexpression of surface markers on tumour cells which are absent in normal cells provides an opportunity of targeting the nanodrug delivery systems to cancer cells [127]. Conjugating specific moieties, which include, small molecules, proteins, and peptides to the surface of nanoparticles are the most common strategies to design a targeted nanodrug delivery carrier [128]. As a smart nanodrug delivery system, drug releases can be also controlled/stimulated to maximize drug sustain release, prolonged dosage and efficiency [129], by

employing pH-responsive [130], thermo-responsive [131], redox-responsive [132], photo-responsive [133], magnetic-responsive [134] drug carriers.

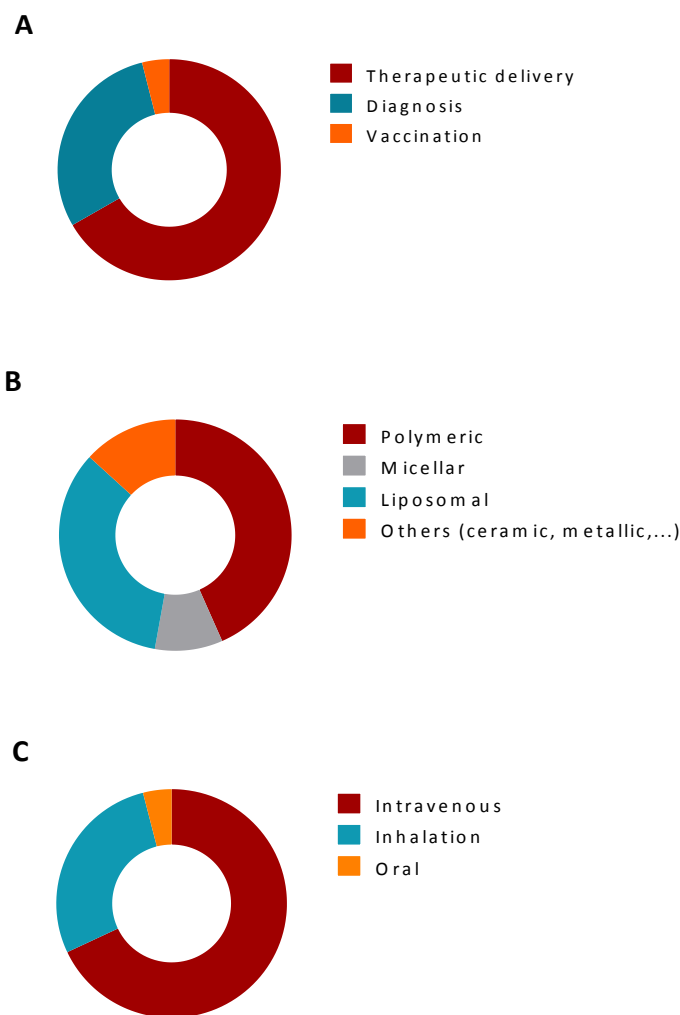


**Figure 1.6:** The data collected based on recent registered clinical trials on Clinicaltrials.gov. A) the proportion of the three most applications of nanomedicine in lung diseases filed. B) the most popular types of nanocarriers used for the treatment of lung diseases. C) the proportion of three different routes of administration employed to treat lung diseases by using nanoparticles.

### 1.2.2 Nano polymer-based for drug delivery

Numerous research efforts have focused on using polymeric nanodrug delivery systems as one of the most prominent nanotherapeutic delivery vehicles, due to their large potential in drug delivery [135]. The attracting characteristics of polymeric nanoparticles include a wide payload spectrum of both hydrophobic and hydrophilic therapeutic agents such as chemical compounds (e.g. paclitaxel, doxorubicin) [136], small biomolecules (e.g. DNA,

protein) [137], and metallic materials (e.g. silver, iron) [138]. Therapeutic agents can be adsorbed, encapsulated, entrapped, and conjugated either throughout or onto the polymeric nanoparticles matrix/ shell as illustrated schematically in figure 1.7 [139, 140].

Other outstanding features of polymer-based nanodrug carriers are their biodegradability and biocompatibility, thus therapeutic agents can be released in a controlled manner by taking the advantages of biodegradation kinetics of the polymers, this can improve toxicity profile and prolonged circulation of drug candidate [141]. Moreover, polymeric nanodrug carriers can be easily administrated via different routes which include, oral, injection, and inhalation routes [135]. Polymeric nanoparticles are one of the most widely approved nanomedicines for the treatment of disease, for instance DOXIL (the first FDA-approved nano-drug), Genexol-PM, and Abraxane [137].

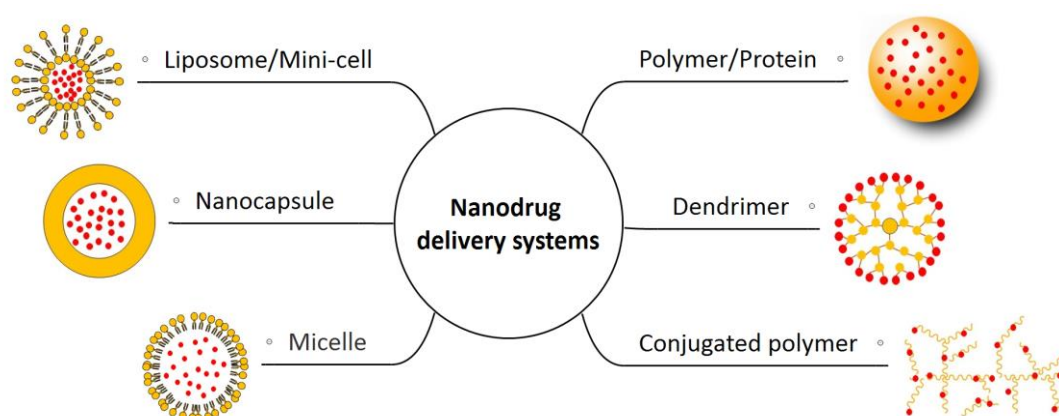


**Figure 1.7:** The most common types of nanocarriers have used for therapeutic agent delivery in preclinical and clinical studies to treat lung diseases. Small red circles represent schematically therapeutic agents.

The ability to modify the surface of polymeric nanoparticles have made them ideal candidates for targeted drug delivery in various diseases treatment, including cancer therapy and offers a substantial improvement over traditional methods of drug delivery system in terms of efficiency and effectiveness [137]. Several different clinical trials are being conducted to investigate the efficacy

and safety of the targeted polymer-based nanodrug delivery systems for the treatment of lung cancer; NCT02369198, NCT01792479, NCT02283320, NCT02769962, and NCT01300533 (see table 1.1).

Technically, there are two different types of polymer-based drug carrier. Natural polymer (e.g. albumin, chitosan) and synthetic polymer (e.g. polyethylene glycol, poly(lactic-co-glycolic acid)) nano delivery vehicles [142]. Natural polymers can be directly found in natural resources such as green plants, animals, and bacteria. Synthetic polymers, however, are synthesised in the laboratory by using different chemical components [143]. It has been reported that poly(lactic-co-glycolic acid) or PLGA is the most studied/used of the degradable synthetic polymers which has been developed as a biodegradable polymer, owing to its features of controlled-release, and special release profiles biodegradability [141, 144].

### **1.2.3 PLGA-based nanoparticles as a drug delivery system**

PLGA is a linear copolymer which has been approved by Food and Drug Administration (FDA) and European Medicines Agency (EMA) for human therapy, including drug delivery, diagnostics and other applications of clinical or basic science research [145]. Many innovative research studies have been reported in the literature, which highlighted the use of PLGA as a drug delivery system to deliver a variety of different types of therapeutic agents, including small molecules [146], proteins [147], and nucleic acids [148]. PLGA is the most popular among the various available biodegradable polymers due to its favourable characteristics that have been highlighted graphically in figure 1.8.

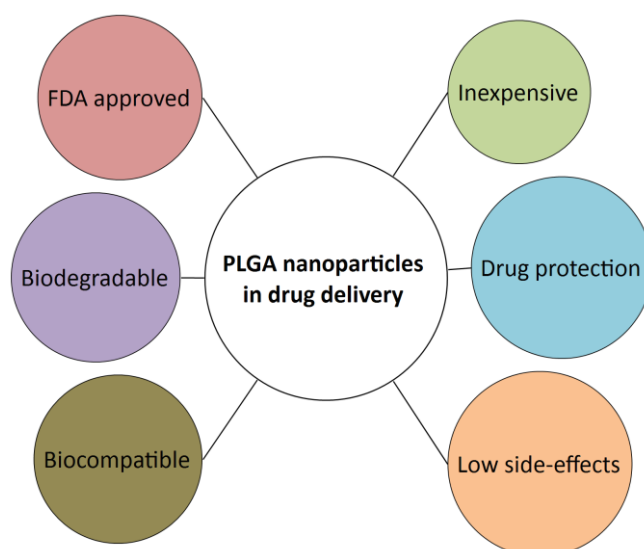


**Figure 1.8:** Benefits of PLGA nanoparticles in drug delivery applications.

PLGA can be synthesised at different ratios between its two basic monomer components, lactic [ $C_3H_4O_2$ ] and glycolic [ $C_2H_2O_2$ ] acid, that can directly impact on its release profiles, biodegradability and its ability to sustain therapeutic agent concentration for an extended period [149]. For instance, 50:50 (v/v) (lactic and glycolic acid) ratio represents faster drug releases than PLGA 65:35 [150]. In fact, drug release decreases as lactic to glycolic ratio increases. The reason is that glycolic acid is more hydrophilic than lactide acid so when the PLGA contains higher proportions of glycolic acid, increased degradation rate of the PLGA nanoparticles is observed because of higher hydrophobicity of PLGA. Therefore, the drug release can be controlled by choosing different ratios of lactic and glycolic acid [151].

PLGA biodegrades via hydrolysis in aqueous environments, breaking its ester linkages to form lactic and glycolic acid monomers that can be naturally metabolised by tricarboxylic acid cycle (Krebs cycle) (see Figure 1.9) [152]. This results in PLG being biocompatible, safe, and non-toxic as a platform for *in vivo* drug delivery with minimum side effect [153]. In fact, numerous *in vitro* and *in vivo* studies have shown the safety and efficacy of the drug loaded PLGA nanoparticles in cancer [154-157].

It is noteworthy to point out that there is already some micro PLGA-based therapeutic carriers in market such as Zoladex<sup>®</sup>, Sandostatin LAR Depot<sup>®</sup>, Nutropin Depot<sup>®</sup> [158], Lupron Depot<sup>®</sup>, Somatuline<sup>®</sup> LA, Trelstar<sup>™</sup> Depot, Arestin<sup>®</sup>, and Risperdal Consta<sup>™</sup> for the treatment of different diseases including cancer [159]. However, to the best of our knowledge, there is no nano PLGA-based drug carrier approved as a therapy.

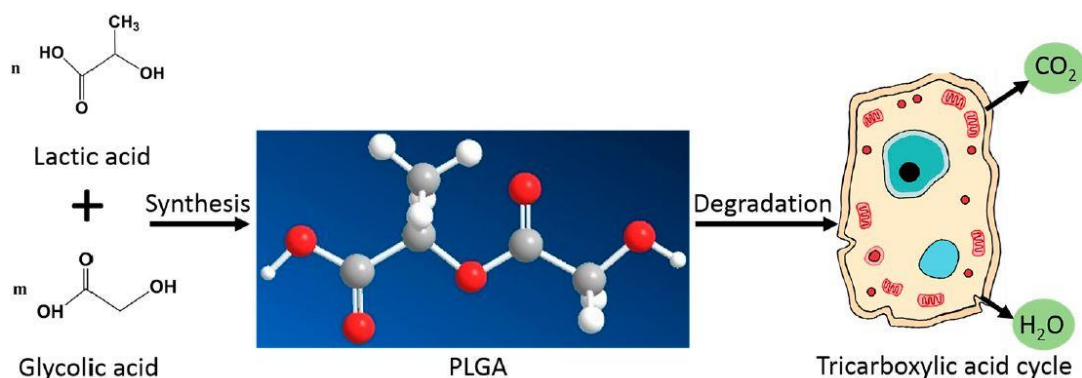


**Figure 1.9:** Synthesis of poly(DL-lactide-co-glycolide) (PLGA), chemical structure and degradation of PLGA via tricarboxylic acid cycle, adapted from ref [160].

### 1.2.4 Nebulised PLGA nanodrug delivery system

Local administration of nano-packaged drugs via the inhalation route delivers drugs effectively and specifically to the target organ, namely the lung resulting, on the one hand enhanced treatment efficacy, and on the other limiting spill-over into the systemic circulation, and consequently reducing the risk of potential adverse systemic side effects of the treatment [161]. Pulmonary drug delivery prevents the degradation of therapeutic components in the gastrointestinal tract and first pass metabolism in the liver. Moreover, the lung provides a large surface area of the alveolar region (100 m<sup>2</sup>) with low proteolytic activity which makes Inhalation local delivery an ideal strategy to treat pulmonary diseases. It has been shown that Inhalation local delivery increases significantly the drug half-life and the drug concentration in the lungs compared to the intravenous injection route [162]. This is in contrast to oral administration

which can be faced with poor bioavailability of the drug to the lung due to its degradation during first-pass metabolism [163, 164].

Despite all the advantages of inhalation therapy, it faces some challenges. In particular for the efficient delivery of therapeutic agents, nebulised drugs must effectively deposit along the airways, overcome extracellular and cellular airway barriers and, when needed, reach intracellular targets [165]. Over the last ten years, considerable attention has been focused on the ability of aerosolised PLGA nanodrug carriers to overcome the current challenges of inhalation therapy and to improve treatment efficiency for a wide range of lung diseases [166, 167]. For instance, Ungaro and colleagues has shown that antibiotic loaded PLGA nano particles achieved a deep lung deposition after pulmonary delivery and were associated with enhanced antibiotic availability [168]. In another *in vivo* study, the PLGA nanoparticles loaded with the anticancer drug (TAS-103) were administered in rats by inhalation route. This investigation resulted in a higher accumulation of drugs in the lung (almost 13-times) compared to those administered via intravenous injection. The PLGA nano carrier provided sustained levels of the drug in the lungs for up to 8 hours. In contrast, plasma concentrations detectable diminished at an accelerated rate over this time period, probably as a consequence of rapid systemic metabolism [169]. In a human non-small cell lung cancer model K-ras<sup>LA1</sup> mice, Jiang and co-worker showed that nebulised PLGA nano carrier system encapsulated Dihydroergotamine tartrate (anti-cancer drug) had very low cytotoxicity and systemic toxicity post-aerosol deliver. Moreover, the aerosol delivery of drug loaded PLGA nanoparticles significantly suppressed lung tumour growth by almost 50% [170]. Research work to date suggests that a nebulised PLGA-nanodrug delivery system is a useful, effective and safe in the treatment of cancer.

### 1.3 Hypothesis and Aims of the Project

Recently, Mawhinney et al. demonstrated the impact of a novel competitive inhibitor of MIF tautomerase activity, SCD-19, in a murine model of Lewis lung carcinoma (LLC). The results revealed that animals treated with 35 mg/kg SCD-19 twice weekly for one month had a significant tumour volume reduction (90%) in comparison to untreated animals, suggesting that SCD19 could be an effective drug for the treatment of lung cancer [24]. Here, we will explore the development of an aerosolised nanoparticle delivery system to improve the solubility and delivery of SCD19 that will allow for local delivery of MIF therapeutics directly to the lung utilising state of the art PLGA nanospheres (see Figure 1.10). This would—allow enhanced concentrations of active compound to be delivered to the lung while minimising potential systemic toxicity. The nanodrug delivery system (PLGA-SCD19) can target the enzymatic active site of both extracellular and intracellular MIF. MNPs were also incorporated into the PLGA NPs for imaging and detection purposes and for the final product they were removed from the NPs.

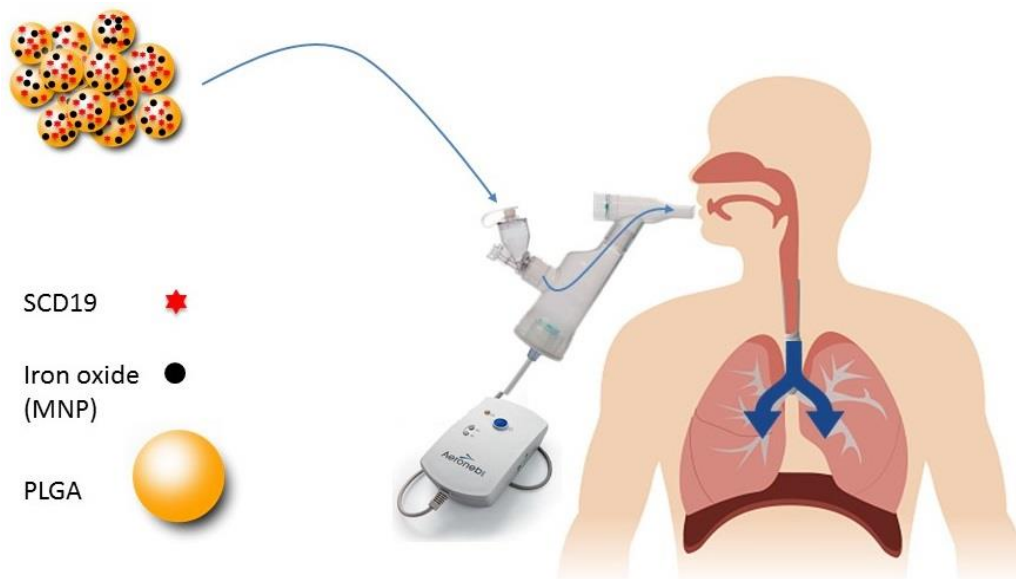


**Figure 1.10:** The concept of the project. The nanodrug delivery system consists of PLGA (drug carrier), Iron oxide (optionally, for imaging purpose), and SCD19 (drug candidate). The nanoparticles are nebulised into the lung by using an Aerogen Ultra nebuliser.

The main goals of this project are:

- i. The Generation and characterisation of SCD19 loaded PLGA NPs (PLGA-SCD19).
- ii. Assessment of the functional activity of PLGA-SCD19 and subsequent *in vitro* studies.
- iii. Optimisation and characterisation of an aerosolised delivery system for PLGA-SCD19 through *in vitro* studies.

# Chapter 2

## Materials & Methods

---

## Chemical materials and reagents used in this study

<b>Name</b>	<b>Cat No.</b>	<b>Supplier</b>
100-mesh copper grid	G100-Cu	Electron Microscopy Sciences
96-Well Polypropylene	005055073	Nunc
Acetone	650501	Sigma-Aldrich
Agarose	16550100	Invitrogen
Ammonium acetate	A1542	Sigma-Aldrich
Ampicillin	sc202951	Santa Cruz Biotechnology
Ascorbic acid	BP461	Sigma-Aldrich
Brilliant blue R 250	6104592	Sigma-Aldrich
Calcium chloride dihydrate	C3306	Sigma-Aldrich
Centrifugal Filter	UFC901024	Merk
Chambered Cell Culture Slides	354108	Falcon
cOmplete™ EDTA-free protease inhibitor	11873580001	Roche
cOmplete™ Protease Inhibitor Cocktail	11697498001	Roche
Coomassie® Brilliant blue R 250	C.I. 42660	Merck
D.P.X	317616	Sigma-Aldrich
Dichloromethane	650463	Sigma-Aldrich
Disodium hydrogen phosphate	S3264	Sigma-Aldrich
DMEM medium	41965-039	Gibco
Dulbecco's phosphate-buffered saline (DPBS)	14190-094	Gibco
EDTA	EDS	Sigma-Aldrich
EGTA	E3889	Sigma-Aldrich
Endotoxin free water	95289	Sigma-Aldrich
FBS	10270106	Gibco
Filter paper	WHA1201150	Whatman
Formaldehyde	F8775	Sigma-Aldrich
Formaldehyde	F1635	Sigma-Aldrich
Gel Loading Dye, Blue (6X)	B7021S	Biolabs
Glacial Acetic acid	27225	Sigma-Aldrich
Glycerine	PHR1020	Sigma-Aldrich
Glycerol	56815	Sigma-Aldrich
Glycine	G8898	Sigma-Aldrich
Hoechst	33342	Invitrogen
Hydrochloric acid	96208	Sigma-Aldrich
isopropylthio- $\beta$ -D-galactoside (IPTG)	I1284	Sigma-Aldrich
L- Glutamine	25030081	Gibco
L-3,4-dihydroxyphenylalanine methyl ester	D1507	Sigma-Aldrich
Leupeptin	L2884	Sigma-Aldrich
LPS free Water	95289	Sigma-Aldrich
Luria berttani (LB) agar	L3147	Sigma-Aldrich
Luria berttani (LB) broth	L3147	Sigma-Aldrich

Magnesium chloride	A0725033646	Merk
Methanol	67561	Sigma-Aldrich
Mini-protean TGX Precast Gel	456-1044	Bio-Rad
Mounting medium	H-1000	VECTASHIELD
MyTaq Red Mix, 2x	BIO-25043	Bioline
Neocuproine	N1501	Sigma-Aldrich
Nuclear fast red	60700	Sigma-Aldrich
Paraformaldehyde	F8775	Sigma-Aldrich
Penicillin and streptomycin	15070-063	Gibco
Phosphate-buffered saline (DPBS)	14190-094	Gibco
PLGA poly (lactic-co-glycolic acid)	719900	Sigma-Aldrich
Potassium chloride	P9541	Sigma-Aldrich
Potassium ferrocyanide	P3289	Sigma-Aldrich
PVA Poly (vinyl alcohol)	P8135	Sigma-Aldrich
Rhodamine phalloidin	R415	Invitrogen
Sodium acetate	S2889	Sigma-Aldrich
Sodium Chloride	S3014	Sigma-Aldrich
Sodium citrate dihydrate	6132-04-3	Sigma-Aldrich
Sodium citrate tribasic dihydrate	C3434	Sigma-Aldrich
Sodium Dodecyl Sulfate (SDS)	S-5200-53	Fisher Chemical
Sodium hydrogen carbonate	S5761	Sigma-Aldrich
Sodium hydroxide	S5881	Sigma-Aldrich
Sodium hydroxide	221465	Sigma-Aldrich
Sodium lactate	1614308	Sigma-Aldrich
Sodium orthovanadate	S6508	Sigma-Aldrich
Sodium periodate	210048	Sigma-Aldrich
Sodium pyrophosphate	221368	Sigma-Aldrich
Sodium pyruvate	P2256	Sigma-Aldrich
Sodium sulfate	13462	Sigma-Aldrich
Sodium tartrate dihydrate	228729	Sigma-Aldrich
SYBR® Safe DNA Gel Stain	S33102	Invitrogen
Trisodium phosphate	04277	Sigma-Aldrich
Triton X-100	X100	Sigma-Aldrich
Trizma® base	93362	Sigma-Aldrich
Trypsin-EDTA	25200056	Gibco
β-glycerophosphate	G9422	Sigma-Aldrich
DNA ladder	15628-019	Invitrogen

## The kits, instruments, and cells used in this study

<b>Name</b>	<b>Cat No.</b>	<b>Supplier</b>
Autoclavable Solo nebuliser	AS3100-US	Aerogen
Bacterial/viral filter	3500808	Baxter
Cell culture slides	354118	Corning
Centrifugal filter	UFC901024	Merk
Chambered Cell Culture Slides	354118	Falcon™
Confocal Microscope	LSM 510	Zeiss
Disposable cuvette	67.755	Sarstedt
Electrophoresis power supplier	model E865	Topac Inc.
Freeze Dry System	7750020	Labconco
HiLoad 16/600 superdex 200 pg	GE28989335	GE Healthcare
HiPrep™ Q Fast Flow 16/10	GE28936543	GE Healthcare
Human breathing simulator	ASL5000	Ingmar Medical
Human mechanical ventilator	SERVO-i	Getinge
LDH assay kit	11644793001	Roch
LLC cell line	CRL-1642	ATCC
Next Generation Impactor (NGI)	Model 170	Copley Scientific
Overhead stirrer (Lab egg, IKA® RW 11)	Z404756	Sigma-Aldrich
PenStrep	15070-063	Gibco
Pierce® High-Capacity Endotoxin Removal Resin	88276	Thermo Fisher Scientific
Pierce™ BCA Protein Assay Kit	23225	Thermo Fisher Scientific
Pierce™ LAL Chromogenic Endotoxin Quantitation	88282	Thermo Fisher Scientific
Quartz cuvette	Z600210	Hellma
Scanning electron microscopy	NEON 40 EsB	Zeiss
Slide-A-Lyzer MINI dialysis cassette	66330	Thermo Fisher Scientific
SpectraMax® i3x Multi-Mode	10014-924	Molecular Devices
Spraytec particle size analyser	MAN036930	Malvern
Sputter Coater	108auto/SE	Cressington Scientific
Stirrer	2830001	IKA
Syringe filter (0.22 µm)	SLGP033RS	Millex
Syringe filter (0.45 µm)	SLHU033RS	Millex
Transmission Electron Microscope	JEM-2100F	JEOL
Ultrasonic Processors	VCX 130 FSJ	Sonics
UV spectrophotometry	80300372	Biochrom
Vybrant™ MTT cell proliferation assay	V13154	Invitrogen
Zetasizer Nano	ZS90	Malvern

## 2.1 Experimental design

SCD19 was synthesised in professor Donnelly's lab and then it was encapsulated in PLGA nanoparticles (PLGA-SCD19) by using a single emulsion-solvent evaporation technique. To visualise the uptake of the nanoparticles in cells, another nanoformulation was also developed, we co-encapsulated iron oxide nanoparticles (MNPs) and SCD19 into PLGA nanoparticles (PLGA-MNP-SCD19). SEM, TEM, NTA and DLS were the first tests applied to look at the size, shape, charge and hydrodynamic diameter of the nanoparticles. LPS concentration was evaluated to ensure the supplied nanoparticles are LPS free and safe for further *in vitro* studies. The drug loading efficiency and drug content of the nanoparticles were investigated and calculated by an UV-spectrometer and a standard curve, which was generated by using a serial dilution of SCD19. An *in vitro* drug release study was carried out by employing a dialysis method to evaluate drug release profile of the nanoparticles. Changes in the hydrodynamic size following incubation in lung artificial fluids was tested by DLS to investigate the colloidal stability of the nanoparticles. A549 cells which are human alveolar basal epithelial cells were then exposed to the nanoparticles to identify formulation that induced acute cytotoxicity using high throughput techniques such as high content screening (HCS). The cytotoxicity of the synthesised nanoparticles was also examined by LDH assay for three different cell lines, including murine macrophage, RAW 264.7, Lewis lung carcinoma, LLC, and A549. Following this, a range of qualitative studies (prussian blue assay, ferrozine assay, and fluorescent microscope) were carried out to study the nanoparticles interaction with cells, and to identify rate of cellular uptake and intracellular localisation. For nebulisation studies we established a collaboration with Aerogen Ltd. In the first step, the size and the volume of the pre- and post-nebulisation nanoparticles were compared by DLS to ensure the nebuliser does not impact on the nanoparticles. Further studies identified the best nanoparticles concentration for the nebulisers with a maximum drug delivery without vibrating mesh clogging. Laser diffraction techniques was employed to

evaluate the volume mean diameter (VMD), the geometric standard deviation (GSD) and the fine particle fraction (FPF) of the nebulised nanoparticles. Two different methods, including mechanical ventilator and human birthing simulator were performed to investigate the drug delivery efficiency for unconscious patients and conscious patients, respectively. We also examined the ability of the nanoparticles to inhibit MIF-induced cell proliferation in an *in vitro* LLC model.

## 2.2 Synthesis of the nanoparticles

HPLC grade and endotoxin-free solvents were obtained from Sigma-Aldrich. The NPs synthesised by using an oil in water (o/w) or single emulsion-solvent evaporation technique. Oleic acid-stabilised  $\text{Fe}_3\text{O}_4$  NPs 40  $\mu\text{l}$  solution (25 mg/ml in  $\text{CH}_2\text{Cl}_2$ ) was added to Acetone: dichloromethane (4 ml, 1:2 w/v) at room temperature. To this was added 1:1 (wt. ratio) PLGA (100 mg) and SCD19 (10 mg). The mixture was stirred and 2% (w/v) poly (vinyl alcohol) (PVA, 8 ml), was added slowly dropwise. The emulsion formed was homogenised using a probe sonicator (Sonics Vibra-Cell™ Ultrasonic, Sandy Hook, USA) (70% amplitude, 30 sec) and poured into 50 ml 0.2% PVA. The resulting emulsion was stirred with an overhead stirrer (Lab egg, IKA® RW 11, Staufen im Breisgau, Germany) 16 h to allow the organic solvents to evaporate. NPs were then recovered by centrifugation ( $21,000 \times g$ , 10 minutes,  $4^\circ\text{C}$ ), washed three times with water (50 ml) and re-suspended in saline (0.9% NaCl) (1 ml) and stored  $4^\circ\text{C}$  until use (see Figure 2.1).

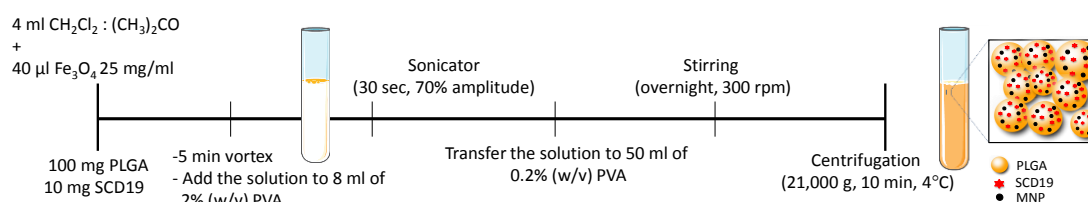


**Figure 2.1:** Schematic diagram describing the synthesis process of PLGA-MNP-SCD19. Image adapted from reference [171].

### 2.3 Limulus amoebocyte lysate (LAL) assay

The newly synthesised PLGA-MNP-SCD19 was analysed and compared to old batches of the nanoparticles to determine the levels of LPS contamination using a Pierce LAL chromogenic endotoxin quantitation assay kit (Thermo Scientific, Dublin, Ireland). Briefly, the standard solutions were prepared in 1, 0.5, 0.25, 0.1 EU/ml concentrations from 24 EU/ml LPS stock according to the manufacturer's specification. 50  $\mu$ l NPs were mixed with 50  $\mu$ l LAL reagent in a pre-warmed 96-well plate and incubated for 10 minutes at 37°C followed by the addition of 50  $\mu$ l substrate solution provided by the kit. Finally, the stop reagent 50  $\mu$ l (acetic acid, 25% (v/v) in water) was added into each well. Absorbance (OD) was measured at 405 nm using an UV-spectrometer (SpectraMax i3x, California, USA). The correlation between absorbance and endotoxin concentration is linear in the 0.1-1.0 EU/ml range. The developed colour intensity is proportional to the amount of endotoxin present in the sample and can be calculated using a standard curve.

### 2.4 Transmission Electron Microscope (TEM)

To obtain quantitative measurement of the nanoparticles size, one drop of the NPs (20  $\mu$ l) suspension was diluted in 10 ml water and 100  $\mu$ l of this solution were deposited on a 100-mesh copper grid covered with amorphous carbon film (Electron Microscopy Sciences, Hatfield, USA). Samples were incubated for 15 minutes under ventilation to allow for complete drying, and then redundant solutions were absorbed with a filter paper. After that each sample was examined by a JEOL 2100 LaB Transmission Electron Microscope (JEOL Ltd., Tokyo, Japan) at 100 kV. The average particle size was calculated from measuring 100 nanoparticles in random fields of view.

## 2.5 Scanning Electron Microscope (SEM)

A scanning electron microscope (Zeiss NEON 40 EsB Cross Beam, Billerica, USA) was used to observe the morphology of the NPs. The nanospheres were prepared by sprinkling onto a Silicon wafers (30  $\mu$ l) and allowing them to dry which was then gently tapped on a piece of clean aluminium foil on a work bench to remove excess nanosphere before being loaded into a Sputter Coater machine (Cressington Scientific, Watford, UK) where they were coated by the platinum for 2 minutes at 13 mA to fix the samples and protect from thermal damage as well as provide a proper secondary electron that improves the quality of the images. Then, the samples were analysed by the scanning electron microscopy. An acceleration voltage of 10 keV was used with no visible damage to the nanosphere surfaces observed.

## 2.6 Nano tracking analysis (NTA)

The measurement of nanoparticle hydrodynamic swelling size was carried out by NTA technique using a NanoSight equipped with a 50 mW 532 nm laser (Malvern Instruments Ltd., Amesbury, UK), running NTA version 3.1. The device records and tracks the Brownian motion of NPs in solution in 2 dimensions. The determination of average distance travelled by each particle in the x and y direction allows the particle diffusion coefficient to be determined. The fluidic system and sample stage were primed with 0.1  $\mu$ m filtered DNase/RNase free water. Calibration was conducted prior to loading samples of unknown size to ensure that the sizes were accurately determined. The system was regularly checked prior to introducing a nanoparticle sample for the presence of any contaminating nanomaterials. NPs were dispersed in ultrapure, 20 nm filtered dH<sub>2</sub>O and loaded into the NanoSight machine, following the selection of the appropriate threshold, an automated script was run, and the positioning and motion of individual NPs was tracked. The analysis of each sample was conducted in batch mode, so that a mean hydrodynamic size could be obtained.

## 2.7 Dynamic Light Scattering (DLS)

The particle size distribution and polydispersity index (Pdl) of PLGA-SCD19 and PLGA NPs (control) was performed by dynamic light scattering (DLS), photon correlation spectroscopy, technique on a Zetasizer Nano ZS90 instrument (Malvern, Amesbury, UK). To produce a suitable scattering intensity, the samples were diluted to a suitable concentration by diluting 1:500 (2 $\mu$ l of the NPs to 1.998 ml Milli-Q water). A sample volume of 1 ml was used in 10mm path length cuvettes (Sarstedt, Wexford, Ireland). The size distribution profile and Pdl of the NPs was determined by using a 659 nm/100 mW laser at an angle of 90° in 10 mm diameter cells at 25°C. Measurements were taken in triplicate and the data are the average of all three runs.

## 2.8 Drug loading, drug encapsulation, and yield efficiency

The produced PLGA and PLGA-SCD19 nanoparticles were transferred into screw cap micro tubes and incubated for 1 minute in Liquid Nitrogen (LN2) to snap-freeze. All samples were then placed into a FreeZone 4.5 litre Benchtop Freeze Dryer (Labconco, Kansas, USA) at 0.02 mbar for 72 h, being maintained at the condenser surface temperature of  $-80 \pm 5^\circ\text{C}$ . PLGA-SCD19 NPs (2 mg) were dissolved in 70% DMSO 200  $\mu$ l followed by 10 minutes vigorous vortex. The solution was measured with a validated spectrophotometric method (Spectra Max i3x, California, USA) at 330 nm. The concentration of loaded SCD19 was assessed based on the standard curve that was generated from different known SCD19 concentrations. Each experiment was repeated three times. Drug loading (%DL), drug encapsulation (%EE), and drug yield (%YE) efficiency were calculated using the following equations [43].

$$\text{Drug loading (\%)} = \frac{\text{Weight of the drug in nanoparticles}}{\text{Weight of nanoparticles}} \times 100$$

$$\text{Yield efficiency (\%)} = \frac{\text{Weight of nanoparticles}}{\text{Weight of PLGA and drug fed initially}} \times 100$$

$$\text{Encapsulation efficiency (\%)} = \frac{\text{Weight of the drug in nanoparticles}}{\text{Weight of drug fed initially}} \times 100$$

## 2.9 Stability of the nanoparticles in simulated lung fluids

To investigate the colloidal stability of the NPs in lung artificial fluids, 0.5 mg/ml PLGA-SCD19 that contained 100  $\mu\text{M}$  (0.025 mg/ml) SCD19 and 0.5 mg/ml PLGA NPs (control) were dispersed in saline (control), artificial lung fluid and artificial lysosomal fluid that were prepared prior to the start of the experiment (see Table 2.1). The size and polydispersity index (PDI) of the NPs were investigated after 48 h by using a Zetasizer Nano ZS90 instrument (Malvern, Amesbury, UK).

**Table 2.1:** Simulated Lung Fluids (SLFs). Composition of the synthetic biological fluids used to simulate the physicochemical environment of the artificial lung fluids [172].

Simulated fluid	Chemical name (formula)	Composition per 1 Litre
<b>Artificial Lung fluid (Gamble's solution) (pH 7.4)</b>	Magnesium chloride (MgCl <sub>2</sub> .6H <sub>2</sub> O)	0.2033g
	Sodium chloride (NaCl)	6.0193 g
	Potassium chloride (KCl)	0.2982 g
	Disodium hydrogen phosphate (Na <sub>2</sub> HPO <sub>4</sub> )	0.142 g
	Sodium sulfate (Na <sub>2</sub> SO <sub>4</sub> )	0.071 g
	Calcium chloride dihydrate (CaCl <sub>2</sub> .2H <sub>2</sub> O)	0.3676 g
	Sodium acetate (C <sub>2</sub> H <sub>3</sub> NaO <sub>2</sub> )	0.9526 g
	Sodium hydrogen carbonate (NaHCO <sub>3</sub> )	2.6043 g
<b>Artificial lysosomal fluid (pH 4.5)</b>	Sodium citrate dihydrate (Na <sub>3</sub> C <sub>6</sub> H <sub>5</sub> O <sub>7</sub> )	0.097 g
	Sodium chloride (NaCl)	3.21 g
	Sodium hydroxide (NaOH)	6 g
	Citric acid (C <sub>6</sub> H <sub>8</sub> O <sub>7</sub> )	20.8 g
	Calcium chloride dihydrate (CaCl <sub>2</sub> .2H <sub>2</sub> O)	0.1285 g
	Trisodium phosphate (Na <sub>3</sub> PO <sub>4</sub> .12H <sub>2</sub> O)	0.2347 g
	Sodium sulfate (Na <sub>2</sub> SO <sub>4</sub> )	0.039 g
	Magnesium chloride (MgCl <sub>2</sub> .6H <sub>2</sub> O)	0.106 g
	Glycerine (C <sub>3</sub> H <sub>8</sub> O <sub>3</sub> )	0.059 g
	Sodium citrate dihydrate (Na <sub>3</sub> C <sub>6</sub> H <sub>5</sub> O <sub>7</sub> .2H <sub>2</sub> O)	0.077 g
	Sodium tartrate dihydrate (C <sub>4</sub> H <sub>4</sub> Na <sub>2</sub> O <sub>6</sub> .2H <sub>2</sub> O)	0.09 g
Sodium lactate (C <sub>3</sub> H <sub>5</sub> NaO <sub>3</sub> )	0.085 g	
Sodium pyruvate (C <sub>3</sub> H <sub>3</sub> NaO <sub>3</sub> )	0.086 g	
Formaldehyde (CH <sub>2</sub> O)	1 mL	

## 2.10 Drug Release

The freshly prepared PLGA-SCD19 NPs (3 ml) which contained 100 µM (0.025 mg/ml) SCD19 were injected into a Slide-A-Lyzer MINI dialysis cassette (Thermo Fisher Scientific, Dublin, Ireland) of 3.5K MWCO pore size. The dialysis cassette was then immersed in a water bath (20 litre) and kept under shaking (150 rpm). To assay the amount of SCD19 remaining inside particles at predetermined intervals (0, 2, 4, 6, 24, 48, 72 h), 180 µl sample was collected from inside the dialysis cassette. Then the volume of each sample was adjusted to 500 µl by adding DMSO and vortexed vigorously for 5 minutes to dissolve the NPs properly. The concentration of SCD19 in each collected sample was assessed by a Varian Cary 50 UV-vis (Agilent Technologies, California, USA) in a quartz cuvette with 1 cm path length and 0.5 ml capacity for the 330 nm peak.

The samples were measured in triplicate. The SCD19 release percentage was obtained according to:

$$\text{Drug release (\%)} = (D_t/D_0) \times 100$$

where  $D_t$  and  $D_0$  indicate the amount of SCD19 released from the PLGA NPs suspension at certain intervals and the total amount of drug in the PLGA NPs suspension, respectively.

## 2.11 Cell culture

The A549 lung carcinoma cell line, was kindly provided by Prof. Yuri Volkov (Department of Clinical Medicine, Trinity Collage Dublin) and the Lewis Lung carcinoma cell line (LLC) was directly sourced from ATCC (Manassas, Virginia, USA). All required reagents and medium to culture the cell lines were purchased from (Gibco, Life Technologies, California, USA). Both cell lines were maintained in DMEM medium supplemented with 10% FBS, 100 U/ml penicillin and streptomycin and 2 mM L- Glutamine. All cell lines were grown at 37°C in a humidified atmosphere containing 5% CO<sub>2</sub>. Cells were passaged every 2-3 days when they reached 80-90% confluency. Cells were not allowed to form a complete monolayer or dense colonies. To passage the cells, growth medium was removed from the cells and the monolayer washed once with PBS and detachment was induced by adding 5ml of 0.05% Trypsin-EDTA (1.5 ml/75 cm<sup>2</sup> surface area) for 3 minutes at 37°C. Trypsin was neutralised by adding medium (4 mL/75cm<sup>2</sup>). The cell pellet was collected by centrifugation and cells were reseeded at a ratio of 1:5 to 1:10 depending upon the length of time needed before cells were used for experiments.

## 2.12 High Content Screening (HCS)

A549 cells were seeded in 96-well Plates ( $4 \times 10^3$  cells/well), exposed to different NPs 100 µg/ml (PLGA-MNP-SCD19, PLGA-MNP, PLGA, and MNP) for 24 h. After washing three times with pre-warmed PBS (Gibco™, Glasgow, UK), the cells were fixed by incubating them for 20 minutes with 4% paraformaldehyde

solution (Sigma-Aldrich, Zwijndrecht, the Netherlands). Adherent cells were then fluorescently stained with Rhodamine phalloidin (Invitrogen, California, USA) to visualise the cellular actin and Hoechst 33342 (Invitrogen, California, USA) to visualise the nuclei. Then, the plates were scanned (six randomly selected fields/well) using an automated microscope IN Cell Analyzer 1000 (GE Healthcare, London, UK) and the acquired images were automatically analysed by the IN Cell Investigator software (v1.9 version). Images were acquired at 10 X magnification using two detection channels (DAPI-FITC-Texas Red filter cube set). The DAPI filter (channel 1) enabled detection of blue fluorescence indicating nuclear staining at a wavelength of 460 nm; the FITC filter (channel 2) enabled detection of red fluorescence indicating actin filament staining at a wavelength of 620 nm. A pseudo-coloured merged image was generated according to a pre-defined colour scheme, with nuclei coloured blue and actin coloured red according to their emission wavelength. Cell count number, cell area, nuclei area, nuclei Intensity and cell Intensity were determined to measure nanoparticles toxicity.

### 2.13 Lactate dehydrogenase assay (LDH assay)

A549, LLC, RAW 264.7 cell lines were plated at  $1 \times 10^4$ /ml in 450  $\mu$ l of medium in a 48 well plate. 16 hours later cells were treated for 72h with a serial dilution of PLGA-SCD19 NPs (0.1, 0.5, 1 and 2 mM of encapsulated SCD19) corresponding to PLGA-SCD19 NPs. After that, 5  $\mu$ l of lysis buffer was added to untreated wells and incubated at 37°C for a further 30 minutes to ensure full lysis as a 100% toxic control. The LDH release assays were measured using a LDH assay kit (Roche Diagnostics, Dublin, Ireland) according to the manufacturer instructions. The cell viability (%) was calculated according to the following equation:

$$\text{Cytotoxicity (\%)} = \frac{\text{OD (test)} - \text{OD (blank)}}{\text{OD (negative control)} - \text{OD (blank)}} \times 100$$

OD (test) = treated cells

OD (blank) = medium + NPs

OD (negative control) = lysed cells

## 2.14 Cellular uptake of nanoparticles in the cells

Perls' Prussian blue stain, which reveals the presence of iron, was performed on the A549 to visualise the cellular uptake of PLGA-MNP-SCD19 NPs. A549 cells were seeded at a density of  $2 \times 10^4$  cells/well in the 8-well chambered cell culture slides (Falcon™, Lowell, USA) and after overnight incubation the cells were exposed to different concentrations of PLGA-MNP-SCD19 NPs (50, 100, and 200  $\mu\text{g/ml}$  based on MNPs concentration) for two different time points, 24h and 48h. After the time points, the treated cells were washed three times by pre-warmed PBS (Gibco™, Glasgow, UK) and fixed using 4% Paraformaldehyde (Sigma-Aldrich, Zwijndrecht, the Netherlands). The chamber was removed, and slides allowed to air dry. Equal parts of 4% hydrochloric acid and 4% potassium ferrocyanide were prepared (Potassium ferrocyanide staining solution, appendix 1) immediately prior to use and slides were immersed in this solution for 20 minutes. Following incubation, the slides were then dipped in double-distilled water three times and counterstained with 0.5% Neutral Red for 2 minutes to stain the nucleus of the cells. Slides were rinsed a further two times with distilled water and allowed to air dry. Finally, the slides were cover slipped with D.P.X (Sigma-Aldrich, St. Louis, USA). Imaging was completed 24h post mounting using the Nikon E800W microscope with 20x and 40x objectives. Images were acquired using the micropublisher 3.3RTV colour camera (photometrics, Arizona, USA).

## 2.15 Confocal microscopy

The uptake of PLGA-MNP-SCD19 NPs and control MNPs were visualised using confocal microscopy. A549 cells were seeded at a density  $2 \times 10^4$  cells/well in a the 8-well chambered cell culture slide (Falcon™, Lowell, USA), treated with MNPs (100 µg/ml), PLGA-MNP-SCD19 NPs (100 µg/ml based on MNPs concentration) for 24h, then the cells were thoroughly washed two times in PBS (Gibco™, Glasgow, UK). and fixed using 4% Paraformaldehyde (Sigma-Aldrich, Zwijndrecht, the Netherlands) for 10 minutes, followed by washing with PBS (Gibco™, Glasgow, UK). Then, staining using fluorescent dyes was performed. Briefly, 100 µl of 10 µg/ml Hoechst 33342 (Invitrogen, California, USA) for nuclei and Rhodamine phalloidin (Invitrogen, California, USA) for F-actin filaments in PBS (Gibco™, Glasgow, UK) was added to each well and allowed to incubate 2h at ambient temperature. After three times washes with PBS (Gibco™, Glasgow, UK), coverslips were mounted on glass slides with transparent mounting medium (VECTASHIELD, Vector Laboratories Inc., USA) and sealed. PLGA-MNP-SCD19 NPs and MNPs cellular internalisation was evaluated by Laser Scanning Confocal Microscopy (LSCM). LSCM imaging and analysis was carried out with equipped with a Zeiss LSM 5 software (Carl Zeiss Microscopy GmbH, Jena, Germany). MNPs were imaged in reflectance mode at  $\lambda_{exc} = 561$  nm.

## 2.16 Colorimetric ferrozine-based assay

The colorimetric ferrozine-based assay allows the quantification of iron in cultured cells. A549 cells seeded in 24-well plates were incubated with different concentrations of MNP-PLGA-SCD19 (50, 100, and 200 µg/ml based on MNPs concentration) and intracellular accumulation of the NPs were quantified after 24h and 48h incubation. Briefly, the cells were lysed with 0.5 ml of 50 mM NaOH (Sigma-Aldrich, UK) per well and 2h incubation on the shaker. The lysed cells were then transferred to 1.5 ml microtube and mixed with 500 µl of 10 mM HCl, and 500 µl of fresh iron-releasing reagent (a freshly mixed solution of 1:1 volumes of 1.4 M HCl and 4.5% (w/v)  $\text{KMnO}_4$  in  $\text{H}_2\text{O}$ ) (see appendix). After that,

the microtapes were incubated for 2h at 60°C within a fume hood, since chlorine gas is produced during the reaction, this step was followed by 1h incubation at room temperature to cool down the samples. Finally, 150 µl of iron-detection reagent (see appendix) were added to each tube. After 30 min incubation in room temperature, 0.5 ml of the solution obtained in each tube was transferred into a well of a 24-well plate, and absorbance was measured at 570 nm (SpectraMax i3x, Molecular Devices, San Jose, USA). Iron content of the sample was calculated by comparing the absorbance of the sample to standard curve that had been prepared in a way like that of the sample (mixture of 100 µl of FeCl<sub>3</sub> standards (0–300 µM) in 10 mM HCl, 100 µl 50 mM NaOH, 0.5 ml releasing reagent, and 1.5 ml detection reagent) (see appendix).

## 2.17 The nebuliser efficiency assay

A serial dilution of the PLGA-SCD19 NPs (8 mg/ml, 16 mg/ml, 40 mg/ml) was prepared in saline and H<sub>2</sub>O (see Table 2.2).

**Table 2.2:** The concentration and volume of NPs prepared for nebulisation studies with Aerogen nebuliser.

PLGA-SCD19 concentration (mg/ml)	Volume of the samples in saline (ml)	Volume of the samples in H <sub>2</sub> O (ml)
8	2	2
16	2	2
40	2	2

An autoclavable vibrating mesh nebuliser (VMS) (Aerogen Solo, Aerogen, Galway, Ireland) was used to nebulize the samples. To avoid vibrating mesh clogging issues, the samples were run from low (0.06 mg/ml) to high (40 mg/ml) concentration. Before loading each sample, 1 ml of saline was nebulised to remove the NPs left in the nebuliser. One ml of each concentration was loaded into the nebuliser then, the nebuliser was placed on the 50 ml falcon and sealed with parafilm. One small hole was made on the parafilm to avoid the build-up of pressure which may interfere with the vibrating mesh during nebulisation. After nebulisation, the falcon was shaken vigorously for 30 seconds to detach the

delivered NPs that have deposited/sedimented/dried onto the walls of the falcon tube and finally the nebulised samples were collected *via* centrifuge at 2000 g, 5 minutes, 4°C. After running each sample, the vibrating mesh was washed to ensure that there is no blocking issue for next sample. To clean the vibrating mesh, the nebuliser was turned upside down and a certain amount of saline (50 µl) was placed on the vibrating mesh, then the nebuliser was turned on. Once the saline has been sucked into the mesh and disappear the nebuliser was turned off immediately. Finally, saline (1 ml) was loaded into the nebuliser cup and nebulised into a new falcon. To assess the efficiency of nebulisation of each concentration of NPs 1) the time required to nebulise 1 ml of NPs, 2) the volume of NPs collected in the falcon tube from the nebuliser, and 3) the concentration of NPs in the falcon tube after nebulisation were recorder/measured. The size distribution of the NPs was investigated by a dynamic light scattering (DLS) (Malvern Instruments Ltd., Amesbury, UK), and compared to the sample before nebulisation. The volume of delivered sample was also determined by Thermo fisher micropipette. Sample concentration was measured by Varian Cary 50 UV-VIS in a quartz cuvette with 1 cm path length and 1 ml capacity.

## 2.18 Laser diffraction

The Volume Median Diameter (VMD) and Geometric Standard Deviation (GSD) of the aerosolised PLGA-SCD19 (16 mg/ml) were determined by using a Malvern Spraytec particle size analyser with RT Sizer software (version 5.60). The NPs were nebulised by a vibrating mesh nebuliser (Aerogen Solo, Aerogen, Galway, Ireland) without the holding chamber as recommended by the Aerogen technical supporter. Nebulisers were connected to the inhalation cell and aspiration was carried past the laser by means of a vacuum pump set to 20 L/min, ensuring laminar flow and reducing artificial droplet size growth through collision with other droplets. The vacuum also ensured that the droplets passed through the laser beam only once. The centre of the emitted aerosol plume was

directed through the centre of the laser beam to increase the accuracy of data acquisition. The data acquisition rate was set to 500 Hz, that is, 500 individual readings per second were taken characterising the droplet size distribution. The value reported for each individual measurement is an average of the individual readings recorded over the course of the dose. All experiments were performed at room temperature and ambient relative humidity (40%–60%).

## 2.19 Cascade Impactor

To determine the relative amount of deposition of the nanoparticles in the different regions of the lung and Mass Median Aerodynamic Diameter (MMAD), the PLGA-SCD19 NPs were nebulised by a vibrating mesh nebuliser (Aerogen Solo, Aerogen, Galway, Ireland) in to a Next Generation Impactor (NGI) (Copley Scientific Ltd., Nottingham, UK) that was operated at 15 L/min at room temperature. The droplet size cut-off points were set at 14.1, 8.61, 5.39, 3.3, 2.08, 1.36, 0.98, and 0.70  $\mu\text{m}$ , respectively, for each of the eight stages of the cascade impactor. After nebulisation of PLGA-SCD19 (1ml) (16 mg/ml), each plate of the impactor and the throat were rinsed with 5 ml and 10 ml of PBS (Gibco™, Glasgow, UK), respectively. The amount of SCD19 recovered from each stage filter was determined with the use of a spectrophotometer (SpectraMax, Molecular Devices, California, US) by measuring the absorbance at 330 nm and interpolation on a standard curve of SCD19 concentrations. Data were expressed as the percentage of total drug deposited on all stages of the impactor including the throat and was represented by the mean  $\pm$  standard deviation ( $n = 3$ ). The Fine Particle Fraction (FPF),  $\text{FPF}_{5 \mu\text{m}}$ , equivalent to the respiratory fraction to target lung and the fine particle fraction,  $\text{FPF}_{2 \mu\text{m}}$ , equivalent to alveolar fraction to target alveoli were calculated as the percentage of aerosol particles  $< 5 \mu\text{m}$  and  $< 2 \mu\text{m}$ , respectively (ISO 27427) relative to the total emitted dose by the Next Generation Impactor.

## 2.20 Human Breathing Simulator and Human mechanical

### ventilator

To simulate a spontaneously breathing adult, A breathing simulator (ASL5000, Ingmar Medical, Pittsburgh, USA) was used. The breathing simulator was programmed to simulate the recorded human breathing patterns with adult setting (inhalation: exhalation ratio 1:3, 15 breaths/ min, and tidal volume 500 ml). A vibrating mesh nebuliser (Aerogen Solo, Aerogen, Galway, Ireland) was placed on the system (see Figure 2.2) to nebulise the nanoparticles and at the end of the system a bacterial/viral filter (Respirgard II 303, Baxter, Ireland) was also placed to collect the nebulised NPs.

To simulate a mechanically ventilated adult, a Maquet SERVO-i mechanical ventilator (Getinge, Sweden) was used. Breathing parameters were inhalation: exhalation ratio 1:1, 15 breaths/ min, and tidal volume 500 ml. Active humidification was supplied to the limb circuit by a hot pot humidifier (Fisher & Paykel, Auckland, New Zealand). The bacterial/viral filter (Respirgard II 303, Baxter, Ireland) was placed before the humidifier while the nebuliser was placed at the limb circuit (see Figure 2.3).

For both breathing simulator and mechanical ventilator, a nominal dose of 1ml (16 mg/ml) PLGA-SCD19 NPs was nebulised in each test run. The amount of NPs captured in the filter was considered the lung dose. The filter was removed upon completion of the run time, eluted 10 ml of PBS (Gibco™, Glasgow, UK), and the washings were tested for SCD19 with an UV spectrophotometry (Biochro, Cambridge, UK) and interpolation on a standard curve at 330 nm. All test iterations were run in triplicate.

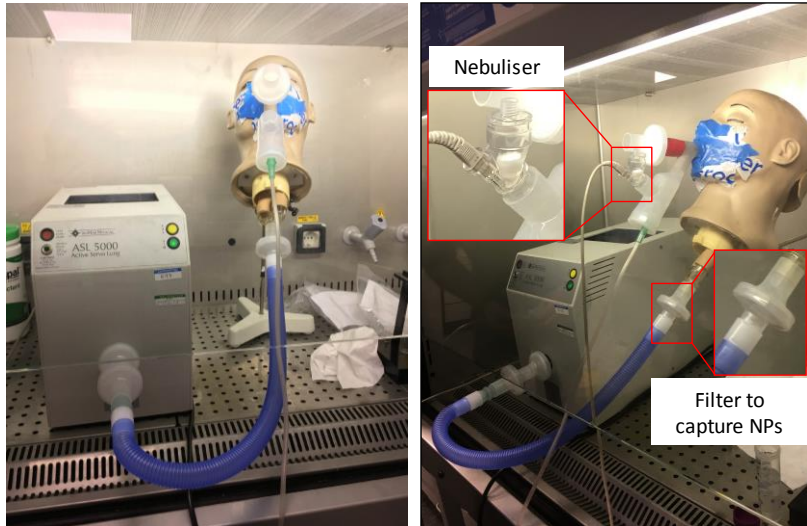


**Figure 2.2:** The human breathing simulator machine. The aerosolised nanoparticles are delivered via limb circuit attached to the machine and the sample are captured by a bacterial/viral filter (Respirgard II 303, Baxter, Ireland). Breathing parameters were inhalation: exhalation ratio 1:3, 15 breaths/ min, and tidal volume 500 ml.

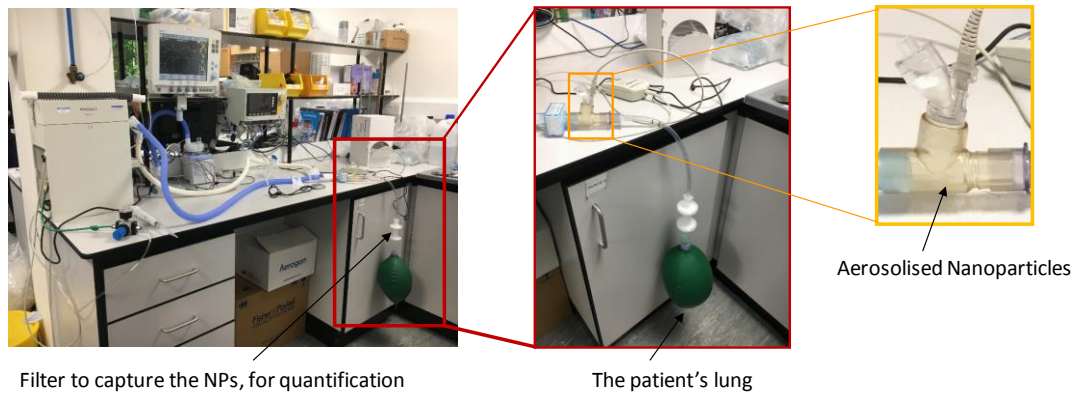


**Figure 2.3:** The human mechanical ventilator. The aerosolised nanoparticles are delivered via dual limb circuit attached to the ventilator and the nanoparticles are captured by a bacterial/viral filter (Respirgard II 303, Baxter, Ireland). Breathing parameters were inhalation: exhalation ratio 1:1, 15 breaths/ min, and tidal volume 500 ml.

## 2.21 Generation of recombinant MIF (rMIF)

Transformed *E.coli* BL21 (DE3) bacteria (kindly donation from Prof. Richard Bucala Yale school of medicine, USA) containing the pET11b-MIF

construct was verified by cultured in selective medium consist of 50 µg/ml Ampicillin (Santa Cruz Biotechnology, Inc. Dublin, Ireland) according to antibiotic resistance marker of pET11 vector in Luria Berttani (LB) broth (Sigma-Aldrich, USA) and LB agar (Sigma-Aldrich, USA) medium (see Appendix). In addition, the transformed bacteria were examined using the colony PCR method for detection of the inserted human MIF gene into the plasmid. Colony PCR is a commonly used, valid and quick screen method for plasmids containing a desired insert directly from bacterial colonies by using specific primers for targeted DNA fragment (see Figure 2.4).

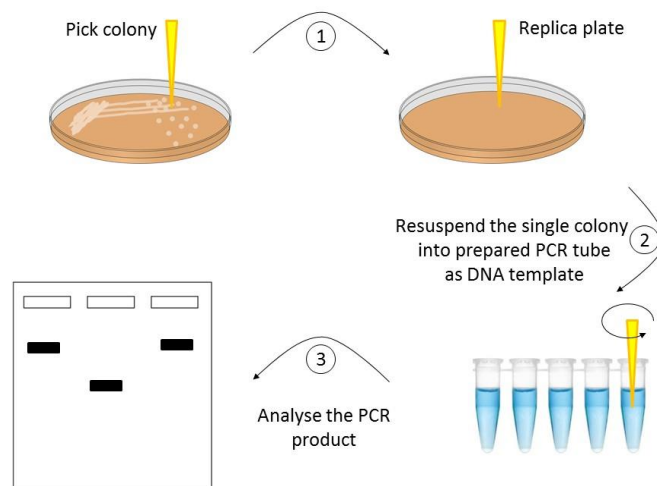


**Figure 2.4:** Schematic processing of the PCR colony method.

Briefly, Transformed bacteria were cultured on LB agar with appropriate antibiotic (50 µg/ml Ampicillin) at 37°C for overnight, then several single colonies were picked up, using the yellow sterile tips for preparation a replica plate, after that each yellow tip was placed in a ready to use PCR master mix (25 µl) (Bioline, MyTaq Red Mix, Dublin, Ireland) and shaken to release/detached the remained bacteria to provide DNA template for the primers. Then, the PCR programme (see Table 2.3) was run after incubation of the PCR tube for 10 minutes at 94°C

to breakdown the bacteria for exposing the recombinant plasmid to specific primers (100 pmol/ $\mu$ l) (see Table 2.4).

**Table 2.3:** Colony PCR Program.

Cycles	Time	Temperature	Process
1	10 minutes	94°C	plasmid exposition
	1 minute	94°C	denaturation
32	1 minute	55°C	annealing
	1 minute	72°C	extension
1	5 minutes	72°C	final extension

**Table 2.4:** Specific primers for MIF human cDNA gene cloned in pET11b.

<b>Forward primer</b>	5'-CCATATGCCGATGTTTCATCGTAAACAC-3'
<b>Reverse Primer</b>	5'-CGGATCCTGCGGCTCTTAGGCGAAGG-3'

### 2.21.1 Agarose gel electrophoresis

PCR products were subjected to electrophoresis in 0.8% agarose (Invitrogen, Dublin, Ireland) dissolved in Tris-Boric-EDTA (TBE) buffer (1M Tris base, 0.02M EDTA, 1M boric acid) (appendix 1) consist of 3% SYBR™ Safe DNA Gel Stain (Invitrogen, Dublin, Ireland). A 6X gel loading dye solution (Bio Labs, Broadheath, Altrincham, UK) was mixed 1 $\mu$ l per 5  $\mu$ l PCR product prior to load into the agarose gel electrophoresis. Electrophoresis was carried out in an electrophoresis tank and the power source was a consort regulated high-voltage power supply (Topac Inc., model E865, Cohasset MA, USA) and the electrophoresis was carried out at 400 mA, 100 V, for 45 minutes or until the dye passed two in third of the gel.

### 2.21.2 Extraction and purification of human rMIF

*BL21 (DE3)* cells transformed by pET11b-hrMIF were grown in 1 litre LB broth at 37°C until the OD 600 nm reached 0.6-0.8. Isopropyl 1-thio-P-D-

galactopyranoside (IPTG) (Sigma-Aldrich, Gillingham Dorset, UK) was added to a final concentration of 1 mM and the incubation continued at 37°C for an additional 3 h. Bacteria were harvested by centrifugation and stored at -80°C. For purification, cell pellets were suspended in Tris-buffered saline (50 mM Tris-HCl, pH 7.5) and stirred overnight at 4°C. Benzonase (20 µl at 250 units/µl) (Sigma-Aldrich, St. Louis, USA) and 2x cOmplete™ EDTA-free protease inhibitor cocktail (Roche, Mannheim, Germany) were added and incubated for 1 hour at 4°C. The cells were then lysed via sonication (30 seconds on, 30 seconds off, 20% amplification, 3 times) and centrifuged at 14000 x g for 20 minutes at 4°C. The supernatant was then filtered using a 0.45 µm syringe filter (Millex, Cork, Ireland), followed by a 0.22 µm syringe filter (Millex, Cork, Ireland) and loaded onto a HiPrep™ Q Fast Flow 16/10 (GE Healthcare Bio-Science, USA) an ion exchange column and eluted with Tris-buffered saline (50 mM Tris-HCl pH 7.5). Recombinant human MIF elutes in the first flow through fractions. These fractions were concentrated using a centrifugal filter MWCO 10,000 (Amicon® Ultra, Cork, Ireland) and loaded into a HiLoad 16/600 superdex 200pg (GE Healthcare Bio-Science, USA) gel filtration column and eluted with Tris-buffered saline. Fractions containing MIF were pooled, concentrated and stored in PBS (Gibco™, Glasgow, UK) at -80°C. The purity, concentration and activity of the rMIF were then assessed by employing SDS-PAGE, BCA protein assay and cell free tautomerase assay. Figure 2.5 illustrates schematically and briefly the expression and purification of rMIF protein.

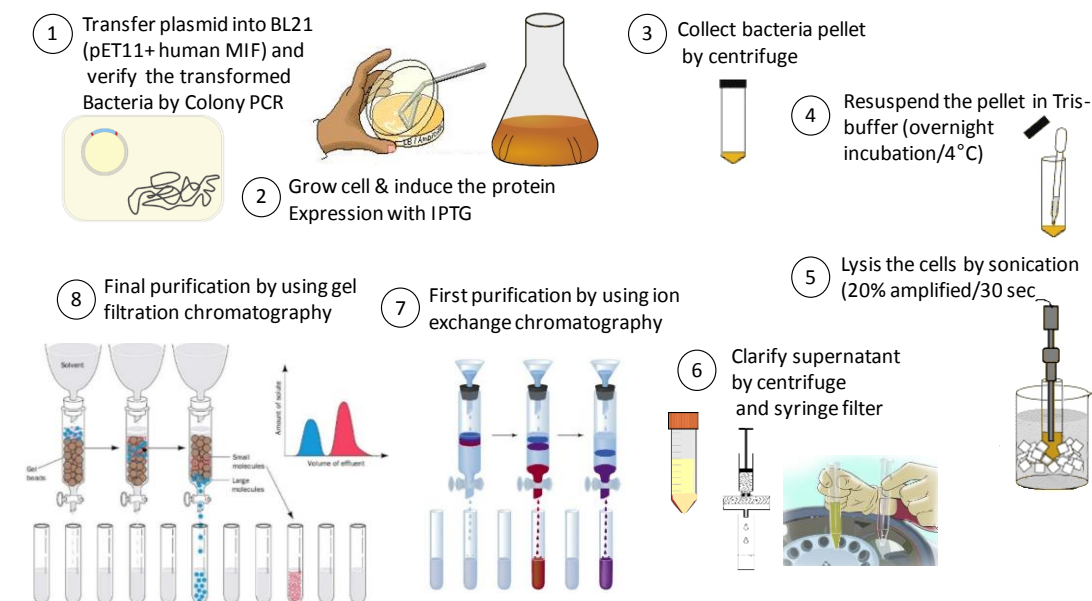


**Figure 2.5:** Schematic diagram illustrating human recombinant MIF expression and purification procedure.

### 2.21.3 Sodium dodecyl sulfate polyacrylamide gel electrophoresis

The molecular weight of the recombinant human MIF was determined by separation of whole cell lysates by Sodium dodecyl sulfate polyacrylamide gel electrophoresis (SDS-PAGE). The discontinuous SDS system was used using a 12% concentration of the Mini-protean TGX Precast Gel (Bio-Rad, California, USA) in the resolving gel. Samples were prepared by adding the sample buffer and boiling for 5 minutes before loading onto an SDS-PAGE. The running buffer consisted of 1 g SDS (Fisher chemical, Dublin, Ireland), 3.03 gr Trizma<sup>®</sup> base (Sigma-Aldrich, St Louis, USA) and 14.04 g Glycine (Sigma-Aldrich, St Louis, USA) in 1000 ml dH<sub>2</sub>O (see appendix). The samples were subjected to electrophoresis at 10 mA and 15 mA in stacking and resolving gel, respectively. Finally, the gel was stained with Coomassie<sup>®</sup> Brilliant blue R 250 (Merck, Dublin, Ireland) after fixation of the gel by incubation in the fixation solution (see appendix) for 15 minutes with shaking. Finally, the SDS-PAGE gel was incubated for 4h in de-staining solution (see appendix).

#### **2.21.4 Endotoxin removal**

The endotoxin (LPS) was depleted from rMIF recombinant protein by employing Pierce® High-Capacity Endotoxin Removal Resin. The column was regenerated by 3.5 ml of 0.2N NaOH for 24 h, one day prior to the experiment. After removing the NaOH by centrifuge (500 ×g, 1 minute, 4°C), the column was washed two times by NaCl (2M) and LPS free water, respectively, and each time the centrifuge (500 ×g, 1 minute, 4°C) was applied to remove the liquids. The LPS contaminated rMIF (1 ml) was added on the column and then it was placed on a rotator at 4°C for overnight. Finally, the column was placed on a clean 15 ml falcon and centrifuged (500 ×g, 1 minute, 4°C) to collect LPS free rMIF.

#### **2.21.5 BCA protein assay**

The concentration of rMIF was measured with bicinchoninic acid (BCA) assay (Pierce™ BCA Protein Assay Kit, Thermo Scientific Inc., Waltham, USA). Briefly, the BCA working reagent was prepared by mixing two reagents provided by the kit, the reagents A and reagent B in the ratio of 50:1. The Bovine serum albumin (BSA) (provided by the kit) was used to prepare standard solution. From a stock solution of 2 mg/ml dilutions with concentrations of 25, 125, 250, 500, 750, 1000, 1500, and 2000 µg/ml were made. The prepared standards and samples (25 µl/well) were pipetted into a 96 well plate, each in triplicate. Then the BCA working reagent (200 µl/well) was added and the plate was shaken for 30 seconds by using a plate shaker, followed by 30 minutes incubation at 37°C. After cooling down the plate at room temperature, the plate was read at UV max of 562 nm (SpectraMax i3x, Molecular Devices, San Jose, USA). Protein concentration of a sample was determined using the standard curve obtained by prepared standards.

#### **2.21.6 Cell free tautomerase assay**

To prepare the MIF's non-physiological substrate, L-dopachrome methyl ester was prepared at 2.4 mM through oxidation of L-3,4-

dihydroxyphenylalanine methyl ester (L-dopachrome methyl ester) with sodium periodate. The substrate solution was mixed well and placed at room temperature for 5 minutes before being placed on ice in the dark. rMIF (100 ng/ml) was added to each of the Tautomerase Inhibitor (PLGA-SCD19 or SCD19) at the concentrations of 100  $\mu$ M. The decrease in absorbance was monitored every 25 seconds for 10 minutes with a spectrophotometer at 475 nm.

## 2.22 TNF- $\alpha$ ELISA

RAW 264.7 cells were seeded at density of  $1 \times 10^5$  cell/ml in 450  $\mu$ l of medium in a 48 well plate. After overnight incubation cells were treated with LPS free rMIF (100 and 500 ng/ml) for 24h. Then, supernatants were collected to determine TNF- $\alpha$  level via a TNF- $\alpha$  specific ELISA (R&D Systems, UK) as an adaptation of the procedure provided by the manufacturer. Briefly, 96 well plates were coated with 50  $\mu$ l of capture antibody (0.8  $\mu$ g/ml) in PBS and sealed and incubated overnight at 4  $^{\circ}$ C. After washing the plate three times with 0.05% PBS Tween and plates blotted dry, it was blocked by adding 150  $\mu$ l/well of 1% BSA (Sigma Aldrich, Dublin) in PBS (Gibco, Life Technologies, California), following two hours incubation at room temperature and washing again as described. 50  $\mu$ l/well of detection antibody (200 ng/ml) in 1% BSA was added and incubated for two hours at room temperature. After washing the plate, 50  $\mu$ l of working concentration of Streptavidin-HRP was added to each well and plates were covered and incubated for 20 minutes at room temperature. 50  $\mu$ l/well of substrate solution (1 OPD (o-phenylenediamine dihydrochloride) tablet and 1 urea hydrogen peroxide/buffer tablet dissolved in 20 ml of water to yield a ready to use buffered substrate solution, Sigma Aldrich, Dublin) was added and incubated for 20 minutes at room temperature. Finally, 25  $\mu$ l of 2N H<sub>2</sub>SO<sub>4</sub> (Sigma Aldrich, Dublin) was added to each well to stop the reaction. The optical density of each well was then measured with a spectrophotometer at 450 nm.

## 2.23 MTT assay

Inhibition of Lewis lung carcinoma cell (LLC) growth was determined by using an MTT (3-[4,5-dimethylthiazol-2-yl] 2,5-diphenyltetrazolium bromide) cell proliferation assay. Briefly, the LLC cells ( $2 \times 10^2$  per well) were seeded in a 48-well plate in DMEM without FBS. After being serum starved overnight, the cells were exposed to the nebulised NPs PLGA-SCD19 (100  $\mu$ M encapsulated SCD19), also the cells were treated by free-SCD19 and PLGA NPs as the controls. Background control contained only culture medium without cells. Cells without treatment were included as a maximum cell growth point. After overnight incubation, the cells were stimulated by rMIF (100 ng/ml) for two days, then individual wells were treated for 4 hours at 37°C with 20  $\mu$ l of MTT (12 mM) (Invitrogen Thermo Fisher Scientific, California, USA) dissolved in PBS (Gibco™, Glasgow, UK). Formazan salt crystals were dissolved with 200  $\mu$ l of SDS (provided by the kit). Absorbance (OD) was measured at 540 nm using an UV-spectrometer (SpectraMax i3x, California, USA).

## 2.24 Statistical analysis

Data are expressed as means  $\pm$  SEM. A GraphPad InStat version 3.00 (GraphPad Software) was used to analyse the data. One-way analysis of variance with the with Dunnett (parametric data), Kruskal-Wallis Test (nonparametric data), Kruskal-Wallis Test (nonparametric ANOVA) with Dunn's Multiple Comparisons post-hoc test and A one-way ANOVA with Tukey- Kramer post-test (compare all pairs of columns) were used to test for statistical significance of differences between more than two experimental groups. Statistical significance was recorded at  $P < 0.05$ .  $N = 3$ , representative of independent experiments.

# Chapter 3

## Synthesis and characterisation of PLGA-SCD19 nanoparticles

---

### 3.1 Introduction

There are various methods that can be used to synthesize nanoparticles [173]. Possible approaches to making nanomaterials include top-down (e.g., media milling, wet milling, and high-pressure homogenisation) and bottom-up (e.g., solvent evaporation, spray drying, and nano-precipitation) [174, 175]. Top-down approaches include starting with a material which is in the macro/micro scale and using chemical/physical methods to reduce its dimensions until the nano-scale is obtained [176]. On the other hand, bottom-up methods are biology inspired which involves assembling or building up the small units (atomic/molecular) by using the interactions between molecules or colloidal particles (Figure 3.1) [177]. As a bottom-up approach, single emulsion-solvent evaporation (oil/water) is one of the most widely used methods to synthesise PLGA nanoparticles and a commonly accepted technique for encapsulating hydrophobic therapeutic agents [144, 178, 179]. Therefore, we used this technique to encapsulate SCD19, our novel MIF inhibitor, as a therapeutic candidate. The single emulsion-solvent evaporation method consists of two steps. Step one; the polymer and drug are dissolved in a volatile organic solvent (e.g., dichloromethane and acetone), this provides the polymer-drug organic solution (oil phase), then the water is added to form the oil-in-water emulsion (o/w). As the final part of step one, an ultrasonication or homogenisation is used to disperse physically the mixture, making it a uniform emulsion and form of “nano-drops”. Step two; the organic solvent is evaporated by stirring at room temperature and finally the polymer which now carry the drug are collected ultracentrifugation and washed with water to remove the excess of stabiliser and unencapsulated drug [180].

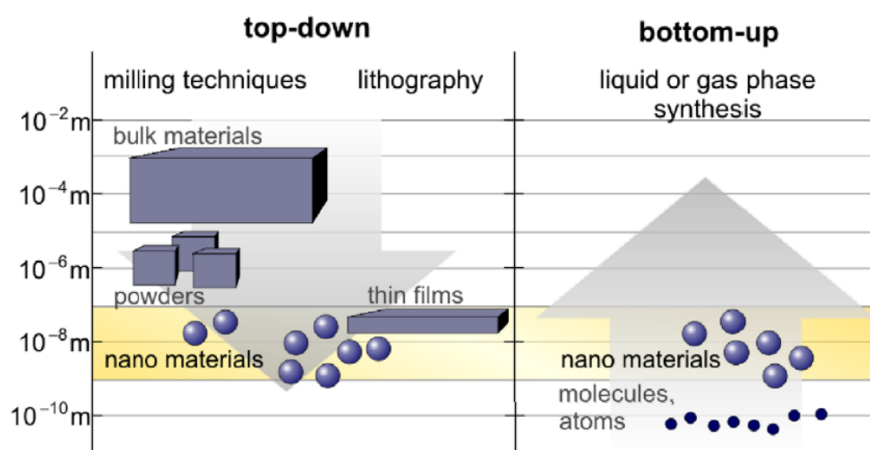


**Figure 3.1.** Methods of nanoparticle production. Top-down and bottom-up methods for nanoparticles preparation [181].

The importance of synthesising nanoparticles without any bacterial endotoxin contamination has been highlighted in many studies, since contamination of nanoparticles by LPS is not uncommon [182, 183]. Endotoxin, also known as lipopolysaccharides (LPS), is a large molecule (molecular weight 200–1000 kDa) that can be found on the outer membrane of Gram-negative bacteria. Contamination by LPS can lead to inappropriate immune/inflammatory effects [183, 184]. The contamination can occur during the synthesis procedure or via contaminated water and buffers [185]. The Limulus Amoebocyte Lysate (LAL) assay is the most frequently used endotoxin detection method that can be applied to examine the LPS contamination of prepared nanoparticles. This assay can detect and quantify LPS contamination at the picogram level (assay sensitivity 0.005 - 50 EU/ml (each 1 EU/ml is 0.1-0.2 ng/ml)) [186].

Synthesised nanoparticles need to be characterised to understand their physical and chemical features and properties. Characterisation of nanoparticles, in fact, is one of the most crucial steps when developing a nanodrug delivery system. This mostly includes, size, shape, surface charge, stability, toxicity, biocompatibility, drug loading capacity and drug release profile. In this study, the developed nanoparticles were designed for pulmonary administration targeting end-organ MIF activity. Therefore, defining the

physicochemical properties of PLGA-SCD19 nanoparticles particularly as pertains to their physical stability and interaction with cells and biological fluids from the lung was of the utmost importance. Size, shape, and morphology of the prepared nanoparticles can be investigated by using scanning electron microscope (SEM). In addition, transmission electron microscopy (TEM) is frequently applied to obtain the size distribution of the nanoparticles [187]. To investigate the hydrodynamic radius of nanoparticles in aquatic environments the standard techniques are nanoparticle tracking analysis (NTA) and dynamic light scattering (DLS). The latter method is also able to determine the surface charge of particles and poly dispersity index (PDI) or “dispersity” as recommended by IUPAC, which defines the degrees of non-uniformity of a size distribution of particles [188]. Both NTA and DLS techniques are based on recording and tracking the Brownian motion of nanoparticles in solution in 2 dimensions. The measurement of average distance moved by each particle in the  $x$  and  $y$  direction enable the particle diffusion coefficient ( $Dt$ ) be identified. As the three important factors, temperature ( $T$ ), solvent viscosity ( $\eta$ ), and temperature are known or introduced at the time of performing the experiment, the sphere-equivalent hydrodynamic diameter of the nanoparticles can be determined using the Stokes-Einstein equation [189]:

$$Dt = TK \frac{TKB}{3\pi\eta d}$$

Investigating the colloidal stability of nanoparticles in biological fluids provides essential information about their ability to resist sedimentation and particle aggregation. The colloidal stability can also influence bioavailability, long-term systemic circulation, and crossing biological barriers [190]. In this study we aimed to use PLGA-SCD19 nanoparticles for pulmonary delivery. Therefore, the nanoparticles were examined for physical stability of PLGA-SCD19 nanoparticles incubated with two synthetic simulated fluids, artificial lung fluid and artificial lysosomal lung fluid. The goal of this experiment was to shed light

on the size distribution and polydispersity index (PDI) of nanoparticles in the artificial fluids.

PLGA nanoparticles are approved by the US Food and Drug Administration (FDA) and European Medicine Agency (EMA) for various drug delivery systems in humans due to high biodegradability and biocompatibility [191], There are numerous techniques to assess the cytotoxicity of nanoparticles, including lactate dehydrogenase (LDH) assay, microculture tetrazolium assay, and trypan blue exclusion assay. LDH assay is one of the most widely accepted methods to assess the toxicity of nanoparticles. LDH is a cytoplasmic enzyme which use as an indicator of lytic cell death since it is released into the extracellular space following cellular membrane damage resulting from apoptosis or necrosis [192]. To investigate the toxicity of PLGA-SCD19 nanoparticles we measured the LDH release from different cell lines exposed to different concentrations of the nanoparticles for various time points. Additionally, to examine the biosafety and biocompatibility of nanoparticles a high content analyser method was used. High content screening (HCS) is a combination of high-resolution fluorescence-based imaging and cell-based assays that produces a visualisation tool and a comprehensive set of quantitative data, providing guidance on the toxic response of cells. This technique provides combined screening and analysis platform that can screen the impact of novel developed nanofomulation on the cell morphology [193].

One of the most interesting features of nanodrug delivery systems is their ability to efficiently cross biological barriers and assess different tissues followed by an efficient cellular uptake, based on their submicron dimensions [194]. Iron oxide magnetic nanoparticles (MNPs) play an increasingly important role in nanomedicine as contrast agents in biomedical imaging and theragnostic agents, where therapeutics with diagnostics are combined [195]. To evaluate the internalisation of PLGA-SCD19 nanoparticles in lung epithelial cells, we took advantage of iron oxide nanoparticles (MNPs) as a non-invasive tool for visualisation of cellular uptake. To this aim, PLGA-MNP-SCD19 nanoparticles

were synthesised by packaging both SCD19 and MNPs in PLGA nanoparticles and three different methods (Prussian blue, ferrozine-based colorimetric assay, and confocal microscopy) were applied to qualify and quantify intracellular PLGA-MNP-SCD19 content after exposure of *in vitro* human lung epithelial cell lines.

## 3.2 Results

### 3.2.1 LPS free nanoparticles

In this experiment, the concentration of endotoxin was evaluated by LAL assay. Two previous batches of nanoparticles which were found to be contaminated with LPS were also used as positive controls. The LPS concentration in the positive controls as assessed by LAL assay was almost 1 EU/ml, whereas in LPS free batches (nanoparticles without LPS contamination) the mean concentration for the whole batch of the nanoparticles without dilution was only 0.026 EU/ml (0.0026 ng/ml – 0.0052 ng/ml) and 0.009 EU/ml (0.009 ng/ml – 0.0018 ng/ml) for PLGA-MNP-SCD19 and PLGA-SCD19, respectively (Figure 3.1). It is worth mentioning that one endotoxin unit (EU) equals approximately 0.1 to 0.2 ng endotoxin/ml of solution [186].

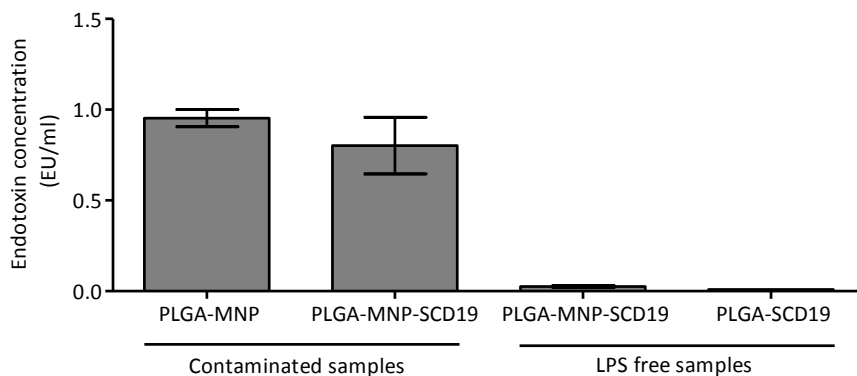


**Figure 3.1:** Endotoxin assay for nanoparticles. Endotoxin contamination in different batches of nanoparticles was evaluated by Limulus amoebocyte lysate (LAL) assay. Positive controls are previous batches of PLGA-MNP and PLGA-MNP-SCD19 nanoparticles which were confirmed to be contaminated with LPS. These samples were compared to LPS-free PLGA-MNP and PLGA-MNP-SCD19 nanoparticles (n=3). one EU equals approximately 0.1-0.2 ng endotoxin/ml [186].

### **3.2.2 Size and morphology of the nanoparticles**

Size and morphology characterization of nanoparticles is an important step to ensure the size range and sample uniformity of the produced nanoparticles. A scanning electron microscope (Zeiss NEON 40 EsB Cross Beam) was used to investigate the morphological characteristics of MNPs, PLGA-SCD19 and PLGA-MNP-SCD19. Although, significant aggregation was observed in uncoated-MNPs (Figure 3.2 A1 and A2), SEM images revealed that both PLGA-SCD19 (Figure 3.2 B1 and B2) and PLGA-MNP-SCD19 nanoparticles preparations (Figure 3.2 C1 and C2) possessed spherical shape and smooth morphology without any aggregation. A transmission electron microscope (JEOL 2100 LaB) was also employed to determine the size of nanoparticles. The average size determined from the TEM images was  $180 \pm 25$  nm and both PLGA-SCD19 and PLGA-MNP-SCD19 samples appear to be of identical size (Figure 3.2 B3 and C3).

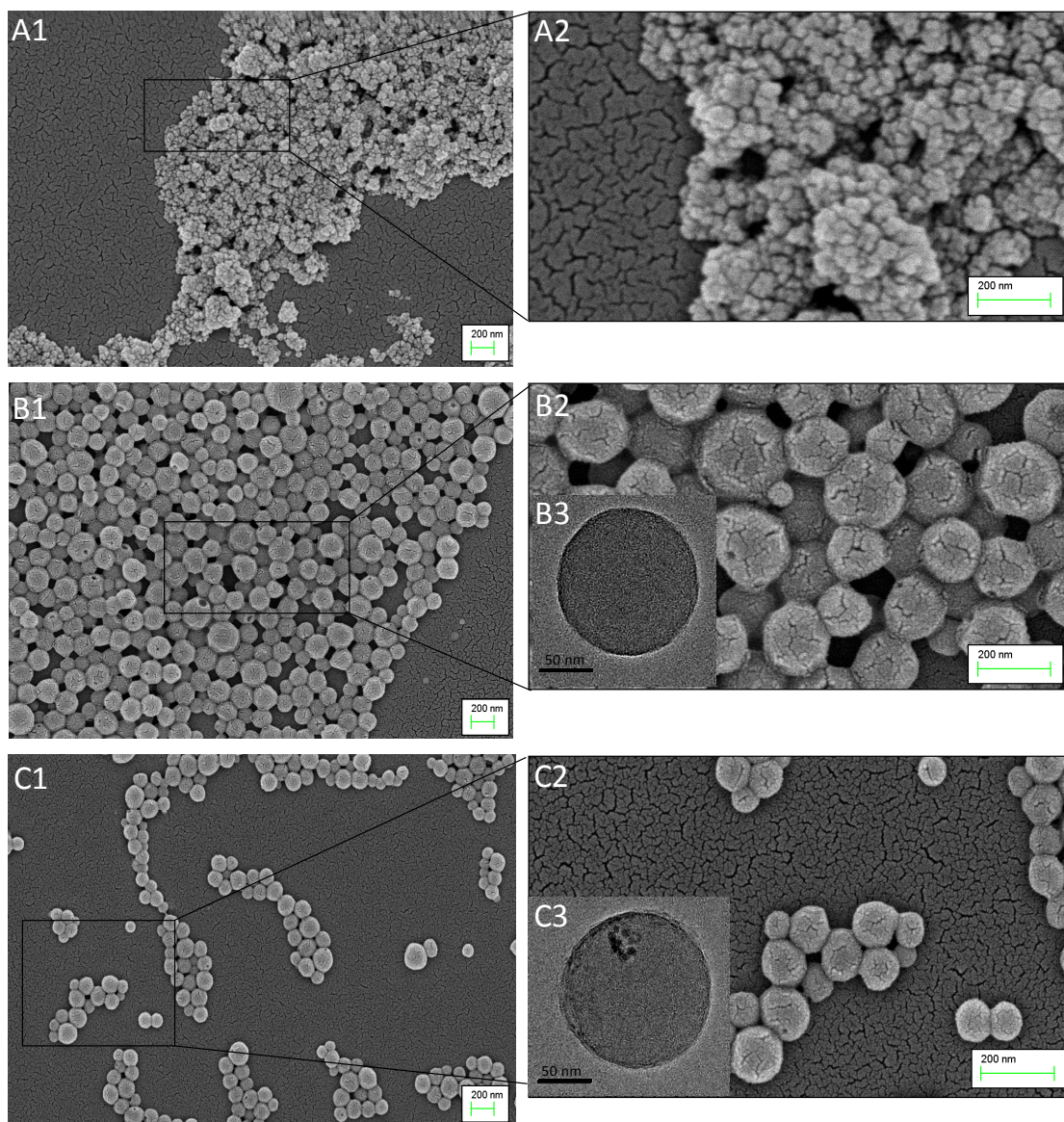


**Figure 3.2:** Electron microscopy images of the nanoparticles. Images of MNPs, PLGA-SCD19, and PLGA-MNP-SCD19 were obtained by scanning electron microscopy (SEM) and transmission electron microscopy (TEM). A1 and A2: SEM images of MNPs. B1 and B2: SEM images of PLGA-SCD19 nanoparticles. B3: TEM images of PLGA-SCD19. C1 and C2: SEM images of PLGA-MNP-SCD19 nanoparticles. C3: TEM images of PLGA-MNP-SCD19 in which the encapsulated MNPs can be seen in PLGA nanoparticles (higher dark contrast). Scale bars correspond to 200 nm.

### 3.2.3 Nano tracking analysis (NTA)

The measurement of hydrodynamic radius of the nanoparticles and their size distribution was carried out by NTA using the Malvern NS500 microfluidic

device (Malvern Instruments Ltd.) equipped with a 50 mW 532 nm laser. Despite a wide size range and aggregation in uncoated-MNPs (Figure 3.3 A), which has been already shown in SEM images, the single and sharp peaks of PLGA-SCD19 and PLGA-MNP-SCD19 (Figure 3.3 B and C) confirm that the nanoparticles had a uniform size distribution without any aggregation which was in accordance with the PDIs as determined by DLS (Table 3.1). The average hydrodynamic size of the samples as measured by using NTA were within the nanometric range and for both PLGA-SCD19 and PLGA-MNP-SCD19 nanoparticles was found approximately of the same size; PLGA-MNP-SCD19 ( $225 \pm 25$  nm) and PLGA-SCD19 ( $200 \pm 20$  nm).

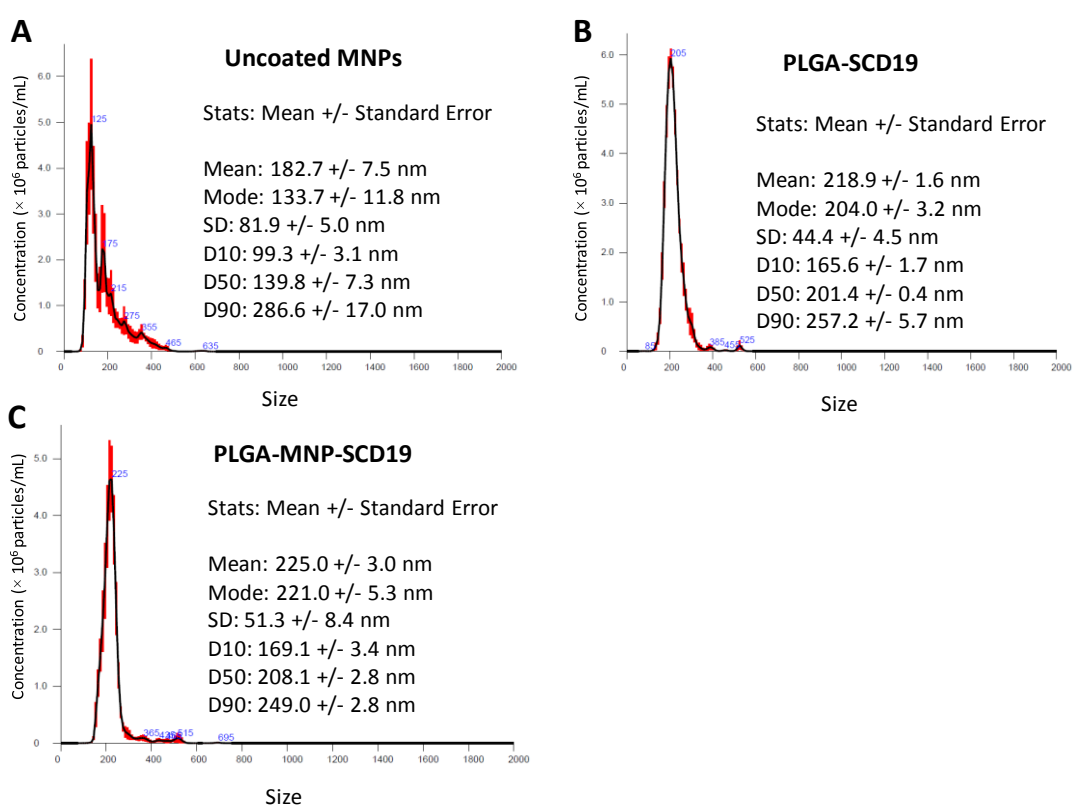


**Figure 3.3:** Size distribution of MNPs, PLGA-MNP, and PLGA-MNP-SCD19 nanoparticles using nanoparticle tracking analysis (NTA). A) Size distribution of MNPs. B) Size distribution of PLGA-SCD19. C) Size distribution of PLGA-MNP-SCD19. In the graphs, Mean is a calculated value which shows the average of the size distribution. The mode represents the peak of the frequency distribution. D10, D50, and D90 demonstrate D values in which the intercepts for 10%, 50% and 90% of the cumulative mass. Red line in each graph represents the standard deviation. All the information was calculated by the NTA software (NTA version 3.1.).

### 3.2.4 Surface charge, drug loading efficiency, drug content, and yield efficiency

A methodology developed by Malvern Instruments (Zetasizer Nano ZS90 instrument) was used to assess the Zeta-potential of PLGA-SCD19 which was our final product. The surface charge of nanoparticles as determined by DLS was  $-28.2 \pm 5.45$  mV which is graphically shown in Figure 3.4.

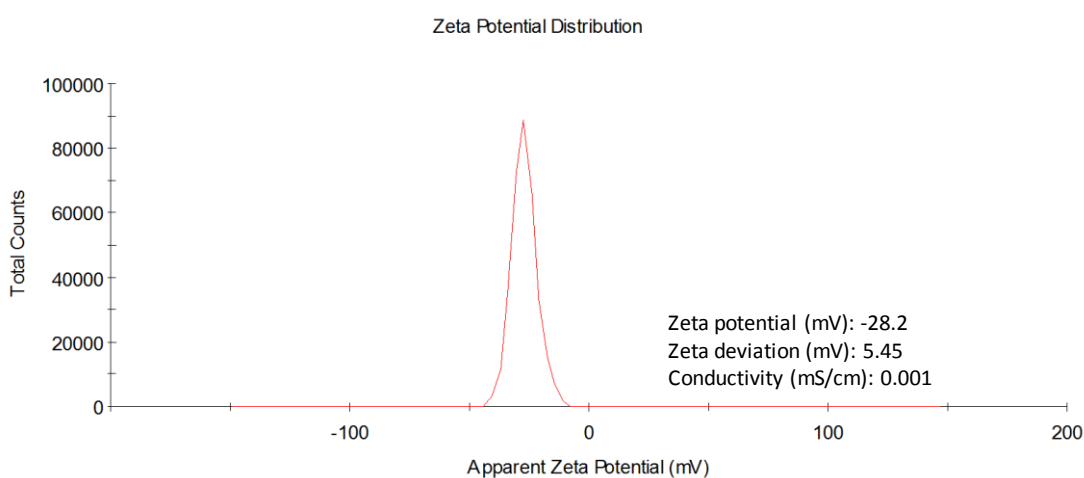


**Figure 3.4:** Zeta potentials of PLGA-SCD19 nanoparticles. A dynamic light scattering technique (DLS) was used to measure the zeta-potential of the nanoparticles.

The analysis of six batches of PLGA-SCD19 nanoparticles showed the concentration of SCD19 that encapsulated into the PLGA was  $3.7 \pm 0.7$  mg or  $15 \pm 0.1$  mM per batch, indicating that the loading efficiency was  $63 \pm 13$  %. Also, the optimised formulation presented satisfactory yield efficiency ( $66 \pm 4\%$ ), which is the weight of the raw materials (PLGA and SCD19) used in the preparation and the final weight of the produced PLGA-SCD19 nanoparticles. The amount of SCD19 which is available for release in the drug delivery system, known as drug content, was also  $5.7 \pm 0.1$  %. All the information is shown in table 3.1.

**Table 3.1:** Characteristics of PLGA-SCD19 nanoparticles. PDI= polydispersity index. DE= Drug loading efficiency. DC= Drug content. YE= Yield Efficiency. The data were obtained from six batches of PLGA-SCD19 nanoparticles.

	Diameter (nm)	Hydrodynamic diameter (nm)	PDI	DE (%)	DC (%)	YE (%)	Mass of SCD19 in the NPs (mg)	Concentration of SCD19 in the NPs (mM/batch)
<b>PLGA-SCD19</b>	180 ±25 nm	200 ±20 nm	0.066	63 ±13	5.7 ±1	66 ±4	3.7 ±0.7	15 ±0.1

### 3.2.5 Effect of lung artificial fluids on PLGA-SCD19 nanoparticles

The stability of PLGA-SCD19 nanoparticles in saline (control), artificial lung fluid, and artificial lysosomal fluid was evaluated after 48 h incubation at 37°C to simulate *in-vivo* nebulisation characteristics. Size and polydispersity index (PDI) of the nanoparticles were determined by using a DLS technique. Nanoparticles were significantly larger when incubated in artificial lung fluid compared to those incubated in saline ( $p < 0.01$ ), however this size change was not statically significant ( $P > 0.05$ ). No significant change in average NP size was detected for those incubated with the artificial lysosomal fluid. The average size of PLGA-SCD19 nanoparticles after incubation for 48 h in saline, artificial lung fluid, and artificial lysosomal fluid was  $234 \pm 10.4$  nm,  $271 \pm 22.8$  nm, and  $215 \pm 21.9$  nm, respectively (Figure 3.5).

In comparison to control, PLGA-SCD19 incubated with saline, the value of PDI for nanoparticles incubated in both artificial lung fluid and artificial lysosomal fluid was increased, but it was not statistically significant ( $P > 0.05$ ) (Figure 3.5). The average of PDI as determined by DLS for the nanoparticles incubated with saline, artificial lung fluid, and artificial lysosomal fluid was  $0.07 \pm 0.05$ ,  $0.18 \pm 0.1$ , and  $0.16 \pm 0.14$ , respectively (Figure 3.6). Although, the average PDI was increased in nanoparticles incubated with the artificial lung fluids, results obtained are in an acceptable size range which indicate that the nanoparticles remained stable and monodisperse in lung fluids.

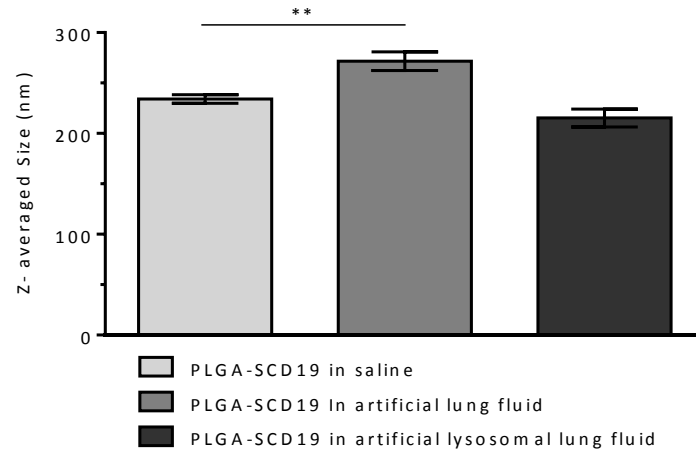


**Figure 3.5:** Impact of artificial lung fluids on the size of PLGA-SCD19 nanoparticles. The PLGA-SCD19 nanoparticles were dispersed in three different solutions (artificial lung fluid, artificial lysosomal fluid, and saline (control) (0.9% (v/v)), after 48 h incubation at 37 °C a dynamic light scattering technique (DLS) was used to measure the size of nanoparticles. Data are presented as mean  $\pm$  SEM and is expressed in Z-average size (nm). A One-way Analysis of Variance (ANOVA) with Dunnett (compare all vs. control) test was used to test for statistical significance of differences between control (PLGA-SCD19 in saline) and the testes (PLGA-SCD19 in artificial lung fluid and PLGA-SCD19 in artificial lysosomal fluid). \*\* $p < 0.01$ , PLGA-SCD19 in saline versus PLGA-SCD19 in artificial lung fluids. The experiment was performed for three batches of PLGA-SCD19 nanoparticles.

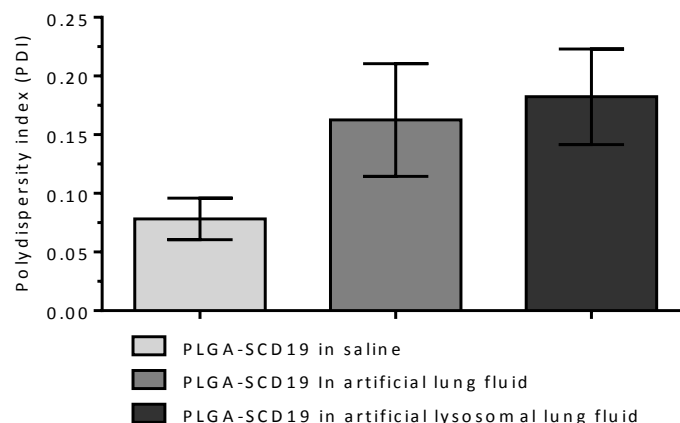


**Figure 3.6:** Effect of artificial lung fluids on the polydispersity index (PDI) of PLGA-SCD19 nanoparticles (NPs). The PLGA-SCD19 NPs were dispersed in three different solutions (artificial lung fluid, artificial lysosomal fluid, and saline (control) (0.9% (v/v)) after 48 h incubation at 37 °C a dynamic light scattering technique (DLS) was used to measure the PDI of nanoparticles. A Kruskal-Wallis Test (nonparametric ANOVA) analysis was run to test for statistical significance of differences between control (PLGA-SCD19 in saline) and the testes (PLGA-SCD19 in artificial lung fluid and PLGA-SCD19 in artificial lysosomal fluid). No significant difference was found between the control (PLGA-SCD19 in saline) and tests (PLGA-SCD19 in artificial lung fluid, artificial lysosomal fluid) ( $p=0.15$ ). The experiment was performed for three batches of PLGA-SCD19 nanoparticles.

### 3.2.6 Drug releases profile

An *in vitro* cumulative drug release study was performed to investigate the rate at which the loaded drug (SCD19) is released into the environment. The experiment was conducted over three days for three batches of PLGA-SCD19 nanoparticles. Figure 3.7 illustrates the drug release profile, with rapid drug release over the first 24 hours followed by a plateau.

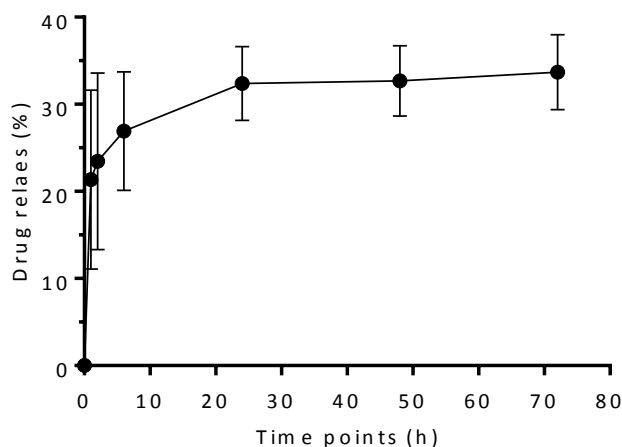


**Figure 3.7.** Drug releases profile from PLGA-SCD19 nanoparticles. The nanoparticles were dispersed in saline (0.9% (v/v), then a dialysis method was used to investigate the drug releases of PLGA-SCD19 nanoparticles. Cumulative release profile was measured over three days for three batches of PLGA-SCD19 nanoparticles. Data are presented as mean  $\pm$  SEM.

### 3.2.7 Biocompatibility

To investigate the biological safety of PLGA-SCD19 and PLGA-MNP-SCD19 nanoparticles we examined the morphology of A549 cells exposed to cadmium selenide quantum dots (CdSe QD) (positive control), MNP, PLGA, PLGA-SCD19, and PLGA-MNP-SCD19 nanoparticles (100  $\mu\text{g}/\text{ml}$  each) for 24 h by high-content screening (HCS). The cell morphology parameters, including cell area and nuclear area of the cells exposed to PLGA-SCD19 and PLGA-MNP-SCD19 were within the normal variation range and there were no signs of cellular or nuclear deformities, membrane bound vesicles, or cell rupture. Compared to the control (untreated cells) no significant changes was observed in both cell and nuclear area. The experiment was performed for three batches of nanoparticles. The results are visualised and quantified in Figure 3.8 A and B. In contrast, a dramatic abnormality and deformity was observed in the cells incubated with CdSe QD, which is a toxic substance and used as positive control.

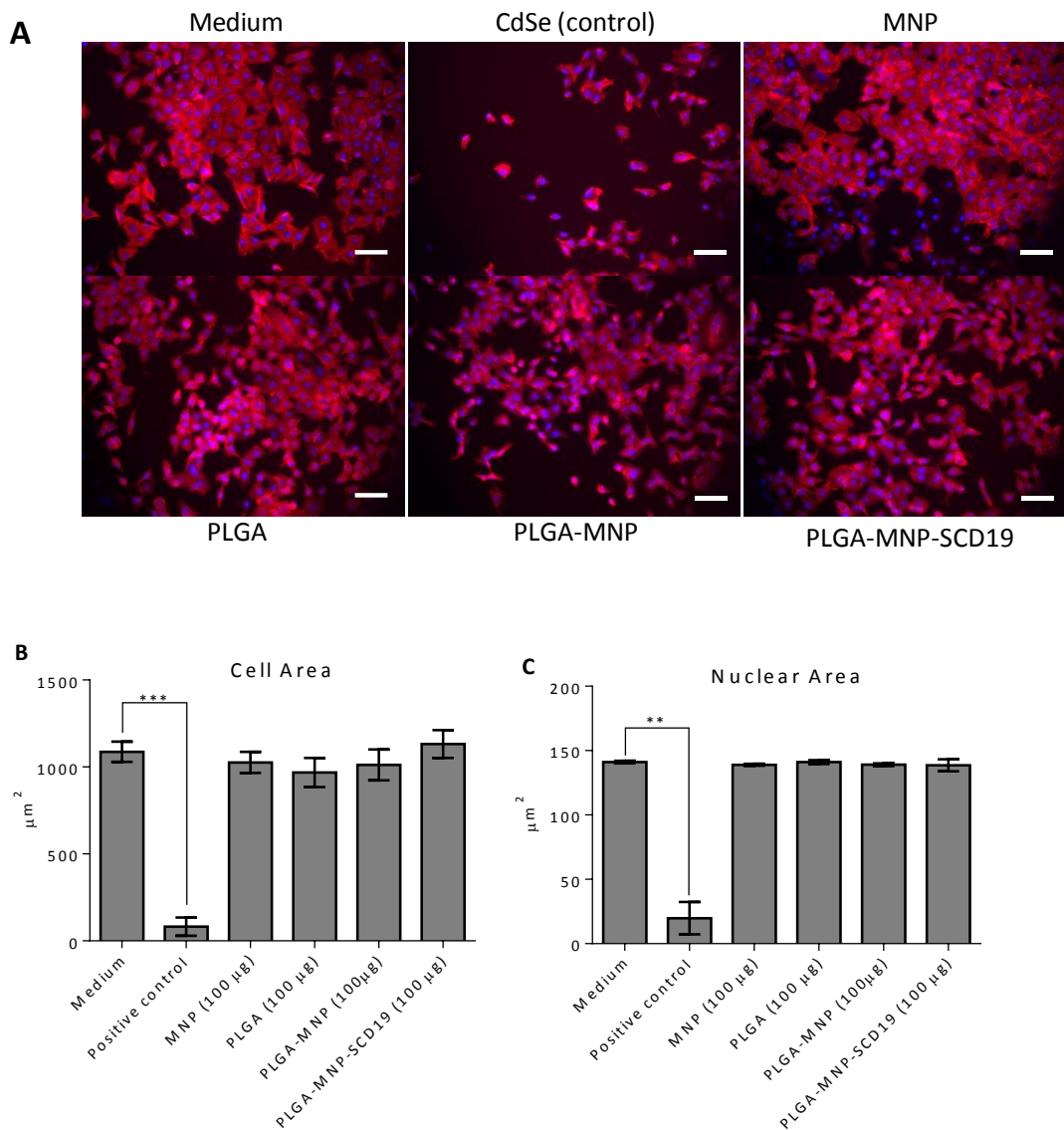


**Figure 3.8:** Cytocompatibility analysis of different nanoparticles in A549 cells. A) The morphology of A549 cells exposed to nanoparticles (100 µg/ml) for 24h was examined by a cell-based automated microscope after staining the cells by Hoechst 33342 and Rhodamine phalloidin to stain nuclei (blue) and actin filaments (red), respectively. B and C) Morphological analysis of A549 cells treated by the nanoparticles was performed using IN Cell Analyzer-1000 equipped with Investigator software by quantifying cell and nuclei area. Positive control= Cadmium selenide quantum dots (CdSe QD). Negative control= untreated cells. Scale bar 10 µm. Data are presented as mean ± SEM and is expressed in micrometre (µm). A Kruskal-Wallis Test (nonparametric ANOVA) with Dunn's Multiple Comparisons post-hoc test was used to test for statistical significance of differences. \*\*\*P<0.001, Medium (negative control) versus treated cells with CdSe QD (positive control) in cell area assessment; \*\*P<0.05, Medium (negative control) versus treated cells with CdSe QD (positive control) in nuclear area assessment.

### **3.2.8 Toxicity**

A standard technique, LDH assay, was performed to assess the toxicity of PLGA-SCD19 nanoparticles for three different cell lines (A549 cells, LLC cells, and Raw 264.7 cells). The cells were exposed to a serial dilution of PLGA-SCD19 nanoparticles for two different time points (24h and 48 h). No significant cytotoxicity was observed at concentrations of 1 mM or less. The results are graphically shown in Figure 3.9. At 2 mM concentrations at a 48-hour timepoint significant cytotoxicity of 18% was observed. For other cell types assessed cytotoxicity at this timepoint was < 10%.

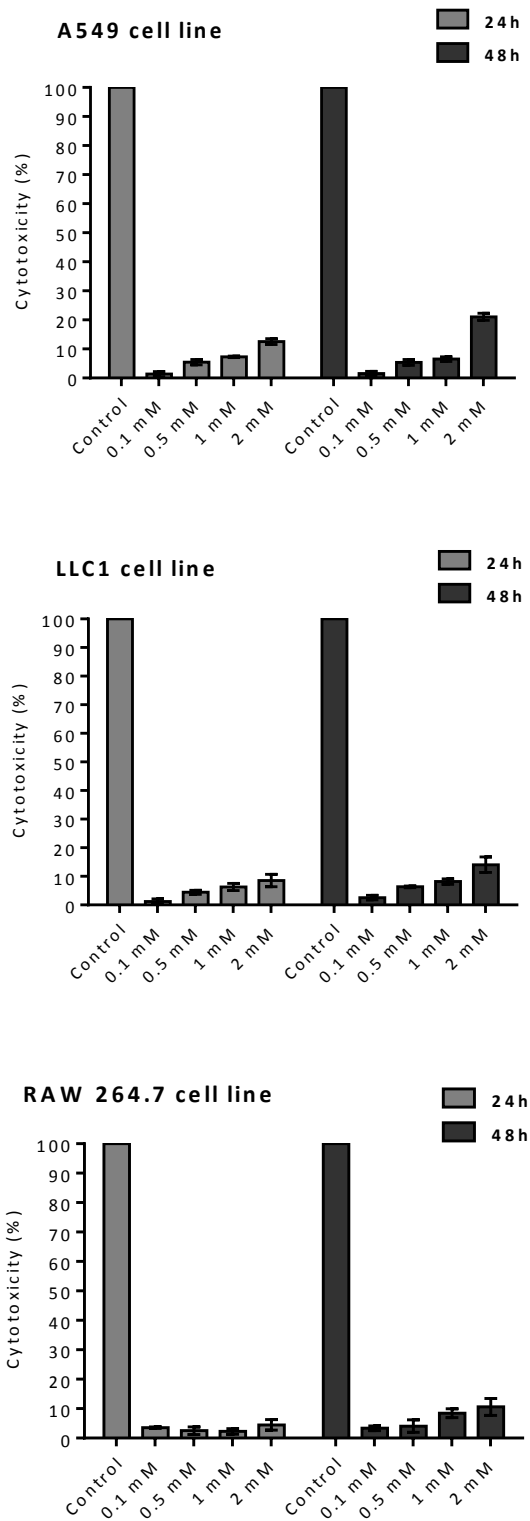


**Figure 3.9:** Assessment of different concentrations of PLGA-SCD19 nanoparticles-induced cytotoxicity in three different cell lines. The cells lines (A549, LLC, and Raw 264.7) were incubated with four different concentrations of the NPs carrying (0.1 mM, 0.5 mM, 1 mM, and 2 mM SCD19) for 24h and 48h. LDH activity is expressed as a percentage of a fully lysed cell control. Data are presented as mean  $\pm$  SEM. n=3.

### 3.2.9 Internalisation of NPs in alveolar epithelial cells

Iron oxide or magnetic nanoparticles (MNPs) were applied as an imaging agent to detect the cellular uptake of nanoparticles, due to their high refractive index. After packaging both MNPs and SCD19 in PLGA, the A549 cells were incubated with PLGA-MNP-SCD19 (100  $\mu\text{g}/\text{ml}$ ) and MNPs as positive control (100  $\mu\text{g}/\text{ml}$ ) for 24 h. After washing the cells to remove nanoparticles from the media and staining the cells by Hoechst 33342 and Rhodamine phalloidin fluorescent dyes, internalisation of nanoparticles was examined by a laser scanning confocal microscopy. As can be seen in figure 3.10 (the merged pictures), significant uptake of the nanoparticles was observed after 24 hours. There were no notable differences between uncoated MNPs (control) and PLGA-MNP-SCD19 in terms of cellular uptake and internalisation. After cellular uptake, no detectable cellular deformation or cell necrosis was observed.

Parallel assays to assess cellular uptake PLGA-MNP-SCD19 nanoparticles were undertaken, including Prussian blue and ferrozine-based colorimetric assay. The A549 cells were incubated with three different concentrations of PLGA-MNP-SCD19 nanoparticles (50, 100, 200  $\mu\text{g}/\text{ml}$ ) at 24h and 48 h timepoints. Then the MNPs were stained with Prussian blue and visualised by a bright field microscope. The nanoparticles, as we observed, accumulated only in cytoplasm close to nuclei and did not penetrate into the nuclei after both 24 h and 48 h incubation timepoints (Figure 3.11 A & B). To determine the intracellular nanoparticles content, ferrozine assay technique was performed. As represented graphically in Figure 3.12, the internalisation of the nanoparticles demonstrated a linear correlation with the NP concentration. However, no significant differences in the cellular uptake were found between the same concentration in both incubation time points (Figure 3.12).

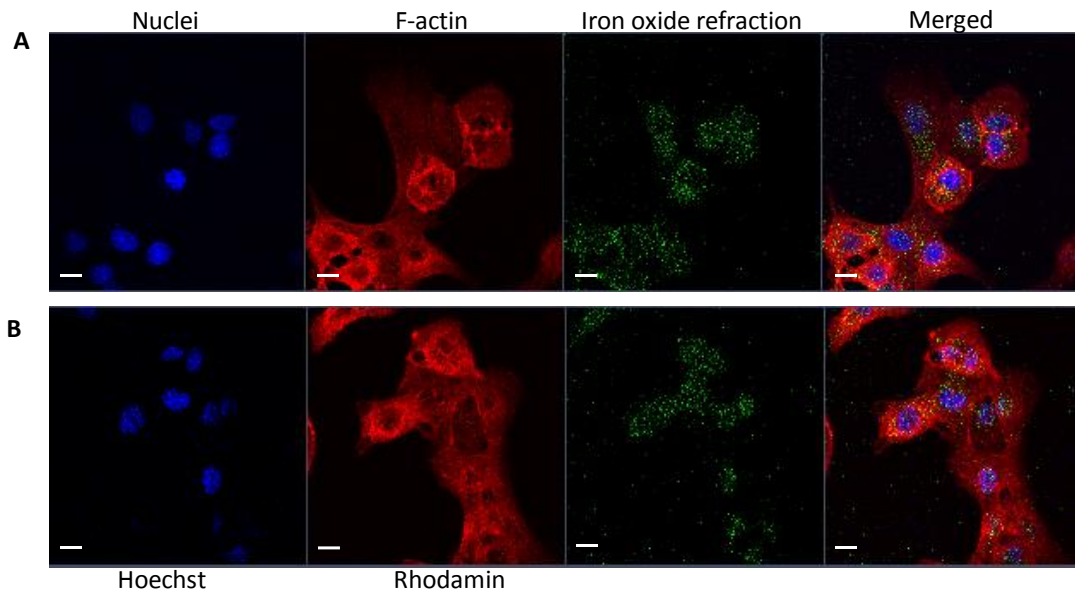


**Figure 3.10:** Internalisation of PLGA-MNP-SCD19 nanoparticles by A549 cells. Uptake of the nanoparticles can be visualised in A549 cells by detecting the reflectance signal of MNPs (iron oxide nanoparticles) (green). A ZEISS 510 Meta confocal microscope was used to detect the reflection of MNPs. The confocal images were acquired after cell exposure to NPs for 24 h. The cells were stained with Hoechst 33342 and Rhodamine phalloidin to stain nuclei (blue) and actin filaments (red), respectively. A) The A549 cells exposed to PLGA-MNP-SCD19 (100 µg/ml). B) The positive control was only treated by uncoated MNPs (100 µg/ml). Scale bar 10 µm.

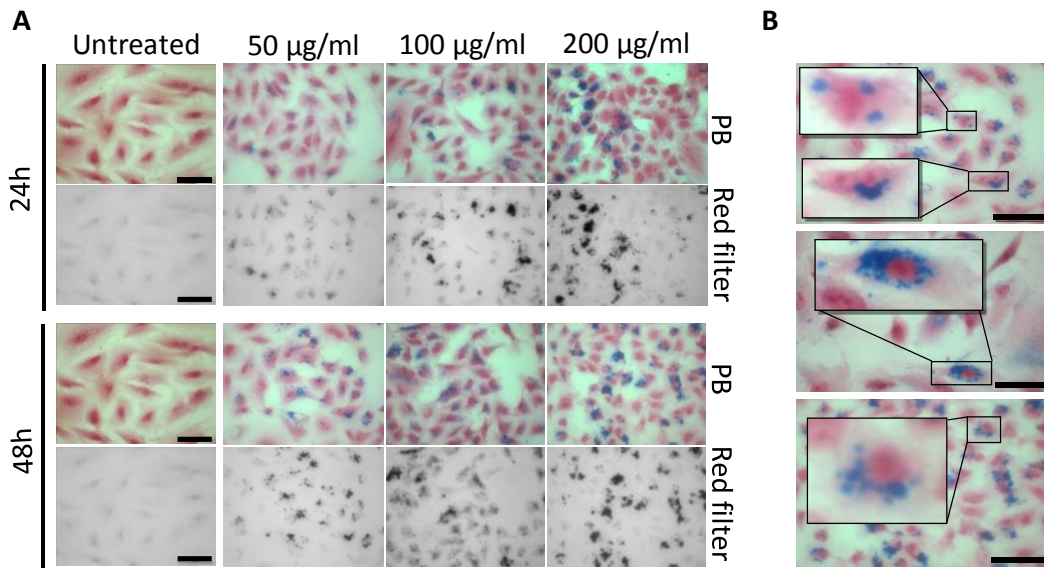


**Figure 3.11:** Cellular uptake of PLGA-MNP-SCD19 by A549 cells. A) Cells incubated with three different concentrations of the PLGA-MNP-SCD19 nanoparticles (50, 100, 200 µg/ml) at two time points (24h and 48h). The cells were stained with Perls' Prussian blue (MNPs) and Neutral Red (0.5% (v/v)) to stain nuclei and cytoplasm. The Images were acquired using a 10x objective lens from a Nikon epifluorescent microscope with colour camera. Coloured filters were applied to aid visualisation of NPs only (red filter) (lower of each panel). B) The A549 cells exposed to 100 µg/ml PLGA-MNP-SCD19 nanoparticles for 24 h. Microscopy image of the NPs captured using a 40x objective lens. Scale bar 10 µm.

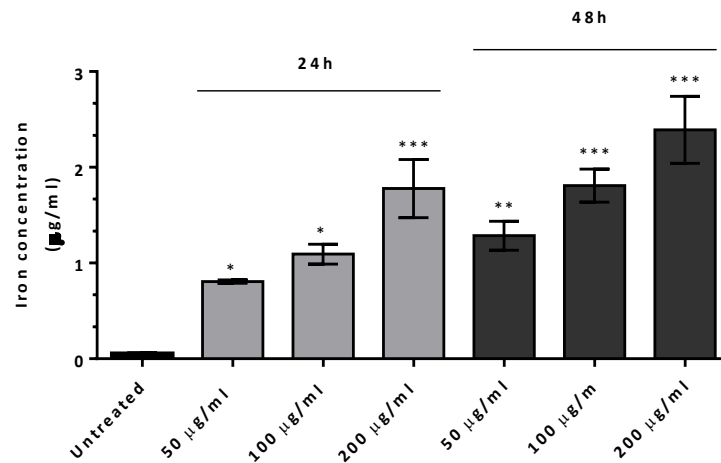


**Figure 3.12:** Intracellular iron content quantification by ferrozine assay. The results on the graph are presented as weight of Intracellular iron/well, after 24h and 48h of incubation The A549 cells with PLGA-MNP-SCD19 nanoparticles (50, 100, 200 µg/ml). Data are presented as mean ± SEM and is expressed in microgram per millilitre (µg/ml). A One-way Analysis of Variance (ANOVA) with Dunnett (compare all vs. control (untreated)) was used to test for statistical significance. Quantitative analysis demonstrated degree of MNP association compared to untreated sample. n=3.

### 3.3 Discussion

Nanotechnology is being actively developed in medicine [114], with a particular focus on the use of nanoparticles as a drug delivery system [113]. PLGA is among the most frequently used polymeric nanoparticles for drug delivery, which has been approved by the FDA and EMA due to its special properties, including biodegradability, biocompatibility, low toxicity, and minimum side effect [144, 196]. Emulsion-solvent evaporation (oil/water) method is the most commonly used method to prepare PLGA loaded drug nanocarriers [144, 178].

It has been reported that the best drug-to-polymer mass ratio to achieve maximum drug loading efficiency and enhance drug release profile is 1:10 [197-199], hence we utilized PLGA (100 mg) and SCD19 (10 mg) to prepare PLGA-SCD19 nanoparticles. The nanoformulation presented satisfactory yield ( $66\% \pm 4$ ) and drug loading efficiency ( $63\% \pm 13$ ). The drug content ( $5.7\% \pm 0.1$ ) was above-average of the drug content efficiency which is usually achieved in nondrug delivery systems (maximum 10%) [200]. To examine cellular internalization of nanoparticles, we synthesised a thermostatic system in which MNPs (imaging reagent) and SCD19 (drug candidate) were encapsulated in PLGA nanoparticle. Utilizing the TEM, SEM, NTA, and DLS techniques in this study, we measured the particle size distribution, hydrodynamic radius, zeta potential, and polydispersity index (PDI) of the synthesised nanoparticles and investigated the stability of the nanoparticles in artificial lung fluids at 37 °C. The average size estimated for both PLGA-SCD19 and PLGA-MNP-SCD19 from the TEM and SEM images was  $180 \pm 25$  nm which was smaller than the size obtained from the nano tracking analysis (NTA). This difference might be attributed to hydrodynamic swelling of particles in aquatic environment that causes particles to be larger [201]. We observed that both PLGA-SCD19 and PLGA-MNP-SCD19 nanoparticles in aqueous solution remained monodispersed without any aggregation with an associated modest increase in size of  $225 \pm 25$  nm compared to  $200 \pm 20$  nm, respectively. These

findings were in accordance with previous published work where PLGA nanoparticles synthesised by the oil/water technique resulted in a hydrodynamic radius of the range 100 to 250 nm [202, 203]. In the artificial lung fluid, the size of PLGA-SCD19 nanoparticles increased slightly at 24 hours but had decreased at 48 hours which could possibly be explained by degradation. It was also observed that the poly dispersity index (PDI) of the PLGA-SCD19 nanoparticles after two days incubation in both artificial lung fluid and artificial lung lysosomal fluid was greater than the nanoparticles incubated with saline (control). The PDI value for all samples incubated in lung synthetic fluids were less than 0.2, showing an acceptable monodisperse size distribution and indicating that the nanoparticles are stable under physiological conditions. Recent studies have suggested that PDI values smaller than 0.3 are desired to ensure monodisperse PLGA nanoformulations [204, 205]. Zeta-potential indicates the surface charge of nanoparticles, which is an important factor for prediction of colloidal stability and estimation of the nanoparticle's electrostatic interactions. The zeta potential from PLGA-SCD19 nanoparticles as determined by using DLS was  $-26 \pm 5.4$  mV, showing the stability of the nanoparticles as the zeta potential values greater than +25 mV or less than -25 mV are demonstrative of stabilised particles [206].

The size of nanodrug carriers can effect drug release and cellular internalisation, two important features of nanoparticles [207]. Larger sized particles present slower release rates because of smaller surface area to volume ratio compare to smaller sized nanodrug carriers [208]. In the present study, *In vitro* drug release behaviour of PLGA-SCD19 nanoparticles showed a high initial burst release (30% drug release) for first 24 h, which is possibly due to the percentage of drug that is over or just under the surface of the nanoparticles, followed by a plateau release for two days. It has previously been shown that the degradation of PLGA nanodrug carriers, characteristically is rapid in the initial stage (approximately 30% in the first 24 h) and subsequently plateau's, resulting in an extended and sustained drug release profile [144, 209].

Providing Endotoxin (LPS) free nanodrug delivery system is a crucial issue that must be taken into careful consideration in the field of nanosafety [182]. LPS binds to a soluble LPS-binding protein, which is recognised by Toll-like receptor (TLR4). TLR4, together with MD2 and CD14 provides the signal-transducing molecule of the LPS receptor complex [210], allowing rapid response to endotoxin-containing bacteria, which promotes the activation of innate immune responses and an upregulation of pro-inflammatory cytokines (e.g., TNF- $\alpha$  and IL-6), leading to systemic sepsis and enhanced morbidity and mortality in the clinical arena [211, 212]. Therefore, endotoxin contamination interferes in both *in vitro* and *in vivo* experiments [183].

It should be pointed out the endotoxin limit for medical devices is set at < 0.5 EU/ml for products that directly or indirectly contact the cardiovascular system and lymphatic system, for devices within the spinal cord and in contact with cerebrospinal fluid (CSF) the accepted level is < 0.06 EU/ml. The LPS concentration of PLGA-SCD19 nanoparticles used in work presented in this thesis as measured by LAL assay was 0.009 EU/ml. Consequently, the final LPS concentration that cells are exposed to will be sub-picogram level which satisfies current FDA regulations [213].

To evaluate the cytotoxicity of PLGA-SCD19 nanoparticles, LDH release assays were performed on our selected cell lines which included the human lung adenocarcinomic cells line - A549, the mouse lung carcinoma cell line - LLC, and the murine macrophage cell line - RAW 264.7. It was found that PLGA-SCD19 NP at concentration < 1mM assessed on selected cell lines was non-toxic. At higher concentrations particularly treated A549 cells – cytotoxicity up to 18% was observed.

High content screening (HCS), which is an automated microscopy and image analysis for high-throughput screening, was employed to determine the changes in cell morphology of epithelial lung cells after incubating the cells with the nanoparticles. Recent studies have demonstrated the suitability of this

technique in monitoring and screening the cytotoxic effect of nanoformulations [214, 215]. In this study, HCS data showed that both PLGA-SCD19 and PLGA-MNP-SCD19 were completely safe, since no change in cell and nuclei area was observed compared to untreated cells. A cell undergoing apoptosis shows a series of typical morphological features in which the cytoskeletal protein actin plays a critical role. We investigated any changes in the cytoskeletal protein actin in A549 cells exposed to nanoparticles. After 24 h incubation, no statistically significant differences were observed in the cytoskeletal protein actin of the treated cells compared to untreated control cells. Chemical-induced apoptosis exhibits characteristic nuclear morphological changes that are distinct from healthy and apoptotic cells [216, 217]. In comparison to untreated cells, the obtained quantified data from the HCS analyser has shown no changes in the nuclei area of the treated cells. Whereas, In the positive control in which the cells were exposed to CdSe QD (toxic compound) both cell area and nuclei area were decreased dramatically.

The use of iron oxide nanoparticles (MNPs) has become a widespread strategy for visualization of the cellular uptake of nanoparticles, owing to their biocompatibility and high refractive index contrast [218-220]. In the current study, we used MNPs to investigate the internalisation of the nanoparticles by encapsulating MNPs in PLGA nanoparticles. Then, the quantitative and qualitative cellular uptake of the nanoparticles was evaluated by performing reflectance confocal microscopy, Prussian blue, ferrozine-based colorimetric assay. The results of the reflectance confocal microscopy revealed significant uptake of our PLGA-MNP-SCD19 by lung epithelial cells after 24 h incubation. However, we found no detectable differences between uncoated MNP (control) and PLGA-MNP-SCD19 in terms of internalisation and localisation. This can be explained by the significant aggregation of uncoated MNPs which was demonstrated on TEM and NTA analysis. The obtained images of Prussian blue staining showed that nanoparticles accumulated only in cytoplasm and no nanoparticles localisation in cell nucleus was observed. In our study, ferrozine

assay revealed that the uptake of nanoparticles in A549 cells reaches a saturation point at 24 h, because no significant changes were detected between 24 h and 48 h timepoint incubation. This result strongly agrees with previous reports. In particular, as recently revealed, [221] the internalisation of PLGA based drug carriers in alveolar epithelial cells increased from 2 to 24 h, and then plateaued.

# Chapter 4

## Characterisation of aerosolised PLGA- SCD19 nanoparticles

---

## 4.1 Introduction

Pulmonary administration of nanotherapeutics for the treatment of respiratory diseases has attracted great interest in recent decades due to the numerous advantages of this promising route of administration [222-224]. Local pulmonary delivery provides on the one hand, higher drug concentrations with a rapid onset of action, combined with less systemic toxicity. This then reduces the dose required and improves overall patient adherence [161]. Moreover, targeting the lung has added advantages such as minimum extra- and intracellular enzymatic activity, significant surface area for absorption efficiency while avoiding first-pass metabolism [225]. The use of aerosolised PLGA-drug nanoparticles for local and systemic drug delivery has increased markedly over the last ten years, due to its high biosafety, drug bioavailability, and low immunogenicity [226].

Aerosol nanodrug delivery to the lungs can combine the advantages of both inhalation therapy and nanodrug delivery methods, providing an effective treatment for lung diseases [166, 226]. In the current study we investigated and characterised the properties of PLGA-SCD19 nanoparticles after nebulisation by Aerogen Ltd nebulisers which incorporate its unique vibrating mesh technology. This unique method (i.e. vibrating mesh) has substantially improved the development of inhalation devices, allowing enhanced doses of active compound to be delivered to the patient while reduced risk of adverse effects, including barotrauma and volutrauma compared to conventional nebulisers [227]. Aerogen nebulisers are based on a technology which is known as AerogenVibronic, a palladium vibrating mesh just 5mm in diameter with 1,000 holes that vibrates at 128,000 times per second, creating a “mini pump” that produces fine particle uniform size droplets, to produce the ideal particle size for deep lung deposition [228]. Initially we examined the quality of PLGA-SCD19 nanoparticles after nebulisation by the Aerogen vibrating mesh nebuliser. The nanoparticles were dispersed in 0.9% (w/v) saline which is referred to as

“physiological saline” [229]. Numerous medications are dissolved or dispersed in physiological saline, because of its benefits such as aiding pulmonary secretions and avoiding hyperosmosis compare to H<sub>2</sub>O [230]. We compared the nebulisation time, delivered volume, and the mass of delivered drug by the Aerogen nebuliser from the nanoparticles dispersed in either 0.9% (w/v) saline and H<sub>2</sub>O. To meet appropriate aerosolisation criteria, aerosolised nanoparticles should be characterised in terms of several key biophysical properties, such as mass median aerodynamic diameter (MMAD), Geometric standard deviation (GSD), volume median diameter (VMD), fine particle fraction (FPF), nebulisation efficiency, and regional aerosol deposition [167, 231]. According to European and US guidelines, aerodynamic particle size distribution (APSD) is a key factor when developing an inhalable therapeutic product [232, 233]. We used a Next Generation Impactor (NGI), a multi-stage cascade impactor, to determine the APSD of the aerosolised PLGA-SCD19 nanoparticles as well as the MMAD, which is defined as the median of the particle-size distribution with having regard to the aerodynamic diameter. NGI is consider as one of the gold standard methods for inhaler test [234], due to its high-performance, accuracy and easy to operate features. The cascade impactor has seven stages and the aerosolised particles are deposited on removable collection cups that are held in a tray. The system is calibrated within the flow rate range of 30–100 L min<sup>-1</sup> which can classify aerosolised nanoparticles based on their aerodynamic diameter, according to the cut-off diameter on each collection stage from 14.1 μm to 0.98 μm, it also has a micro-orifice collector (MOC) that collects extra-fine particles (≤0.7 μm) so each stage captures aerosolised particles in a defined range of aerodynamic particle sizes (see Figure 4.1) [235, 236].

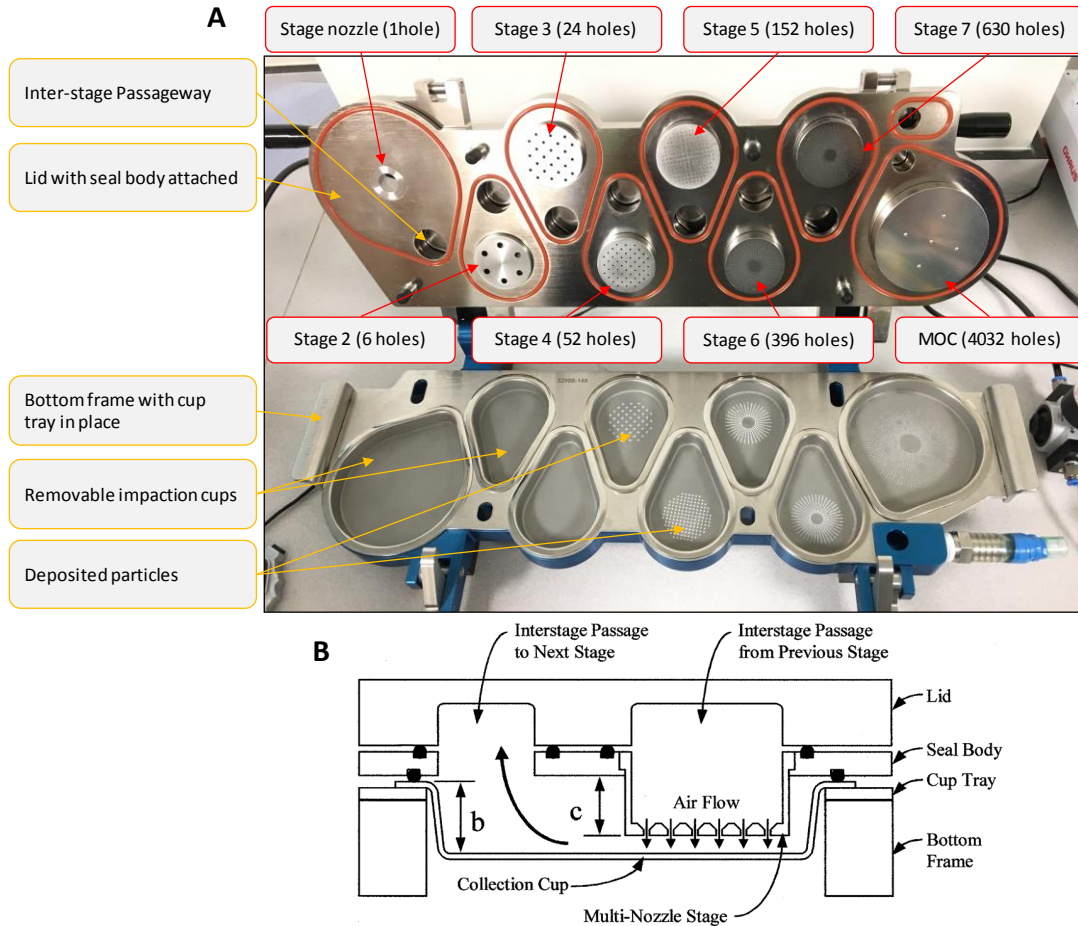


**Figure 4.1:** Next Generation Impactor System (NGI). A) Assembled view and nozzle configuration of the NGI. B) Layout of inter-stage passageways to measure the aerosol droplet size from a nebulizer [237].

NGI has been successfully employed to investigate the properties of aerosolised PLGA drug carriers in several previous studies [238-240]. It has been shown that the ideal aerosol particle size distribution for deep lung deposition in alveolar region, is between 1-5  $\mu\text{m}$ . The aerosol particle sizes range from 5-8  $\mu\text{m}$  are preferentially deposited in the airway, whereas mouth and throat deposition are found with particles > 8  $\mu\text{m}$ . Particles smaller than 1  $\mu\text{m}$  are preferentially exhaled (see Figure 4.2) [241].

We also employed laser diffraction analysis for further characterisation of aerodynamic properties of the aerosolised PLGA-SCD19 nanoparticles to achieve a transfer from dispersed nanoparticles to aerosolised nanoparticles for

inhalation to the lower respiratory tract. Laser diffraction is a common method used for estimating several key features of aerosolised nanotherapeutics, including fine particle fraction (FPF) which is referred to as the fraction that lies below 5  $\mu\text{m}$  in size and have a high chance of delivering into the deep lung and GSD that implicates the variability of the particle size distribution of nebulised aerosols [242]. The laser diffraction method is based on determining the angular difference in intensity of light scattered collecting the scattered light using a detector array as a laser beam passes through aerosol particle sample [243]. The angle of the diffraction (scattering angle) can be measured by the detector to evaluate the size of the nanoparticle, since large particles scatter laser light at small angles compare to small particles [244, 245].

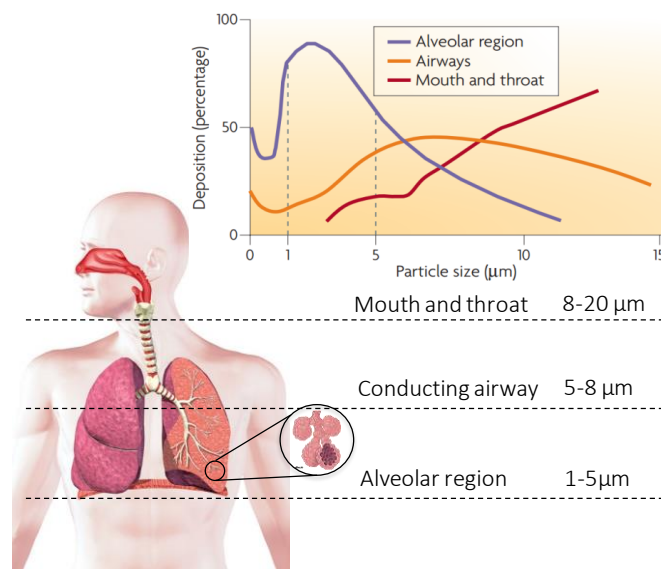


**Figure 4.2:** The relation of particle size distribution and the deposition of aerosol particles in the human respiratory tract [241].

To investigate the *in vitro* nebulisation efficiency of our aerosolised nanopackage inhibitors generated with a vibrating mesh nebuliser, experiments were conducted with two types of breathing simulators – the first for unassisted spontaneous breathing and the second for assisted spontaneous ventilation. Breathing simulators are designed to reproduce a wide range of breathing

profiles that mimic the human inhalation airflow profile and are now a key part of routine oral inhaled product (OIP) testing [246].

Unassisted spontaneous breathing patterns were simulated using a digitally controlled breathing simulator (ASL5000, IngMar Medical). The breathing simulator has three main sections; piston, actuator and control unit. The piston that is driven by the actuator provides a rectilinear motion which simulates lungs inhaling and exhaling, according to the equation of motion. The ASL5000 allows the creation of various types of breaths and simulates the spontaneously breathing patient in a variety of modes and patterns such as; coughs, apnea, snoring, active exhalation [247], however for this current study only a normal breath-simulation tidal pattern was conducted. We also used a mechanical ventilation (also known as assisted ventilation) for *In vitro* and experimental studies of aerosolised PLGA-SCD19 nanoparticles to assess aerosol lung deposition. Mechanical ventilations have been used in intensive care unit (ICU) since 1940s [248]. It has been shown that the use of mechanical ventilations to deliver aerosolised medications via vibrating mesh nebulisers provides a high efficiency dose delivery of aerosol therapeutic agents to the lungs ([NCT01879488](#)) [249]. Recently, In a clinical studies ([NCT02298101](#)) the ability of the vibrating mesh nebulisers was investigated via a mechanical ventilation to ensure the high efficiency dose delivery of aerosol medications to the lung, resulting in high superiority of the nebulisers to deliver nebulised therapeutics into the pulmonary system as compared to other nebulisers [250].

## 4.2 Results

### 4.2.1 Optimisation of PLGA-SCD19 nanoparticles for the nebuliser

To determine the appropriate concentration of PLGA-SCD19 nanoparticles for use with the Aerogen nebulisers, 1 ml of three different concentrations (8, 16, 40 mg/ml) of PLGA-SCD19 nanoparticles dispersed either in 0.9% (w/v) saline and H<sub>2</sub>O was nebulised and collected in the falcon tubes. Then we assessed and compared the collected volume, required time for nebulisation and mass of delivered SCD19 for the all different concentrations.

The volume of the nebulised samples dispersed either in 0.9% (w/v) saline and H<sub>2</sub>O was measured and compared to blank samples (H<sub>2</sub>O and 0.9% (w/v) saline) which were used as control. No detectable change was observed as the concentration of the nanoparticles was increased from 8 mg/ml to 40 mg/ml. Although, no solution remained in the medication cup after nebulisation the volume delivery efficiency for the majority of samples was in excess of 85% and no change was found between low and high sample concentration in terms of collected volume (see Figure 4.3).

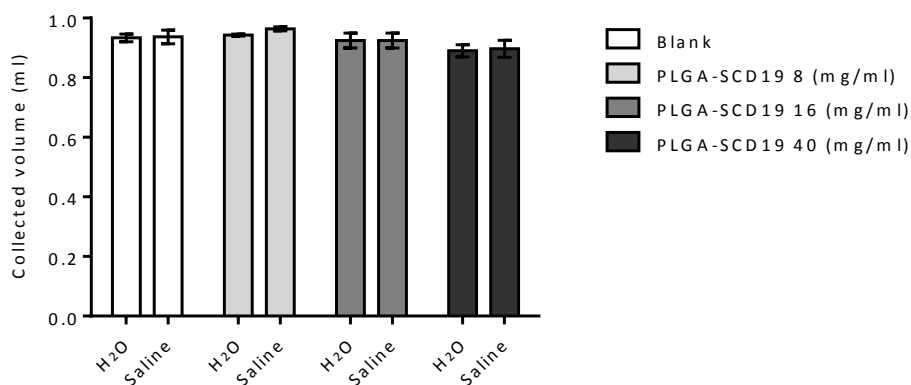


**Figure 4.3:** The volume delivery efficiency of Aerogen nebuliser for PLGA-SCD19 nanoparticles. Different concentrations (8, 16, 40 mg/ml) of PLGA-SCD19 dispersed in either H<sub>2</sub>O or saline were nebulised by an Aerogen Solo vibrating mesh nebuliser. The samples (1ml) were nebulised and the collected volume was measured by a micropipette. The efficiency of the volume delivery is expressed as the millilitre sample collected after nebulisation. Data is presented as mean  $\pm$  SEM and is expressed in microgram per millilitre ( $\mu$ g/ml) (n= 3). Blank= saline or H<sub>2</sub>O as the vehicle control). A One-way Analysis of Variance (ANOVA) with Dunnett (compare all vs. control (blank) and samples dispersed in H<sub>2</sub>O vs. samples dispersed in saline) was used to test for statistical significance. There was no statistically significant difference.

The time required to nebulise 1 ml of two different nanoformulation concentrations (8 mg/ml and 16 mg/ml) was comparable to that observed for blank samples (H<sub>2</sub>O and 0.9% (w/v) saline). However, the nebulisation time was increased for the high concentration (40 mg/ml) of PLGA-SCD19 nanoparticles dispersed in both H<sub>2</sub>O and 0.9% (w/v) saline. It is important to mention that a clogging issue on the vibrating mesh from the high concentration sample (40 mg/ml) was observed after each run (see Figure 4.4) and extra washing procedures were required to clean the vibrating mesh. Due to this clogging issue, the time required to nebulise 40 mg/ml was notably higher than controls (see Figure 4.5).

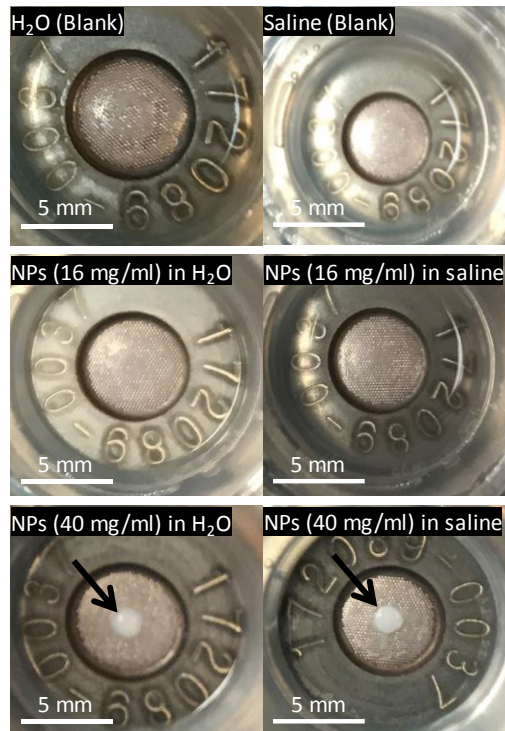


**Figure 4.4:** Photographs of the vibrating mesh of the nebuliser before use (top two panels) and after nebulisation on of the 16 mg/ml and 40 mg/ml of PLGA-SCD119 nanoparticles (NPs) in either H<sub>2</sub>O or saline. black arrows show the nanoparticles clogging on the vibration mesh. Scale bar 5 mm.

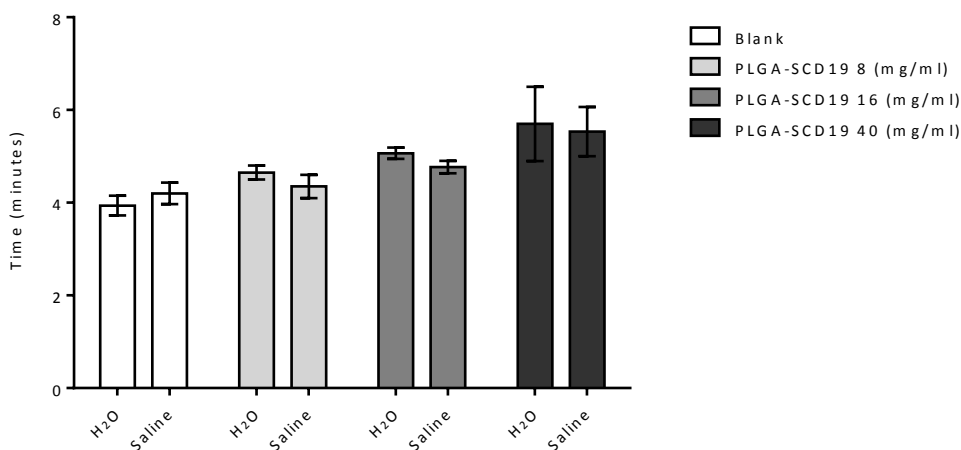


**Figure 4.5:** Nebulisation times of Aerogen nebuliser for PLGA-SCD19 nanoparticles. Different concentrations (8, 16, 40 mg/ml) of PLGA-SCD19 nanoparticles dispersed in either H<sub>2</sub>O or saline were nebulised by an Aerogen Solo vibrating mesh nebuliser. The samples (1ml) were nebulised and the nebulisation time for sample delivery was measured by a lab timer recorder. The nebulisation time is expressed as the minutes needed to deliver 1ml of each concentration. Data is presented as mean  $\pm$  SEM and is expressed in microgram per millilitre ( $\mu$ g/ml) (n= 3). Blank= saline or H<sub>2</sub>O as the vehicle control. A One-way Analysis of Variance (ANOVA) with Dunnett (compare all vs. control (blank) and samples dispersed in H<sub>2</sub>O vs. samples dispersed in saline) was used to test for statistical significance. There was no statistically significant difference.

The concentration of PLGA-SCD19 nanoparticles (mass of SCD19) before and after nebulisation was compared to assess the nebuliser drug delivery efficiency. The maximum delivery efficiency, almost 100%, of nanoformulation delivery was found for the 8 mg/ml and 14 mg/ml samples which is shown graphically in Figure 4.6. The samples with highest concentration (40 mg/ml), dispersed in either H<sub>2</sub>O and 0.9% (w/v) saline, resulted in approximately 80% delivery efficiency which was the lowest level among all the concentrations.

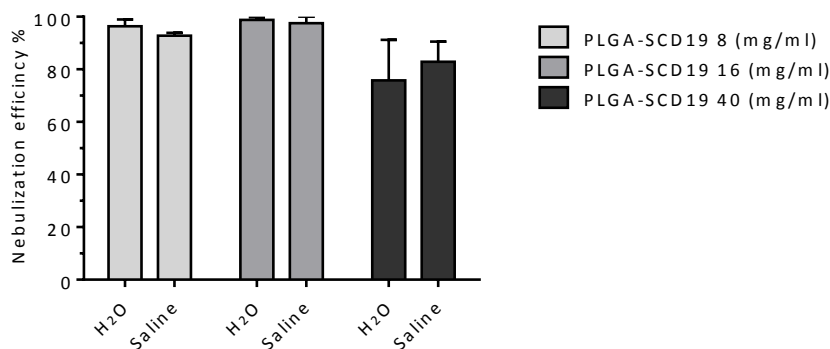


**Figure 4.6:** The efficiency of Aerogen nebuliser to deliver PLGA-SCD19 nanoparticles. Different concentrations (8, 16, 40 mg/ml) of PLGA-SCD19 nanoparticles dispersed in either H<sub>2</sub>O or saline were nebulised by an Aerogen Solo vibrating mesh nebuliser. The samples (1ml) were nebulised and the nebuliser efficiency to deliver nanoparticles was analysed after comparing the concentration of SCD19 before and after nebulisation in the samples by a UV-Vis machine. Data is presented as mean  $\pm$  SEM and are expressed in microgram per millilitre ( $\mu\text{g/ml}$ ),  $n = 3$ , representative of 3 experiments. A One-way Analysis of Variance (ANOVA) with Dunnett (compare all vs. control (blank) and samples dispersed in H<sub>2</sub>O vs. samples dispersed in saline) was used to test for statistical significance. There was no statistically significant difference.

To examine the impact of the Aerogen nebuliser on the size and volume of PLGA-SCD19 nanoparticles dispersed in 0.9% (w/v) saline, following nebulisation, the nebulised nanoparticles were re-collected in falcon tube and both the particle size and volume of the nanoparticles, before and after nebulisation, were measured and compared by DLS. Figures 4.7 and 4.8 show the size and volume of PLGA-SCD19 nanoparticles for both pre- and post-nebulisation, respectively. The particle size and volume of the nanoparticles remained similar to the initial nanoformulation before nebulisation and the Aerogen vibrating mesh nebuliser had no detectable impact on the PLGA-SCD19 nanoparticles.

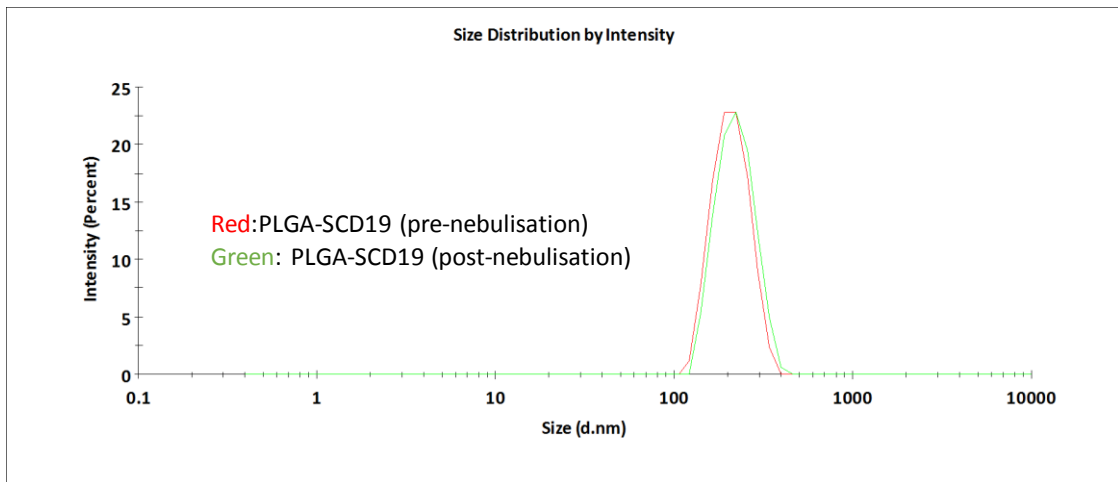


**Figure 4.7:** Effect of nebulisation in the size of PLGA-SCD19 nanoparticles. The size of PLGA-SCD19 nanoparticles were measured before and after nebulisation using DLS technique. An Aerogen Solo vibrating mesh nebuliser (Aerogen, Galway, Ireland) was used to generate the aerosolised PLGA-SCD19 nanoparticles. n=3.

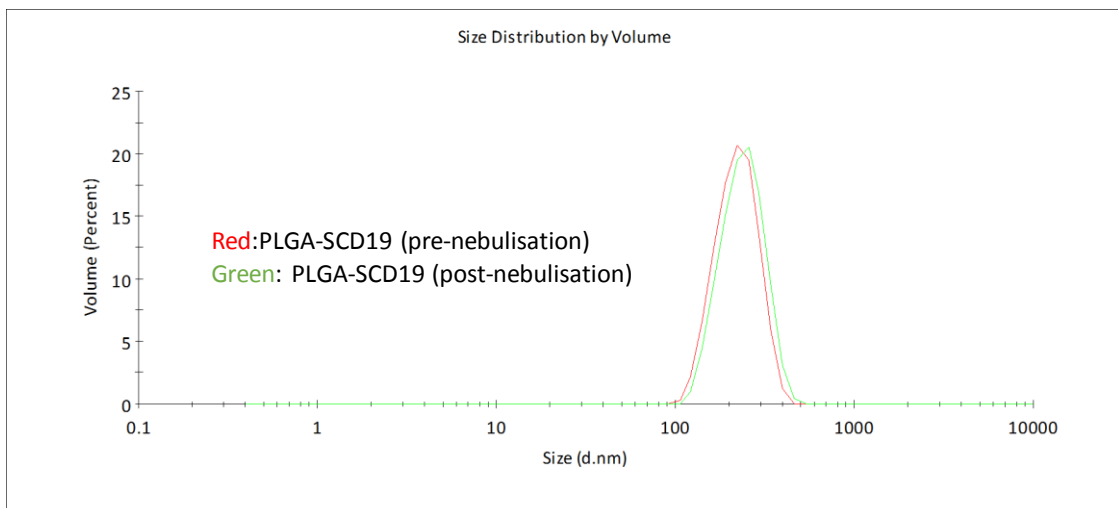


**Figure 4.8:** The impact of nebulisation on the volume of PLGA-SCD19 nanoparticles. The volume of PLGA-SCD19 nanoparticles were measured before and after nebulisation using DLS technique. An Aerogen Solo vibrating mesh nebuliser (Aerogen, Galway, Ireland) was used to generate the aerosolised PLGA-SCD19 nanoparticles. n=3

## 4.2.2 Reginal aerosol deposition in the Next Generation Impactor (NGI)

The mass median aerodynamic diameter (MMAD) of the nebulised PLGA-SCD19 nanoparticles as determined by a Next Generation Impactor (NGI) was  $2.2 \pm 0.4 \mu\text{m}$ . Also, Volume median diameter (VMD), geometric standard deviations (GSDs), and fine particle fraction (FPF) for the three runs are presented in Table 4.1. To determine the relative amount of deposition of the PLGA-SCD19 nanoparticles in the different regions of the lung. The aerosol was examined by the NGI. During the course of the experiment, the aerosolised nanoparticles were deposited on the different plates of the impactor based on their droplet size distribution, which is shown in Figure 4.9. Quantification of deposited nanoparticles in each plate showed that most of nanoparticles have deposited in the stages of 3, 4, 5, 6 and 7, indicating that the vast majority of the aerosolised PLGA-SCD19 nanoparticles had a droplet size range between approximately 1 to  $5 \mu\text{m}$ . The highest deposition rate was detected in the stages of 5 and 4, which had almost half of the deposited nanoformulation. Also, about 4% of the nanoparticles deposited in throat region and only 2% of the nanoformulation had the droplet size greater than  $14 \mu\text{m}$  (see Figure 4.10).

**Table 4.1:** Aerodynamic properties of the aerosolised PLGA-SCD19 nanoparticles with an Aerogen Solo vibrating mesh nebuliser. Results are representative of three independent nebulisations, as mean  $\pm$  SD, with 1 ml of saline solution analysed by laser diffraction technique. VMD= volume median diameter, GSD= geometric standard deviation, FPF= fine particle fraction.

<b>Mesh nebuliser</b>	Standard
<b>Power supply (output voltage)</b>	100%
<b>HOLDING chamber</b>	No
<b>VMD (<math>\mu\text{m}</math>)</b>	$4.4 \pm 0.33$
<b>GSD (<math>\mu\text{m}</math>)</b>	$1.5 \pm 0.2$
<b>FPF <math>5 \mu\text{m} &lt; 5 \mu\text{m}</math> (%)</b>	59.6 %
<b>FPF <math>2 \mu\text{m} &lt; 2 \mu\text{m}</math> (%)</b>	9.9 %
<b>Output (mL/min)</b>	$0.3 \pm 0.2$
<b>Duration (min)</b>	$3.3 \pm 0.2$

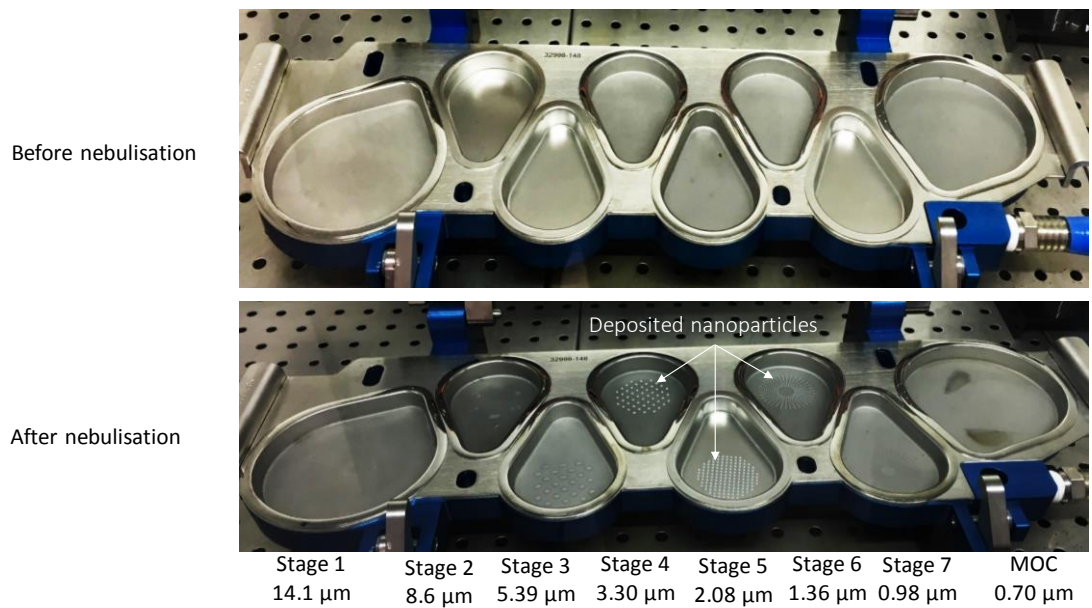


**Figure 4.9:** The Aerosol PLGA-SCD19 nanoparticles distribution at different Impactor stages. Upper panel, before running the experiment all the caps have been washed by BPS buffer to remove any possible contamination. In lower panel, an Aerogen Solo vibrating mesh nebuliser was used to nebulised PLGA-SCD19 nanoparticles into the cascade impactor (Next Generation Impactor, Model 170). The deposited PLGA-SCD19 nanoparticles, indicated by white arrows, was observed mostly in the stages of 3, 4, 5, 6, and 7 with the size distribution of 3.30  $\mu\text{m}$ , 2.08  $\mu\text{m}$ , and 1.36  $\mu\text{m}$  respectively.

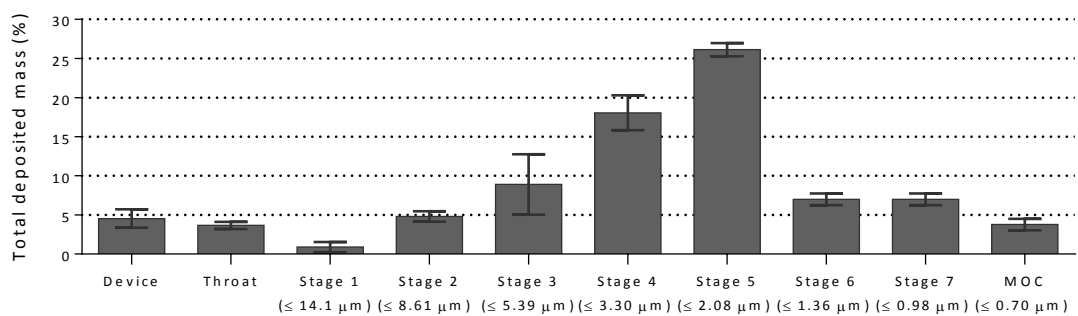


**Figure 4.10:** Quantification of the deposited PLGA-SCD19 nanoparticles. Distribution of droplet size after nebulisation using an Aerogen Solo vibrating mesh nebuliser in the different stages of cascade impactor (Next Generation Impactor, Model 170). The data is represented as mass percentage of nominal dose (n=3). The average of delivery time was 4:10 minutes. The Mass Median Aerodynamic Diameter (MMAD) obtained with PLGA-SCD19 nanoparticles was  $2.2 \pm 0.4 \mu\text{m}$ .

### 4.2.3 Drug delivery efficiency; mechanical ventilator & human breathing simulators

To assess the *in vitro* drug delivery efficiency three batches of PLGA-SCD19 nanoparticles were nebulised by a human mechanical ventilator and a human breathing simulator. The results of the experiments are summarised in Table 4.2 and Table 4.3. The delivery time for all the samples was in the standard range. Using a mechanical ventilator resulted in 23% drug delivery efficiency with the small standard deviation (0.88%). The normal respiration rate provided by the human breathing simulator brought 14.1% drug delivery and the standard deviation was the same as ventilation experiment.

**Table 4.2:** The mechanical ventilator measurements. A mechanical ventilator (SERVO-i®) was used to investigate the delivery efficiency for PLGA-SCD19 nanoparticles delivery. The experiment was conducted for three batches of PLGA-SCD19 (1 ml, 14 mg/ml). The mechanical ventilator was attached to a filter to collect inhaled dose. The delivered dose was determined by extraction of nanoparticles from the filter and subsequent quantification by using a UV-Vis spectrophotometer based on a standard curve that was generated by preparing a serial dilution of PLGA-SCD19 nanoparticles. The percentage found in the inhalation filter represents the delivery efficiency. Data are presented from a series of n = 3 experiments (Run 1,2 and 3).

	Loaded PLGA-SCD19 (mg/ml)	Dose duration (min)	Delivered NPs (mg/ml)	Mass balance (%)	Average (%)	STDEV (%)	Delivered SCD19 (mg/ml)
Run 1	14	4:18	3.37	24.07			
Run 2	14	4:02	3.17	22.64	23.04	0.88	0.17
Run 3	14	4:31	3.14	22.48			

**Table 4.3:** Breathing simulator measurements. A breathing simulator (ASL5000) was used to characterise the delivery efficiency of the breathing simulator for PLGA-SCD19 nanoparticles delivery. The delivery efficiency was investigated for three batches of PLGA-SCD19 (1 ml, 14 mg/ml). The breathing simulator was attached to a filter to collect inhaled dose. The delivery efficiency was determined by extraction of nanoparticles from the filter and subsequent quantification by using a UV-Vis spectrophotometer based on a standard curve that was generated by preparing a serial dilution of PLGA-SCD19 nanoparticles. The percentage found in the inhalation filter represents the delivery efficiency. Data are presented from a series of n = 3 experiments (Run 1,2 and 3).

	Loaded NPs (mg/ml)	Dose duration (min)	Delivered NPs (mg/ml)	Mass balance (%)	Average (%)	STDEV (%)	Delivered SCD19 (mg/ml)
Run1	14	3:44	1.92	13.76			
Run2	14	4:26	1.65	11.76	14.1	0.88	0.10
Run3	14	4:49	2.35	16.78			

#### 4.2.4 Discussion

Aerosol therapy is an effective technique to deliver medications, including nanotherapeutic agents to the respiratory tract. It has been previously shown that 75% of the nanotherapeutics administered via injection are dissipated systemically – with ultimately poor delivery to the lung for the treatment of lung specific diseases. This results in not only loss of treatment efficiency but also enhances the risk for systemic drug side-effects. In contrast, more than 80% of the drug payload can be delivered to the lung when using a nanotherapeutic inhaled strategy [251].

To optimise inhaled therapies several important factors including, physical characteristics of Inhaled pharmaceuticals (e.g. particle size distribution), devices and inhalation methods used need to be considered [252]. Nebulisers are among the most efficient devices that have been developed and employed for inhalation therapy [253]. All commercially available nebulisers are categorised into three types; (1) jet nebulisers, (2) ultrasonic nebulisers, and (3)

mesh nebulisers. Jet nebulisers have been used frequently for the treatment of respiratory diseases. However, several studies have highlighted potential disadvantages to this mode of therapeutic administration, including low drug delivery efficiency and the requirement for the use of compressed gas and additional tubing [254-256]. Ultrasonic nebulizers also have significant drawbacks as an optimum lung delivery system. These include inability to deliver viscous solutions and heat-sensitive therapeutic agents, due to the high temperature they generate during operation [257, 258]. In order to overcome these disadvantages significant work has been undertaken with the development of mesh nebulisers. Mesh nebulisers are practical, portable, quiet and small in size. They also have improved drug delivery efficiency and minimal residual volume (reservoir is ~0.3 ml) aligned with shorter treatment times (3-10 min). Their capacity to generate high concentration fine-particle fractions increases drug delivery to the lung peripheries [227, 256, 259, 260]. The analysis of both EU and US clinical trial databases has revealed that mesh nebulisers are now the most commonly used inhaled-delivery device compared to jet nebulisers for industry clinical trials[227].

Despite these advantages, these mesh-based systems are not without their drawbacks. One such issue is clogging of the pores when delivering viscous or highly concentrated drug formulations. In order to overcome this, it is necessary to investigate the effect of these factors on each respective mesh nebuliser [260]. In this study, nebulisation of PLGA-SCD19 nanoparticles (40 mg/ml) resulted in clogging of the nanoparticles on the vibrating mesh, increasing nebulisation time and decreasing drug delivery efficiency. However, lower concentration of PLGA-SCD19 (16 mg/ml) showed almost 100% delivery efficiency within 4 minutes to deliver 1 ml of the nanoformulation without any clogging issues. The analysis of post-nebulisation PLGA-SCD19 has shown that the size and volume of the nanoformulation were identical to the size and volume of the pre-nebulisation samples, indicating that the nebuliser has no adverse effect on the physical properties of the nanoparticles. Aerosol particle

size has been shown to play a vital role in evading the physiological barriers of the pulmonary system and targeting the therapeutics to the appropriate respiratory tract [261]. The volume median diameter (VMD) of the aerosolised PLGA-SCD19 nanoparticles was measured to be  $4.4 \pm 0.33 \mu\text{m}$  with a possible geometric standard deviation (GSD)  $1.5 \pm 0.2 \mu\text{m}$ . This midpoint droplet size is recognised as the ideal particle size distribution for deep lung deposition [241]. The fine particle fraction (FPF) of the aerosolised nanoformulation revealed that at least 60% of the particles are perfect size range with a mass median aerodynamic diameter (MMAD) of  $2.2 \pm 0.4 \mu\text{m}$ , predicting targeting and achieving deep deposition within the respiratory tract. Moreover, the results of the *in vitro* regional aerosol deposition measurement (cascade impactor) predict that in excess of 70% of the aerosolised PLGA-SCD19 will be deposited within the alveolar region.

Our results reveal that aerosolised PLGA-SCD19 nanoparticles deliver highly satisfactory *in vitro* delivery efficiency for both the mechanical ventilator and human breathing simulator. A recent review of nanoparticle aerosolised systems in clinical trials has shown that whole lung drug deposition via mechanical ventilators is 1% to 16% [262], whereas our work shows improved values of 23% and 14% drug deposition in our mechanical ventilator and human breathing simulator systems. We suggest that these improved values are secondary to a high degree of nanoformulation uniformity without aggregation, high stability of nanoparticles, and the optimised nanoformulation concentration used in our systems.

# Chapter 5

## Drug activity after packaging into the PLGA nanoparticles

---

## 5.1 Introduction

Macrophage migration inhibitory factor (MIF), a pivotal proinflammatory cytokine, which has been implicated in the pathogenesis of inflammation and cancer [263]. As previously highlighted in this thesis, over expression of MIF has been associated with tumour aggressiveness and poor survival rates [19, 264]. MIF's tautomerase activity has been implicated in cancer biology. Specifically inhibiting this enzymatic activity via small molecular weight inhibitors has been shown to significantly inhibit cancer proliferation and metastatic spread [19, 265, 266]. All these studies add significant weight to the expanding body of evidence that targeting the enzymatic active site of MIF represents a valid and novel therapeutic target in cancer. In the context of lung cancer, evidence has been presented linking MIF activity to cell proliferation, carcinogenesis, and the development of malignancy [267, 268]. Pre-clinical studies have revealed that stimulating the cells with recombinant MIF resulted in a significant increase in cell proliferation [67, 269]. For instance, in a recent study, treating Lewis lung carcinoma cell (LLC) with human recombinant MIF (100 ng/ml) resulted in 100% increase in cancer cell proliferation [24]. Professor Donnelly's research group has recently described a novel MIF inhibitor (SCD19), which was identified via a computational virtual screening of putative ligand binding sites. As explained previously in the thesis introduction (see 1.1.5), SCD19 has been shown to effectively reduce tumour size in a murine lung cancer model [24]. In this thesis we investigated whether the design of an aerosolised pulmonary delivery of our SDC19 packaged into PGLA nanocarrier offered promise as a targeted therapy for lung cancer. We have used a cell free tautomerase assay, to investigate the efficacy of the MIF inhibitors [270-272]. As part of this screening process we generated sufficient quantities of human recombinant MIF (rMIF) via using transformed *E.coli* BL21 (DE3) bacteria containing the pET11b-MIF recombinant plasmid, which was provided by Prof. Richard Bucala, Yale university, USA. Subsequently, the expressed recombinant human MIF was purified via anion exchange chromatography and fast protein liquid chromatography (FPLC). After

endotoxin removal, this produced recombinant MIF was also used to stimulate cell proliferation in LLC cells to examine the ability of PLGA-SCD19 nanoparticles to decrease cell proliferation.

## 5.2 Results

### 5.2.1 Expression and purification of human recombinant MIF

#### (rMIF)

To confirm the presence of the pET11b-MIF plasmid in transformed *E.coli BL21 (DE3)* bacteria, the bacteria were inoculated into the selective medium containing 50 µg/ml ampicillin, followed by colony PCR method. Figure 5.1 shows that transformed *E.coli BL21 (DE3)* bacteria grow in LB broth and on LB agar selective media, owing to the ampicillin resistance gene located on pET11b plasmid back bone. Also, the presence of the inserted human MIF cDNA was verified by colony PCR. As can be seen in Figure 5.2, a single and sharp PCR product, the MIF gene, was present in all the nine randomised single colonies which have been inoculated on a grade plate as a safe source of transformed bacteria. This gene is 345 bp in size and is found to be located within this range on the gel relative to the ladder (between the standard ladders 300-400 bp). The lane 1 had the most intense and sharp band, so this single colony was selected as the best candidate for large scale culture and protein expression. The negative control (C) contains only PCR master mix that was not inoculated with bacteria. As was expected, no MIF PCR product can be seen in this lane.

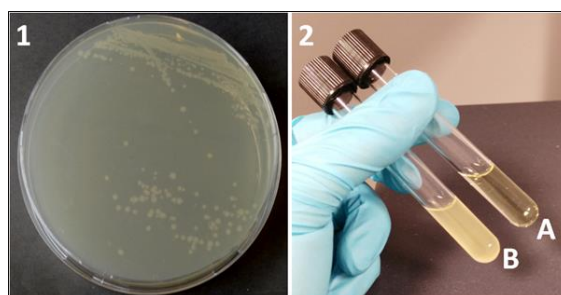


**Figure 5.1:** Antibiotic selective media for isolation transformed bacteria (*E. coli BL21 (DES)*) containing pET11b-MIF. 1) LB agar with 50 µg/ml ampicillin. 2A) LB broth medium with 50 µg/ml ampicillin overnight incubated at 37 °C (negative control). 2B) LB broth with 50 µg/ml ampicillin and a single colony of *E. coli BL21 (DE3)* bacteria containing pET11b-MIF, after overnight incubation at 37 °C.

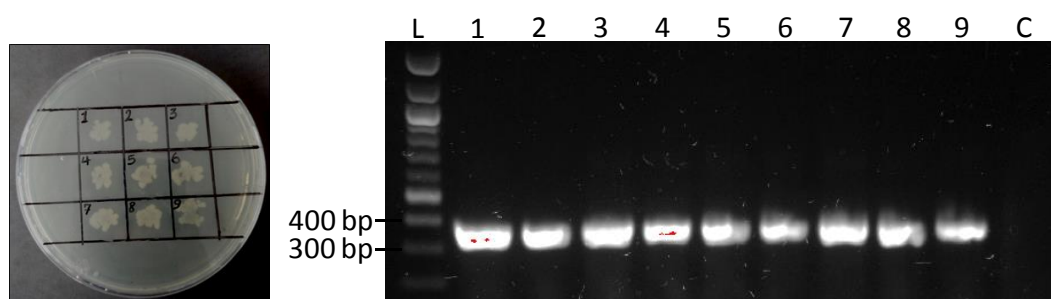


**Figure 5.2:** Colony PCR screening for transformed *E. coli BL21 (DES)* by rMIF-pET11b. Left panel, Bacteria grid plate of the transformed *E. coli BL21 (DES)* by rMIF-pET11b In LB agar with ampicillin (50 µg/ml). Nine randomly picked colonies were swabbed onto each grid and incubated at 37 °C. All nine colonies were screened by colony PCR to verify the existence of rMIF-pET11b plasmid in the *E. coli BL21 (DES)*. This grid plate provides a safe source of several transformed single colony for future work to select best single colony for expression of the human recombinant MIF (rMIF) protein. Right panel, Colony PCR screening of nine randomly picked colonies identified all positive colonies with PCR bands of the expected 345 bp size. bp= base pair. L= DNA ladder (Invitrogen, Cat #15628-019). Lane 1 to 9= colonies number. C= negative control.

Based on the results of the colony PCR, the colony number 1 was chosen and used for rMIF expression. The protein expression was performed into two Erlenmeyer flasks, each consist of 1 litre of LB broth and 50 µg/ml of ampicillin. After IPTG induction, bacterial pellets were prepared and subsequently the cells were lysed by vigorous sonication. The lysed cells were centrifuged to separate cell debris and supernatant. Both cell debris and supernatant were analysed by employing SDS-PAGE technique to detect the expressed recombinant MIF (rMIF). The size of MIF monomers is 12.5 kD and as can be seen in figure 5.3 (Left panel)

Lanes 1 and 2, both of which are the supernatant of induced samples, display significant bands present in the 10-15kD region. Whereas in the supernatant of uninduced samples, Lane 3 and 4, no significant bands are found. The induced supernatants (lane 1 and 2) were collected for additional purification stages to remove unwanted protein bands which were mostly located between 15-37kD region (figure 5.3).

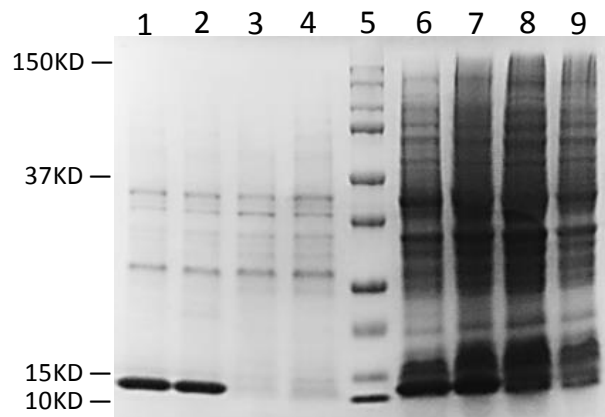


**Figure 5.3:** Analysis the expressed recombinant protein (rMIF) band. Left panel, two Erlenmeyer flasks (batch one and batch two) containing one litre LB broth, ampicillin (50 µg/ml), and *E. coli* BL21 (DES)-rMIF-pET11b were prepared. Before inducing the bacteria by IPTG (100 mM) at the OD 0.6, one millilitre of each batch was taken as uninduced protein samples (negative control). Then the bacteria were shaken for further 3h at 37 °C and harvested by centrifuge. Finally, the bacteria were lysed, and cell debris and supernatants were separated by centrifuge. Ten-microliter aliquots were taken from each sample, electrophoresed in 12% Mini-protean TGX Precast Gel (Bio-Rad), and stained by Coomassie® Brilliant blue R 250. Lane 1 and 2, induced supernatants (batch I and II). Lane 3 and 4, uninduced supernatants (batch one and two). Lane 5, ladder. Lane 6 and 7, induced cell debris (batch one and two). Lane 8 and 9, uninduced cell debris (batch I and II). The rMIF band of the expected 12.5 KD size can be seen in lane 1 and 2.

Following protein expression analysis, the supernatant from induced cells, which was found to carry human rMIF, was loaded onto a HiPrep mono QFF anion exchange column. The elution process was monitored by an UV trace to detect protein in the fractions eluting from the column over the time. The recombinant protein was eluted in the flow through fractions since it does not interact with the column. Figure 5.4, lane 1, shows the collected and pooled

samples from the anion exchange column as the first purification step. Before loading the sample on the gel filtration column, the pooled sample (15 ml) was concentrated (microconcentrator 10,000 MWCO) to obtain a proper volume (2 ml). Figure 5.4 illustrates the concentrated samples (lanes 2 and 3) from the batches one and two. Because of the concentration operation, all the unwanted protein bands are more visible compared to unconcentrated sample which can be seen in lane 1. To remove the remained unwanted band, the concentrated sample was subsequently loaded onto a HiLoad 16/600 superdex 200pg gel filtration column. The sample was eluted by running buffer and the fractions were analysed by SDS-PAGE, based on the UV trace that was previously described. Figure 5.4 illustrates the result of last purification. As can be seen in the lanes 2, 3, and 4 larger proteins migrated more faster than small protein which is the typical pattern of gel filtration chromatography. The fractions of 6, 7, 8, and 9 were found to be pure with a sharp band of the expected rMIF (12.5 KD size). Eluted fractions containing pure rMIF were pooled together, concentrated to achieve the final volume of 2 ml and stored at -80 °C for further studies.

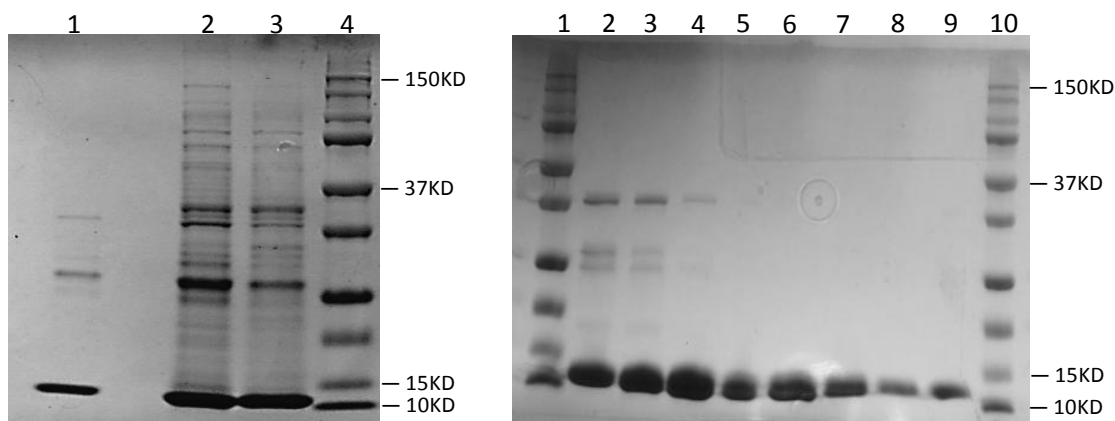


**Figure 5.4:** Analysis the purified recombinant protein (rMIF) bands. Left panel, first purification step was conducted by employing anion exchange chromatography (HiPrep™ Q Fast Flow 16/10) on the collected induced supernatants samples. ten-microliter aliquots were taken from each sample and electrophoresed in 12% Mini-protean TGX Precast Gel (Bio-Rad). The protein bands were stained by Coomassie® Brilliant blue R 250. Lane 1, Pooled samples after running the ion exchange chromatography (before concentration procedure). Lanes 2 and 3, concentrated samples (batch one and two) by an Amicon Ultra-15 Centrifugal Filter (ufc901024-merck millipore). Lane 4, ladder. Right panel, the analysis the purified recombinant protein (rMIF) bands after final purification which was performed by using fast gel filtration chromatography technique (Hiload 26/600 superdex 200 pg column). Ten-microliter aliquots were taken from MIF-containing fractions at each purification step, analysed to find the highest pure fractions. Lanes 1 and 10, ladders. Lanes 2-9 collected fractions.

## 5.2.2 Endotoxin removal and enzyme activity of purified rMIF

The endotoxin (LPS) was removed from rMIF by using a Pierce® High-Capacity Endotoxin Removal kit as described previously in section 2.19.4. To ensure the efficiency of LPS removal, the concentration of endotoxin in contaminated rMIF was assessed and compared to LPS free rMIF by using a LAL assay kit. As can be seen in figure 5.5 A, the LPS concentration in the contaminated sample was approximately 3 EU/ml, but in LPS free batch the mean concentration was only 0.15 EU/ml. As was mentioned previously in the section 3.1.2, one endotoxin unit (EU) equals approximately 0.1 to 0.2 ng endotoxin/ml of solution [186]. Following LPS depletion, the concentration of rMIF was evaluated by a BCA protein assay kit to find out how much protein can be recovered from the endotoxin removal column. The LPS contaminated rMIF sample and LPS free sample had a concentration of 1.2 mg/ml and 1 mg/ml,

respectively, which revealed 15% loss of total sample during this LPS removal process. To ensure that the remain LPS has no impact on inflammatory response which is very sensitive to LPS contamination, the safety of LPS free rMIF was examined by measuring the level of TNF- $\alpha$  in the RAW 264.7 macrophage cell line treated by two different concentrations (100 and 500 ng/ml) of LPS free rMIF for 24 h. The concentration of TNF- $\alpha$  was measured using a R&D TNF- $\alpha$  Duo Set ELISA (see Methods chapter, section 2.20). Figure 5.5 B shows the level of TNF- $\alpha$  expression and demonstrates that at the even high concentration of LPS free rMIF (500 ng/ml) the TNF- $\alpha$  release was on the same level with untreated cells (medium) and the TNF- $\alpha$  level for all tests were approximately 0.06 ng/ml. As was discussed previously in the introduction chapter, there is a direct correlation between MIF's enzyme activity (tautomerase) and its physiological function. Therefore, it was important to ensure the purified rMIF is enzymatically active after purification and LPS removal steps. Figure 5.5 C illustrates the enzymatic activity of the LPS free rMIF at 100 ng/ml concentration, indicating that the purification and LPS removal procedure had no adverse impact on the enzyme activity of the recombinant protein. We also investigated the activity of our drug candidate, SCD19, before packaging into the PLGA nanoparticles to ensure that it inhibits effectively the tautomerase activity of MIF. As can be seen in figure 5.6, SCD19 at the concentration of 100  $\mu$ M blocked almost 100% of the rMIF's tautomerase activity, while untreated rMIF showed a proper enzyme activity. This is demonstrated by the curve that is generated as the dark red substrate (L-dopachrome methyl ester) is converted to the colourless product, which know as dopachrome methyl ester tautomerase assay.

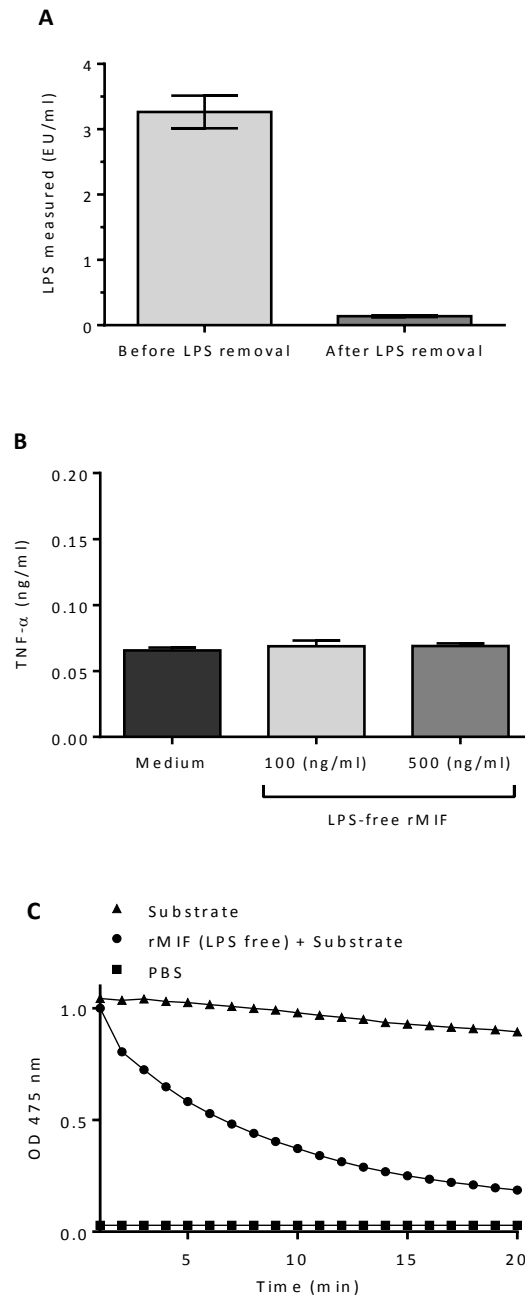


**Figure 5.5:** LPS removal and analysis the activity of purified recombinant MIF (rMIF). A) The concentration of LPS in rMIF before and after LPS removal measured by a Pierce high capacity endotoxin removal resin. The protein concentration as determined by using a BCA protein assay kit was 1mg/ml. B) The effect of LPS free rMIF on TNF- $\alpha$  release in RAW macrophage cells. RAW macrophage cells were plated at  $1 \times 10^5$  per well and treated with 100 ng/ml and 500 ng/ml LPS free rMIF. After 24 h, supernatants were collected and assessed for levels of TNF $\alpha$  by ELISA. Data is presented as mean  $\pm$  SEM (n=3). No change was detected in either 100 or 500 ng/ml LPS free rMIF (100 ng/ml) compared to untreated cells. C) Cell free tautomerase assay of rMIF. Recombinant MIF was incubated with L-dopachrome methyl ester substrate and the activity of the rMIF was assessed by measuring absorbance at 475 nm over 20 min.

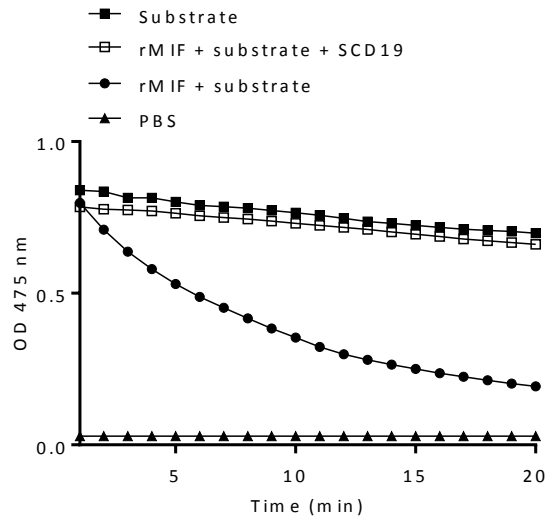


**Figure 5.6:** The activity of SCD19 to inhibited MIF enzymatic activity. Recombinant MIF was incubated with or without (control) SCD19 (100  $\mu$ M) for 20 minutes in room temperature, then the substrate (L-dopachrome methyl ester) was added and the activity of the rMIF was assessed by measuring absorbance at 475 nm over 20 min.

### 5.2.3 Inhibition of cell proliferation in Lewis lung carcinoma cells

We examined the ability of nebulised SCD19 loaded in PLGA nanoparticles (PLGA-SCD19) to inhibit the cell proliferation of Lewis lung carcinoma cell line (LLC). From figure 5.7 it can be seen that MIF stimulates (untreated cells + MIF (100 ng/ml)) proliferation of Lewis lung carcinoma cell line (LLC) significantly compared to untreated cells \*\*\* $p < 0.001$ . PLGA-SCD19 nanoparticles significantly decreased the MIF induced cell proliferation to levels similar with untreated cells \*\*\* $p < 0.001$ . Also, PLGA-SCD19 nanoparticles reduced significantly the cell proliferation of LLC cell line compared to PLGA nanoparticles (negative control) \* $p < 0.05$ .

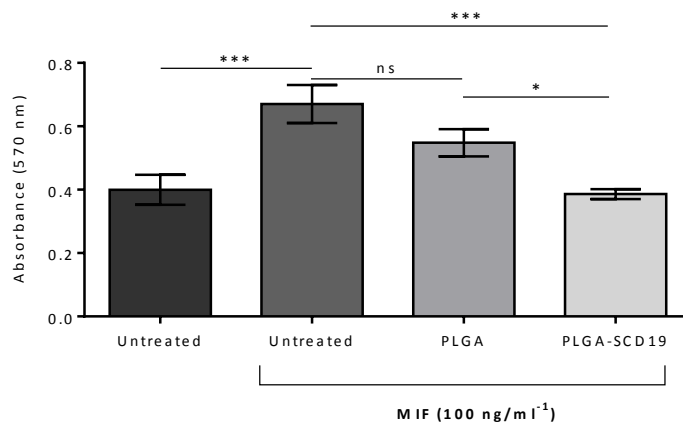


**Figure 5.7:** Inhibition of cell proliferation in Lewis lung carcinoma cell (LLC) by nebulised PLGA-SCD19 nanoparticles. The effect of nebulised PLGA-SCD19 nanoparticles on Lewis lung carcinoma cell growth was evaluated by MTT assay. The LLC were seeded at the density of  $2 \times 10^2$  per well, then treated by PLGA nanoparticles (negative control) and PLGA-SCD19 nanoparticles carrying (SCD19 100  $\mu$ M) one day prior to the two days stimulation by rMIF (100 ng/ml). Data is presented as mean  $\pm$  SEM (n=9). A one-way ANOVA with Tukey- Kramer post-test (compare all pairs of columns) was used to test for statistical significance of differences. \*\*\* $p < 0.001$ , untreated versus untreated + MIF. \*\*\* $p < 0.001$ , untreated + MIF versus PLGA-SCD19 (100  $\mu$ M) [medium: control, LLC cells stimulated by rMIF]. \* $p < 0.05$ , PLGA versus PLGA-SCD19 (100  $\mu$ M).

### 5.3 Discussion

Changes in the cell-cycle allow malignant cells to escape the normal control of cell proliferation [273]. The critical role of MIF in cellular proliferation have been highlighted in numerous studies [19, 24, 274-279]. As previously highlighted, MIF promotes cell proliferation via three main cell signalling pathways such as MAPK/ERK [280], JNK/c-Jun/AP-1 [281], and PI3K/Akt/mTOR [275], resulting in the development of cancer and tumour growth [19]. In this current chapter, we investigated whether our novel drug nanoformulation (PLGA-SCD19) could significantly reduce LLC cell proliferation.

We expressed human recombinant MIF through IPTG induction protein expression method from a pET11b-MIF recombinant plasmid which carries MIF cDNA, since there is cDNA copy of the gene in the recombinant plasmid, it can be expressed in bacterial expression hosts (e.g. *E.coli BL21* (DE3)) as no post-

transcription modification is required for MIF cDNA. A high-yield purification of recombinant human macrophage migration inhibitory factor (rMIF) was achieved (2 ml of 1.2 mg/ml rMIF) after employing anion exchange chromatography and gel filtration chromatography, respectively. Although, bacterial expression systems have many benefits such as; rapid expression, high yields, and ease of culture [282], there is a considerable LPS contamination issue with the purified recombinant protein which can cause misleading experimental results in both *in vitro* and *in vivo* studies. To tackle this issue, we employed an endotoxin binding resin to deplete the LPS contamination to a safe level. The results of endotoxin assay (LAL assay) showed that the concentration of LPS in one milligram of rMIF, after LPS removal procedure, is 0.15 EU/ml. Considering the fact that the working concentration of rMIF is 100 ng/ml and the purified rMIF should be diluted by  $10^6$  times, consequently, the final concentration of the LPS is  $1.5 \times 10^{-7}$  EU/ml or  $3-1.5 \times 10^{-3}$  pg/ml as each 1 EU/ml is 0.1-0.2 ng/ml. LPS is a strong inflammatory mediator which triggers immune cells via Toll-like receptors (TLRs) leading to the secretion of pro-inflammatory mediators (e.g. TNF- $\alpha$ ). To assess whether our purified rMIF possessed and physiologically relevant LPS contamination we assessed whether this recombinant protein could induce a significant pro-inflammatory response from immune cells and found no significant induction of TNF compared to control medium. Before packaging the SCD19 into PLGA nanoparticles, we investigated the activity of the drug candidate to inhibit MIF's enzyme activity. The dopachrome tautomerase assay showed that SCD19 (100  $\mu$ M) inhibited almost 100% of MIF's enzyme activity compared to untreated rMIF. In the *in vitro* experiment, rMIF (100 ng/ml) increased cell proliferation of LLC cancer cells by more than 30%. This data is in support of results published by others, who showed that rMIF increased significantly cell proliferation in different cells, leading to tumour growth and cancer development [24, 283-285]. Treated cancer cells by the nebulised nanoformulation carrying 100  $\mu$ M of SCD19 led to almost 50% cell proliferation reduction compared to untreated cells. This result was similar to previous results, which free SCD19 was applied to decrease cell proliferation from rMIF-

Induced cell proliferation in LLC cancer cell line [24]. However, vibrating mesh nebulisers are inoperative when working with free SCD19 due to the DMSO solvent which is required to dissolve free SCD19 and can potentially damage the nebuliser's vibrating mesh. In fact, the vast majority of the small-molecule MIF inhibitors are only soluble in organic solvents (e.g. DMSO), including ISO-1 which is the commercially available MIF inhibitor [286]. Nanodrug delivery systems can tackle this issue providing long-term stable and well-dispersed drug loaded nanoparticles in both saline and water that can be administered directly into the lungs via inhalation, thus, avoiding the use of hazardous solvents.

# Chapter 6

## Discussion

---

The main focus of this PhD thesis was to investigate the synthesis and characterisation of an aerosolised PLGA nanodrug delivery system as a novel nanoparticle formulation for MIF enzyme inhibitors to modulate MIF's physiological activity in pulmonary diseases, particularly lung cancer. SCD19 (MIF inhibitor)-loaded PLGA nanoformulation overcame the water solubility issues associated with SCD19 and enabled high levels of lung-specific deliver of active compound with minimum toxicity.

Cancer is the second leading cause of death worldwide, estimated to be accountable for 9.6 million deaths and 18.1 million new cases in 2018. Lung cancer is the most frequently diagnosed cancer (11.6% of the total cases) and the leading cause of cancer death (18.4% of the total death) [287]. Most of the lung cancer patients present with advanced stage cancer with very limited therapeutic options and many should be cured by surgery. However, around 50% die of their disease despite curative resection [288]. As we have highlighted previously, MIF has been implicated as a key protein driving cancer growth and inhibiting its unique tautomerase enzymatic activity has been shown to significantly inhibit cancer proliferation. This formed the basis for our work developing an aerosolised lung delivery system of a nanopackaged MIF enzymatic inhibitor.

Our original hypothesis was that this inhalable nanodrug carrier can provide all the advantages of an inhalational and nanocarrier based drug delivery approach to improve treatment efficiency with minimum local and systemic toxicity. To investigate this, we encapsulated our novel MIF enzyme inhibitor, SCD19, into PLGA nanospheres (PLGA-SCD19) by using an oil in water (o/w) or single emulsion-solvent evaporation technique. We examined the properties of the drug loaded nanoparticles to ensure they meet the essential and desirable criteria. A transmission electron microscope (TEM) and a scanning electron microscope (SEM) were utilised to measure the size and to observe and detect

surface morphology and structural characteristics of the nanoparticles. Also, nanoparticle tracking analysis (NTA) and dynamic light scattering (DLS) technique were applied to determine the size distribution of the nanoparticles in liquid suspension and the surface charge of PLGA-SCD19 nanoparticles. Further characterisations were carried out to investigate the drug content, encapsulation efficiency, yield efficiency, and the release profile of the nanoformulation, followed by the stability of the nanoparticles in artificial lung fluids, this experiment was performed to investigate the nanoparticles aggregation or lose their uniformity of size and shape in artificial lysosomal fluid and artificial lung fluid. As one of the most crucial steps when developing a nanodrug delivery system, the toxicity and biocompatibility of the PLGA-SCD19 was investigated for different normal and cancerous cell lines by LDH cytotoxicity assay and high-content analysis (HCS). The cellular uptake of the PLGA-SCD19 was also evaluated in adenocarcinomic human alveolar basal epithelial cells (A549 cells) by using three different techniques; Prussian blue staining, ferrozine assay, and confocal microscopy. In this thesis, we aimed to develop an aerosolised nanodrug delivery system for inhalation treatment, therefore we investigated the physical properties of the PLGA-SCD19 administered by Aerogen's vibrating mesh nebulisers. Different techniques and methods were used to characterise the aerosolised PLGA-SCD19. The size distribution, volume median diameter (VMD) and geometric standard deviation (GSD) of the aerosolised PLGA-SCD19 were evaluated by a method known as laser diffraction, this step was necessary to ensure that the properties of the aerosolised nanoparticles are suitable for deep lung deposition. The relative amount of deposition of the nanoparticles in the different regions of the lung was investigated and determined by utilising a Next Generation Impactor (NGI), this experiment was conducted to evaluate the amount of the deposited PLGA-SCD19 in both the upper and lower respiratory tract. Further experiments were performed to assess the drug delivery efficiency of the aerosolised PLGA-SCD19 by using a mechanical ventilator and a human breathing simulator. Finally, we examined the activity of the encapsulated

SCD19 to inhibit cell proliferation from a MIF-induced cell proliferation model in lewis lung cancer (LLC) cell line.

MIF represents a well-defined, pleiotropic, pro-inflammatory mediator of the immune system that plays a substantial role in the overall inflammatory cascade. MIF is a Swiss Army Knife-type of small protein with many biological functions which led to it being considered as a cytokine, enzyme, hormone, and molecular chaperone [19, 289]. Within our group the focus is on the vital regulator of innate immunity MIF, which has been associated with a wide range of diseases, including lung cancer. It has been well demonstrated that inflammation has influential effects on tumour development [290]. The role of MIF's biological activities in tumour growth, angiogenesis, and cancer progression is now well supported by published work. Studies also have shown that overexpression of MIF is closely associated with tumour aggressiveness and metastatic potential [19, 72, 268, 278, 291-294]. MIF possesses a unique and intriguing enzyme activity (tautomerase) which its role and human physiological substrate has not been identified thus far. However, it has been shown that MIF's enzyme activity contributes to the biological functional activity of MIF [24, 294]. Thus, the tautomerase active site is considered as the logical binding site for potential inhibitors of MIF function [271, 289, 295, 296]. Our lab has recently reported the discovery of a small-molecular-weight inhibitor, known as SCD19, which targets the active enzymatic site of MIF. In a recent study, SCD19 was found to markedly reduce tumour growth compared to untreated tumour in a murine lung cancer model [24], in another study, SCD19 decreased significantly the inflammatory response in a murine pulmonary chronic *P. aeruginosa* model [40], representing a robust and effective candidate to the concept of anti-MIF strategy as a potential future anti-inflammatory/anti-cancer therapeutic approach. In this current study, we report the maximise local delivery of MIF therapeutics directly to the lungs through the development of an aerosolised delivery system utilising state of the art nanoparticles.

Nanoparticles are among the most extensively studied drug delivery vehicles which, in turn, are currently the most common application of nanotechnology in the field of nanomedicine [297]. Nano particle aerosolised delivery systems to the lung represent a novel future therapeutic strategy for cancer and in particular lung cancer. [125]. Nanocarrier based drug delivery systems can increase the drug therapeutic index, contributing to improve treatment efficiency with less drug toxicity and significantly less adverse effect compared to free drugs [129]. Nanodrug delivery system administrated by the pulmonary route as a targeted drug therapy and non-invasive route represents a promising strategy for the treatment of respiratory diseases [124, 125].

In this thesis, we took advantage of both nanotechnology-based drug delivery system and the inhalation route for administration of our novel MIF inhibitor, SCD19, to provide a safe and effective treatment platform. We decided to encapsulate SCD19 in poly (lactic-co-glycolic acid) or PLGA, a natural polymer nanodrug delivery vehicle, due to numerous advantages of this biodegradable, nontoxic and FDA approved nanodrug delivery system [226]. A standard method, single emulsion-solvent evaporation technique, was used to encapsulate SCD19 into PLGA nanoparticles. The first challenge was to produce LPS free nanoparticles, since nanoparticles can be contaminated easily by endotoxins during the synthesis procedure which causes a massive immune response in both *in vitro* and *in vivo* studies [183]. The endotoxin assay showed that the produced PLGA-SCD19 nanoparticles were relatively endotoxin-free. The second challenge was to produce uniform size distribution of the PLGA-SCD19 nanoparticles. In fact, nonuniform size distribution, lack of reproducibility, and lack of stability are considerable as the most challenging obstacles when developing a nanodrug delivery system [129]. NTA analysis was employed to investigate the hydrodynamic diameter of the PLGA-SCD19 nanoparticles dispersed in 0.9% (w/v) saline and water which resulted in a single and sharp peak, approximately 200 nm in diameter, indicating that the nanoparticles were uniform without aggregation. Also, TEM and SEM images of

the nanoparticles showed a uniform spherical shape with smooth surfaces. It is noteworthy that spherical nanoparticles are taken up effectively by the cellular mechanisms of phagocytosis owing to the actin structure of the cells that must be formed to initiate phagocytosis and let cell membrane progress and then move over the nanoparticle [298]. To confirm the cellular uptake, we co-encapsulated iron oxide nanoparticles (MNPs) and SCD19 into PLGA. The MNPs were added for detection and imaging purpose to observe the cellular uptake of our nanoparticles. We carried out three methods; Prussian blue assay, ferrozine assay, and confocal microscopy, to investigate the cellular uptake of the PLGA-MNP-SCD19. All three techniques showed that significant accumulations of nanoparticles occurred in the cells after overnight incubation. The stability of the developed nanoformulation was an important consideration in our study, since unstable nanoparticles tend to form sedimentation, agglomeration, and crystallisation [299]. The zeta potential value of the PLGA-SCD19 was in a range,  $-28.2 \pm 5.45$  Mv, that would typically be considered high in regard to stability [206], moreover further studies to examine the stability of the nanoparticles in lung artificial fluids (LAFs) showed that the nanoparticles remained monodispersed without any aggregation in ALFs. The drug content, yield and encapsulation efficiency were constant for all examined batches which shows the reproducibility of the nanoformulation. Toxicological study for our nanoformulation was one of the top considerations in this study. We performed LDH cytotoxicity assay and HCS analysis to evaluate the capacity of the PLGA-SCD19 to induce acute cell toxicity. In both evaluations the nanoparticles were found to be non-toxic to cells.

In this study, we established a collaboration with Aerogen Ltd, one of the world's leading medical device companies specialising in the design and production of aerosol drug delivery devices. Initially, we optimised our nanoformulation for Aerogen's vibrating mesh nebuliser to achieve maximum drug delivery within acceptable nebulisation times. The vibrating mesh nebuliser did not affect the size nor the volume of PLGA-SCD19 nanoparticles compared to

nanoparticles pre-nebulisation. In our work we noticed that the nanoparticles concentration is relevant for nebulisation efficiency, where higher concentrations of nanoparticles can bring about vibrating mesh clogging issues which leads to reduced delivery efficiency.

We further characterised the properties of the aerosolised PLGA-SCD19 nanoparticles by using a laser diffraction method which revealed that they had a perfectly acceptable volume mean diameter with an optimal particle size distribution for deep lung deposition. This leads to improve treatment efficiency by allowing aerosols to access the small airways with minimum waste [300]. Further investigation to evaluate the regional deposition of the aerosol nanoparticles in an advanced human respiratory tract model, resulted in high deposition in the alveolar region of the lung model with very low deposition in upper respiratory tract. Additional experimental methods to define drug delivery efficiency included; the human breathing simulator and a human mechanical ventilator simulator. Previous studies of other compounds had shown a wide range of drug delivery efficiency (from 1% to 16%) possibly due to different factors, such as inhaler devices and drug formulation [262]. In this study we achieved 23% and 14% drug delivery efficiency from the mechanical ventilator and the breathing simulator machine, respectively. Finally, we examined the ability of our aerosolised PLGA-SCD19 nanoparticles to reduce cell proliferation in a MIF-induced cell proliferation *in vitro* model which resulted in a significant reduction of cell proliferation in the selected cancer cells.

In the context of personalised medicine, MIF represents an ideal therapeutic target. Published work has revealed that a functional MIF polymorphism, a tetranucleotide microsatellite (-794 CATT<sub>5-7</sub>, rs5844572), is directly implicated in the overexpression of MIF [18]. It has been shown that patients who have 5-CATT repeat have low MIF expression and 6-,7-,8-CATT repeat result in high level expression. Since this polymorphism was identified, numerous studies have shown the association of this polymorphism and cancer development [301-304]. In relation to lung, it has been demonstrated that

patients who have high MIF levels have more aggressive diseases, including COPD [305], Cystic fibrosis [48], and Asthma patients [306]. We proposed that individuals genetically primed to be high MIF producers would have more aggressive disease in lung cancer. Therefore, targeting those individuals with an anti-MIF therapeutic strategy would have significant clinical benefit in lung cancer. A classic example of personalised medicine – getting the right treatment to the patients that would benefit the most. To investigate this, our lab has established a humanised MIF polymorphism mouse model, where the mouse MIF gene has been replaced by the human equivalent incorporating either our 5/5 or 7/7 polymorphism. Thus, being genetically primed to express low levels or high levels of MIF respectively. To ensure our mice were functional the Intraperitoneal macrophages were isolated from both groups and stimulated with PI:C and LPS. From the group the 7-CATT mice have higher basal and stimulated levels of MIF than 5-CATT. For future work we aim to establish a murine lung cancer model by using these novel mice groups to investigate how high and low level of MIF effect lung cancer and secondly incorporate an aerosolised PLGA-SCD19 therapeutic arm to assess efficacy in these murine models of lung cancer. We believe that our nanoformulation can be applied to modulate the physiological activities of MIF in other lung diseases, including Cystic fibrosis, Asthma, and COPD. Therefore, our transgenic mice and nanoformulation methodology will provide a framework for the assessment of new novel treatments for a range of lung diseases. A natural extension of the work presented in this thesis would be the use of our PLGA-SCD19 nanoparticles in alternative administration formats (eg topical, IV, subcutaneous) to treat extrathoracic systemic diseases.

In this thesis we presented work on the synthesis and characterisation of an effective and practical nanodrug delivery shuttle for MIF inhibitors. This study has demonstrated that the developed aerosolised nanodrug delivery system due to its appropriate characteristics and therapeutic activities may be provide a novel adjunctive agent for use with anticancer drugs in the treatment

of patients with lung cancer and the data obtained from characterisation studies may contribute to future drug delivery researches.

# Chapter 7

## Bibliography

---

1. Bloom, B.R.B., Boyce, *Mechanism of a Reaction in Vitro Associated with Delayed-Type Hypersensitivity*. Science, 1966. **153**(3731): p. 80-82.
2. Simons, D., et al., *Hypoxia-induced endothelial secretion of macrophage migration inhibitory factor and role in endothelial progenitor cell recruitment*. Journal of Cellular and Molecular Medicine, 2011. **15**(3): p. 668-678.
3. Nathan, C.F., H.G. Remold, and J.R. David, *Characterization of a lymphocyte factor which alters macrophage functions*. The Journal of Experimental Medicine, 1973. **137**(2): p. 275-290.
4. Weiser, W.Y., et al., *Molecular cloning of a cDNA encoding a human macrophage migration inhibitory factor*. Proceedings of the National Academy of Sciences, 1989. **86**(19): p. 7522-7526.
5. Bernhagen, J., et al., *MIF is a pituitary-derived cytokine that potentiates lethal endotoxaemia*. Nature, 1993. **365**: p. 756-759.
6. Calandra, T., et al., *The macrophage is an important and previously unrecognized source of macrophage migration inhibitory factor*. The Journal of Experimental Medicine, 1994. **179**(6): p. 1895-1902.
7. Oliver, F., et al., *Regulated secretion of macrophage migration inhibitory factor is mediated by a non-classical pathway involving an ABC transporter*. FEBS Letters, 2003. **551**(1-3): p. 78-86.
8. Bacher, M., et al., *An essential regulatory role for macrophage migration inhibitory factor in T-cell activation*. Proceedings of the National Academy of Sciences of the United States of America, 1996. **93**(15): p. 7849-7854.
9. Rossi, A.G., et al., *Human circulating eosinophils secrete macrophage migration inhibitory factor (MIF). Potential role in asthma*. Journal of Clinical Investigation, 1998. **101**(12): p. 2869-2874.
10. Daryadel, A., et al., *Apoptotic Neutrophils Release Macrophage Migration Inhibitory Factor upon Stimulation with Tumor Necrosis Factor- $\alpha$* . Journal of Biological Chemistry, 2006. **281**(37): p. 27653-27661.
11. Roth, S., et al., *Secondary necrotic neutrophils release interleukin-16C and macrophage migration inhibitory factor from stores in the cytosol*. Cell Death Discovery, 2015. **1**: p. 15056-9.
12. Calandra, T. and T. Roger, *Macrophage migration inhibitory factor: a regulator of innate immunity*. Nature Reviews Immunology, 2003. **3**(10): p. 791-800.
13. Budarf, M., et al., *Localization of the Human Gene for Macrophage Migration Inhibitory Factor (MIF) to Chromosome 22q11.2*. Genomics, 1997. **39**(2): p. 235-236.
14. Paralkar, V. and G. Wistow, *Cloning the Human Gene for Macrophage Migration Inhibitory Factor (MIF)*. Genomics, 1994. **19**(1): p. 48-51.
15. Zhu, J., et al., *On the nature of human housekeeping genes*. Trends in Genetics, 2008. **24**(10): p. 481-484.
16. Waeber, G.r., et al., *Transcriptional Activation of the Macrophage Migration-Inhibitory Factor Gene by the Corticotropin-Releasing Factor is Mediated by the Cyclic Adenosine 3',5'-Monophosphate Responsive*

- Element-Binding Protein CREB in Pituitary Cells*. *Molecular Endocrinology*, 1998. **12**(5): p. 698-705.
17. Baugh, J.A., et al., *Dual regulation of macrophage migration inhibitory factor (MIF) expression in hypoxia by CREB and HIF-1*. *Biochemical and Biophysical Research Communications*, 2006. **347**(4): p. 895-903.
  18. Baugh, J.A., et al., *A functional promoter polymorphism in the macrophage migration inhibitory factor (MIF) gene associated with disease severity in rheumatoid arthritis*. *Genes And Immunity*, 2002. **3**: p. 170.
  19. Ciaran, O.R., et al., *Targeting MIF in Cancer: Therapeutic Strategies, Current Developments, and Future Opportunities*. *Medicinal Research Reviews*, 2016. **36**(3): p. 440-460.
  20. Costa-Silva, B., et al., *Pancreatic cancer exosomes initiate pre-metastatic niche formation in the liver*. *Nature Cell Biology*, 2015. **17**: p. 816.
  21. Suzuki, M., et al., *Crystal structure of the macrophage migration inhibitory factor from rat liver*. *Nature Structural Biology*, 1996. **3**: p. 259–266.
  22. Ishizaka, K., et al., *Biochemical Basis of Antigen-Specific Suppressor T Cell Factors: Controversies and Possible Answers*, in *Advances in Immunology*, F.J. Dixon, Editor. 1999, Academic Press. p. 1-60.
  23. Rosengren, E., et al., *The immunoregulatory mediator macrophage migration inhibitory factor (MIF) catalyzes a tautomerization reaction*. *Molecular Medicine*, 1996. **2**(1): p. 143-149.
  24. Mawhinney, L., et al., *Macrophage Migration Inhibitory Factor (MIF) Enzymatic Activity and Lung Cancer*. *Molecular Medicine*, 2014. **20**(1): p. 729-735.
  25. Fingerle-Rowson, G., et al., *A Tautomerase-Null Macrophage Migration-Inhibitory Factor (MIF) Gene Knock-In Mouse Model Reveals That Protein Interactions and Not Enzymatic Activity Mediate MIF-Dependent Growth Regulation*. *Molecular and Cellular Biology*, 2009. **29**(7): p. 1922-1932.
  26. Sun, H.W., et al., *Crystal structure at 2.6-Å resolution of human macrophage migration inhibitory factor*. *Proceedings of the National Academy of Sciences of the United States of America*, 1996. **93**(11): p. 5191-5196.
  27. Bernhagen, J., et al., *MIF is a noncognate ligand of CXC chemokine receptors in inflammatory and atherogenic cell recruitment*. *Nature Medicine*, 2007. **13**: p. 587.
  28. Mitchell, R.A., et al., *Macrophage migration inhibitory factor (MIF) sustains macrophage proinflammatory function by inhibiting p53: Regulatory role in the innate immune response*. *Proceedings of the National Academy of Sciences of the United States of America*, 2002. **99**(1): p. 345-350.
  29. Kleemann, R., et al., *Intracellular action of the cytokine MIF to modulate AP-1 activity and the cell cycle through Jab1*. *Nature*, 2000. **408**: p. 211-216.

30. Hudson, J.D., et al., *A Proinflammatory Cytokine Inhibits P53 Tumor Suppressor Activity*. The Journal of Experimental Medicine, 1999. **190**(10): p. 1375-1382.
31. Burger-Kentischer, A., et al., *Expression of Macrophage Migration Inhibitory Factor in Different Stages of Human Atherosclerosis*. Circulation, 2002. **105**(13): p. 1561-1566.
32. Pyle, M., et al., *Macrophage migration inhibitory factor expression is increased in pituitary adenoma cell nuclei*. Journal of Endocrinology, 2003. **176**(1): p. 103-110.
33. Bucala, R., *A most interesting factor*. Nature, 2000. **408**: p. 146–147.
34. Finger, E.C. and A.J. Giaccia, *Hypoxia, inflammation, and the tumor microenvironment in metastatic disease*. Cancer metastasis reviews, 2010. **29**(2): p. 285-293.
35. Winner, M., et al., *Amplification of Tumor Hypoxic Responses by Macrophage Migration Inhibitory Factor–Dependent Hypoxia-Inducible Factor Stabilization*. Cancer research, 2007. **67**(1): p. 186-193.
36. Amin, M.A., et al., *Migration Inhibitory Factor Mediates Angiogenesis via Mitogen-Activated Protein Kinase and Phosphatidylinositol Kinase*. Circulation Research, 2003. **93**(4): p. 321-329.
37. O'Reilly, C., et al., *Targeting MIF in Cancer: Therapeutic Strategies, Current Developments, and Future Opportunities*. Medicinal Research Reviews, 2016. **36**(3): p. 440-460.
38. Bucala, R. and S.C. Donnelly, *Macrophage Migration Inhibitory Factor: A Probable Link between Inflammation and Cancer*. Immunity, 2007. **26**(3): p. 281-285.
39. Steffen, R., et al., *The Role of Macrophage Migration Inhibitory Factor in Critical Illness*. Mini-Reviews in Medicinal Chemistry, 2014. **14**(14): p. 1116-1124.
40. Tynan, A., et al., *Macrophage migration inhibitory factor enhances Pseudomonas aeruginosa biofilm formation, potentially contributing to cystic fibrosis pathogenesis*. The FASEB Journal, 2017. **31**(11): p. 5102-5110.
41. Donnelly, S.C., et al., *Regulatory role for macrophage migration inhibitory factor in acute respiratory distress syndrome*. Nature Medicine, 1997. **3**: p. 320-323.
42. Rendon, B.E., et al., *Regulation of Human Lung Adenocarcinoma Cell Migration and Invasion by Macrophage Migration Inhibitory Factor*. Journal of Biological Chemistry, 2007. **282**(41): p. 29910-29918.
43. Olivieri, C., et al., *Macrophage migration inhibitory factor in lung tissue of idiopathic pulmonary fibrosis patients*. Experimental Lung Research, 2016. **42**(5): p. 263-266.
44. Sauler, M., R. Bucala, and P.J. Lee, *Role of macrophage migration inhibitory factor in age-related lung disease*. American Journal of Physiology-Lung Cellular and Molecular Physiology, 2015. **309**(1): p. L1-L10.

45. Li, J., et al., *Tumor Microenvironment Macrophage Inhibitory Factor Directs the Accumulation of Interleukin-17-producing Tumor-infiltrating Lymphocytes and Predicts Favorable Survival in Nasopharyngeal Carcinoma Patients*. The Journal of Biological Chemistry, 2012. **287**(42): p. 35484-35495.
46. Das, R., et al., *Macrophage migration inhibitory factor (MIF) is a critical mediator of the innate immune response to *Mycobacterium tuberculosis**. Proceedings of the National Academy of Sciences, 2013. **110**(32): p. E2997-E3006.
47. El-Adly, T.Z., et al., *Association of macrophage migration inhibitory factor promoter polymorphism -173G/C with susceptibility to childhood asthma*. Central-European Journal of Immunology, 2016. **41**(3): p. 268-272.
48. Adamali, H., et al., *Macrophage Migration Inhibitory Factor Enzymatic Activity, Lung Inflammation, and Cystic Fibrosis*. American Journal of Respiratory and Critical Care Medicine, 2012. **186**(2): p. 162-169.
49. Weiser, J.N., et al., *Macrophage Migration Inhibitory Factor Is Detrimental in Pneumococcal Pneumonia and a Target for Therapeutic Immunomodulation*. The Journal of Infectious Diseases, 2015. **212**(10): p. 1677-1682.
50. Ohwatari, R., et al., *Serum Level of Macrophage Migration Inhibitory Factor as a Useful Parameter of Clinical Course in Patients with Wegener's Granulomatosis and Relapsing Polychondritis*. Annals of Otolaryngology, Rhinology & Laryngology, 2001. **110**(11): p. 1035-1040.
51. Sauler, M., et al., *Macrophage Migration Inhibitory Factor (MIF) in Pulmonary Arterial Hypertension - Secondary Analysis from FREEDOM-C2*, in *A68. WOW: PHARMACOLOGICAL TREATMENT OF PULMONARY HYPERTENSION*. p. A2281-A2281.
52. Edwards, K.M., et al., *Macrophage Migratory Inhibitory Factor (MIF) May Be a Key Factor in Inflammation in Obstructive Sleep Apnea*. Sleep, 2011. **34**(2): p. 161-163.
53. Husebø, G.R., et al., *Macrophage migration inhibitory factor, a role in COPD*. American Journal of Physiology-Lung Cellular and Molecular Physiology, 2016. **311**(1): p. L1-L7.
54. Wu, G., et al., *Relationship between elevated soluble CD74 and severity of experimental and clinical ALI/ARDS*. Scientific Reports, 2016. **6**: p. 30067-30073.
55. O'Reilly, C., et al., *Targeting MIF in Cancer: Therapeutic Strategies, Current Developments, and Future Opportunities*. Med Res Rev, 2016. **36**(3): p. 440-60.
56. Calandra, T. and T. Roger, *Macrophage migration inhibitory factor: a regulator of innate immunity*. Nat Rev Immunol, 2003. **3**(10): p. 791-800.
57. Sauler, M., R. Bucala, and P.J. Lee, *Role of macrophage migration inhibitory factor in age-related lung disease*. American Journal of Physiology - Lung Cellular and Molecular Physiology, 2015. **309**(1): p. L1-L10.

58. Dela Cruz, C.S., L.T. Tanoue, and R.A. Matthay, *Lung cancer: epidemiology, etiology, and prevention*. Clinics in chest medicine, 2011. **32**(4): p. 605-644.
59. *Cancer*. World Health Organization. 2018; Available from: <http://www.who.int/news-room/fact-sheets/detail/cancer>.
60. Wong, M.C.S., et al., *Incidence and mortality of lung cancer: global trends and association with socioeconomic status*. Scientific Reports, 2017. **7**(1): p. 14300.
61. Coleman, A.M., et al., *Cooperative Regulation of Non-Small Cell Lung Carcinoma Angiogenic Potential by Macrophage Migration Inhibitory Factor and Its Homolog, D-Dopachrome Tautomerase*. The Journal of Immunology, 2008. **181**(4): p. 2330-2337.
62. Tomiyasu, M., et al., *Quantification of Macrophage Migration Inhibitory Factor mRNA Expression in Non-Small Cell Lung Cancer Tissues and Its Clinical Significance*. Clinical Cancer Research, 2002. **8**(12): p. 3755-3760.
63. Balogh, K.N., D.J. Templeton, and J.V. Cross, *Macrophage Migration Inhibitory Factor protects cancer cells from immunogenic cell death and impairs anti-tumor immune responses*. PLOS ONE, 2018. **13**(6): p. e0197702.
64. Costa-Silva, B., et al., *Pancreatic cancer exosomes initiate pre-metastatic niche formation in the liver*. Nature Cell Biology, 2015. **17**: p. 816-26.
65. Kamimura, A., et al., *Intracellular distribution of macrophage migration inhibitory factor predicts the prognosis of patients with adenocarcinoma of the lung*. Cancer, 2000. **89**(2): p. 334-341.
66. Coleman, A.M., et al., *Cooperative Regulation of NSCLC Angiogenic Potential by Macrophage Migration Inhibitory Factor and its Homolog, D-Dopachrome Tautomerase*. Journal of immunology (Baltimore, Md. : 1950), 2008. **181**(4): p. 2330-2337.
67. Arenberg, D., et al., *Macrophage migration inhibitory factor promotes tumor growth in the context of lung injury and repair*. American journal of respiratory and critical care medicine, 2010. **182**(8): p. 1030-1037.
68. Mantovani, A., et al., *Cancer-related inflammation*. Nature, 2008. **454**: p. 436.
69. Conroy, H., L. Mawhinney, and S.C. Donnelly, *Inflammation and cancer: macrophage migration inhibitory factor (MIF)—the potential missing link*. QJM: An International Journal of Medicine, 2010. **103**(11): p. 831-836.
70. Oghumu, S., et al., *Deletion of macrophage migration inhibitory factor inhibits murine oral carcinogenesis: Potential role for chronic pro-inflammatory immune mediators*. International Journal of Cancer, 2016. **139**(6): p. 1379-1390.
71. Meyer-Siegler, K.L., et al., *Inhibition of Macrophage Migration Inhibitory Factor or Its Receptor (CD74) Attenuates Growth and Invasion of DU-145 Prostate Cancer Cells*. The Journal of Immunology, 2006. **177**(12): p. 8730-8739.

72. He, X.-X., et al., *Macrophage migration inhibitory factor promotes colorectal cancer*. *Molecular medicine (Cambridge, Mass.)*, 2009. **15**(1-2): p. 1-10.
73. Choudhary, S., et al., *Macrophage migratory inhibitory factor promotes bladder cancer progression via increasing proliferation and angiogenesis*. *Carcinogenesis*, 2013. **34**(12): p. 2891-2899.
74. Denz, A., et al., *Inhibition of MIF Leads to Cell Cycle Arrest and Apoptosis in Pancreatic Cancer Cells*. *Journal of Surgical Research*, 2010. **160**(1): p. 29-34.
75. Bandres, E., et al., *microRNA-451 Regulates Macrophage Migration Inhibitory Factor Production and Proliferation of Gastrointestinal Cancer Cells*. *Clinical Cancer Research*, 2009. **15**(7): p. 2281-2290.
76. Castro, B.A., et al., *Macrophage migration inhibitory factor downregulation: a novel mechanism of resistance to anti-angiogenic therapy*. *Oncogene*, 2017. **36**: p. 3749-3759.
77. Stein, A., et al., *Pilot Study: Elevated Circulating Levels of the Proinflammatory Cytokine Macrophage Migration Inhibitory Factor in Patients With Chronic Spinal Cord Injury*. *Archives of Physical Medicine and Rehabilitation*, 2013. **94**(8): p. 1498-1507.
78. Wu, S.-P., et al., *Macrophage migration inhibitory factor promoter polymorphisms and the clinical expression of scleroderma*. *Arthritis & Rheumatism*, 2006. **54**(11): p. 3661-3669.
79. Wu, G., et al., *Relationship between elevated soluble CD74 and severity of experimental and clinical ALI/ARDS*. *Scientific Reports*, 2016. **6**: p. 30067.
80. Lubetsky, J.B., et al., *Pro-1 of Macrophage Migration Inhibitory Factor Functions as a Catalytic Base in the Phenylpyruvate Tautomerase Activity*. *Biochemistry*, 1999. **38**(22): p. 7346-7354.
81. Emerich, D.F. and C.G. Thanos, *Nanotechnology and medicine*. *Expert Opinion on Biological Therapy*, 2003. **3**(4): p. 655-663.
82. Luo, D., K.A. Carter, and J.F. Lovell, *Nanomaterial Engineering: shaping future nanomedicines*. *Wiley interdisciplinary reviews. Nanomedicine and nanobiotechnology*, 2015. **7**(2): p. 169-188.
83. Duncan, R. and R. Gaspar, *Nanomedicine(s) under the Microscope*. *Molecular Pharmaceutics*, 2011. **8**(6): p. 2101-2141.
84. Singh, S. and A. Singh, *Current status of nanomedicine and nanosurgery*. *Anesthesia, Essays and Researches*, 2013. **7**(2): p. 237-242.
85. *The Critical Path Opportunities List and Report*. 2006; Available from: <http://wayback.archivet.org/7993/20180125035449/https://www.fda.gov/downloads/ScienceResearch/SpecialTopics/CriticalPathInitiative/CriticalPathOpportunitiesReports/UCM077258.pdf>.
86. Landesman-Milo, D., S. Ramishetti, and D. Peer, *Nanomedicine as an emerging platform for metastatic lung cancer therapy*. *Cancer and Metastasis Reviews*, 2015. **34**(2): p. 291-301.
87. Hussain, S., *Nanomedicine for Treatment of Lung Cancer*, in *Lung Cancer and Personalized Medicine: Novel Therapies and Clinical Management*, A.

- Ahmad and S.M. Gadgeel, Editors. 2016, Springer International Publishing: Cham. p. 137-147.
88. Bölükbas, D.A. and S. Meiners, *Lung cancer nanomedicine: potentials and pitfalls*. *Nanomedicine*, 2015. **10**(21): p. 3203-3212.
  89. Kakkar, A., et al., *Evolution of macromolecular complexity in drug delivery systems*. *Nature Reviews Chemistry*, 2017. **1**: p. 0063.
  90. Irvine, D.J., et al., *Synthetic Nanoparticles for Vaccines and Immunotherapy*. *Chemical Reviews*, 2015. **115**(19): p. 11109-11146.
  91. Buxton, D.B., *Nanotechnology in the diagnosis and management of heart, lung and blood diseases*. *Expert Review of Molecular Diagnostics*, 2007. **7**(2): p. 149-160.
  92. Yu, G., et al., *Polyrotaxane-based supramolecular theranostics*. *Nature Communications*, 2018. **9**(1): p. 766-799.
  93. Doroudian, M., et al., *Nanotechnology based therapeutics for lung disease*. *Thorax*, 2019: p. thoraxjnl-2019-213037.
  94. Babu, A., et al., *Nanoparticle-Based Drug Delivery for Therapy of Lung Cancer: Progress and Challenges*. *Journal of Nanomaterials*, 2013. **2013**: p. 11.
  95. Brahmer, J.R., *Harnessing the Immune System for the Treatment of Non-Small-Cell Lung Cancer*. *Journal of Clinical Oncology*, 2013. **31**(8): p. 1021-1028.
  96. Mamo, T. and G.A. Poland, *Nanovaccinology: The next generation of vaccines meets 21st century materials science and engineering*. *Vaccine*, 2012. **30**(47): p. 6609-6611.
  97. Fujita, Y. and H. Taguchi, *Current status of multiple antigen-presenting peptide vaccine systems: Application of organic and inorganic nanoparticles*. *Chemistry Central Journal*, 2011. **5**: p. 48-48.
  98. Suzuki, H., et al., *Multiple therapeutic peptide vaccines consisting of combined novel cancer testis antigens and anti-angiogenic peptides for patients with non-small cell lung cancer*. *Journal of Translational Medicine*, 2013. **11**: p. 97-97.
  99. Mitchell, P., et al., *Tecemotide in unresectable stage III non-small-cell lung cancer in the phase III START study: updated overall survival and biomarker analyses*. *Annals of Oncology*, 2015. **26**(6): p. 1134-1142.
  100. Peng, G., et al., *Diagnosing lung cancer in exhaled breath using gold nanoparticles*. *Nature Nanotechnology*, 2009. **4**: p. 669-673
  101. Sakumura, Y., et al., *Diagnosis by Volatile Organic Compounds in Exhaled Breath from Lung Cancer Patients Using Support Vector Machine Algorithm*. *Sensors (Basel, Switzerland)*, 2017. **17**(2): p. 287-299.
  102. Chatterjee, S., M. Castro, and J.F. Feller, *An e-nose made of carbon nanotube based quantum resistive sensors for the detection of eighteen polar/nonpolar VOC biomarkers of lung cancer*. *Journal of Materials Chemistry B*, 2013. **1**(36): p. 4563-4575.
  103. Peng, G., et al., *Detection of lung, breast, colorectal, and prostate cancers from exhaled breath using a single array of nanosensors*. *British Journal of Cancer*, 2010. **103**(4): p. 542-551.

104. Fernandes, M.P., S. Venkatesh, and B.G. Sudarshan, *Early Detection of Lung Cancer Using Nano-Nose - A Review*. The Open Biomedical Engineering Journal, 2015. **9**: p. 228-233.
105. Nakhleh, M.K., et al., *Diagnosis and Classification of 17 Diseases from 1404 Subjects via Pattern Analysis of Exhaled Molecules*. ACS Nano, 2017. **11**(1): p. 112-125.
106. Kelkar, S.S. and T.M. Reineke, *Theranostics: Combining Imaging and Therapy*. Bioconjugate Chemistry, 2011. **22**(10): p. 1879-1903.
107. Zavaleta, C., D. Ho, and E.J. Chung, *Theranostic Nanoparticles for Tracking and Monitoring Disease State*. SLAS TECHNOLOGY: Translating Life Sciences Innovation, 2018. **23**(3): p. 281-293.
108. Shi, J., et al., *Cancer nanomedicine: progress, challenges and opportunities*. Nature reviews. Cancer, 2017. **17**(1): p. 20-37.
109. Harrison, M., D. Tomlinson, and S. Stewart, *Liposomal-entrapped doxorubicin: an active agent in AIDS-related Kaposi's sarcoma*. Journal of Clinical Oncology, 1995. **13**(4): p. 914-920.
110. Meng, Z., et al., *Prodrug Strategies for Paclitaxel*. International Journal of Molecular Sciences, 2016. **17**(5): p. 796.
111. Zhang, Y., Y. Huang, and S. Li, *Polymeric Micelles: Nanocarriers for Cancer-Targeted Drug Delivery*. AAPS PharmSciTech, 2014. **15**(4): p. 862-871.
112. *FDA Approval for Paclitaxel Albumin-stabilized Nanoparticle Formulation USA*. 2018]; Available from: <https://www.cancer.gov/about-cancer/treatment/drugs/fda-nanoparticle-paclitaxel#Anchor-NSCLC>.
113. Hassan, S., et al., *Evolution and Clinical Translation of Drug Delivery Nanomaterials*. Nano today, 2017. **15**: p. 91-106.
114. Ragelle, H., et al., *Nanoparticle-based drug delivery systems: a commercial and regulatory outlook as the field matures*. Expert Opinion on Drug Delivery, 2017. **14**(7): p. 851-864.
115. Venditto, V.J. and F.C. Szoka, *Cancer Nanomedicines: So Many Papers and So Few Drugs!* Advanced drug delivery reviews, 2013. **65**(1): p. 80-88.
116. Kalepu, S. and V. Nekkanti, *Insoluble drug delivery strategies: review of recent advances and business prospects*. Acta Pharmaceutica Sinica B, 2015. **5**(5): p. 442-453.
117. Turner, C., et al., *Implications of the solvent vehicles dimethylformamide and dimethylsulfoxide for establishing transcriptomic endpoints in the zebrafish embryo toxicity test*. Environmental Toxicology and Chemistry, 2012. **31**(3): p. 593-604.
118. Jahangirian, H., et al., *A review of drug delivery systems based on nanotechnology and green chemistry: green nanomedicine*. International Journal of Nanomedicine, 2017. **12**: p. 2957-2978.
119. Zhu, X., et al., *Long-circulating siRNA nanoparticles for validating Prohibitin1-targeted non-small cell lung cancer treatment*. Proceedings of the National Academy of Sciences of the United States of America, 2015. **112**(25): p. 7779-7784.

120. Reid, G., et al., *Clinical development of TargomiRs, a miRNA mimic-based treatment for patients with recurrent thoracic cancer*. Epigenomics, 2016. **8**(8): p. 1079-1085.
121. Ensign, L.M., R. Cone, and J. Hanes, *Oral drug delivery with polymeric nanoparticles: The gastrointestinal mucus barriers*. Advanced Drug Delivery Reviews, 2012. **64**(6): p. 557-570.
122. Ngwa, W., et al., *Nanoparticle Drones to Target Lung Cancer with Radiosensitizers and Cannabinoids*. Frontiers in Oncology, 2017. **7**: p. 208-215.
123. Chidambaram M, M.R., Kathiresan K, *Nanotherapeutics to overcome conventional cancer chemotherapy limitations*. Journal of Pharmacy and Pharmaceutical Sciences, 2011. **14**(1): p. 67-77.
124. Loira-Pastoriza, C., J. Todoroff, and R. Vanbever, *Delivery strategies for sustained drug release in the lungs*. Advanced Drug Delivery Reviews, 2014. **75**: p. 81-91.
125. Mangal, S., et al., *Pulmonary delivery of nanoparticle chemotherapy for the treatment of lung cancers: challenges and opportunities*. Acta Pharmacologica Sinica, 2017. **38**(6): p. 782-797.
126. Masood, F., *Polymeric nanoparticles for targeted drug delivery system for cancer therapy*. Materials Science and Engineering: C, 2016. **60**: p. 569-578.
127. Seidi, K., et al., *Tumor target amplification: Implications for nano drug delivery systems*. Journal of Controlled Release, 2018. **275**: p. 142-161.
128. Srinivasarao, M. and P.S. Low, *Ligand-Targeted Drug Delivery*. Chemical Reviews, 2017. **117**(19): p. 12133-12164.
129. Hare, J.I., et al., *Challenges and strategies in anti-cancer nanomedicine development: An industry perspective*. Advanced Drug Delivery Reviews, 2017. **108**: p. 25-38.
130. Zhu, Y.-J. and F. Chen, *pH-Responsive Drug-Delivery Systems*. Chemistry – An Asian Journal, 2015. **10**(2): p. 284-305.
131. Gandhi, A., et al., *Studies on thermoresponsive polymers: Phase behaviour, drug delivery and biomedical applications*. Asian Journal of Pharmaceutical Sciences, 2015. **10**(2): p. 99-107.
132. Raza, A., et al., *Redox-responsive nano-carriers as tumor-targeted drug delivery systems*. European Journal of Medicinal Chemistry, 2018. **157**: p. 705-715.
133. Zhou, Y., et al., *Photoresponsive Drug/Gene Delivery Systems*. Biomacromolecules, 2018. **19**(6): p. 1840-1857.
134. Nappini, S., et al., *Magnetic field responsive drug release from magnetoliposomes in biological fluids*. Journal of Materials Chemistry B, 2016. **4**(4): p. 716-725.
135. Banik, B.L., P. Fattahi, and J.L. Brown, *Polymeric nanoparticles: the future of nanomedicine*. Wiley Interdisciplinary Reviews: Nanomedicine and Nanobiotechnology, 2016. **8**(2): p. 271-299.

136. Delplace, V., P. Couvreur, and J. Nicolas, *Recent trends in the design of anticancer polymer prodrug nanocarriers*. *Polymer Chemistry*, 2014. **5**(5): p. 1529-1544.
137. Kamaly, N., et al., *Targeted polymeric therapeutic nanoparticles: design, development and clinical translation*. *Chemical Society reviews*, 2012. **41**(7): p. 2971-3010.
138. Yang, Y., et al., *Safety and efficacy of PLGA(Ag-Fe(3)O(4))-coated dental implants in inhibiting bacteria adherence and osteogenic inducement under a magnetic field*. *International journal of nanomedicine*, 2018. **13**: p. 3751-3762.
139. Prabhu, R.H., V.B. Patravale, and M.D. Joshi, *Polymeric nanoparticles for targeted treatment in oncology: current insights*. *International Journal of Nanomedicine*, 2015. **10**: p. 1001-1018.
140. Weissig, V., T.K. Pettinger, and N. Murdock, *Nanopharmaceuticals (part 1): products on the market*. *International Journal of Nanomedicine*, 2014. **9**: p. 4357-4373.
141. Kamaly, N., et al., *Degradable Controlled-Release Polymers and Polymeric Nanoparticles: Mechanisms of Controlling Drug Release*. *Chemical reviews*, 2016. **116**(4): p. 2602-2663.
142. Hamid Akash, M.S., K. Rehman, and S. Chen, *Natural and Synthetic Polymers as Drug Carriers for Delivery of Therapeutic Proteins*. *Polymer Reviews*, 2015. **55**(3): p. 371-406.
143. Vroman, I. and L. Tighzert, *Biodegradable Polymers*. *Materials*, 2009. **2**(2): p. 307-344.
144. Makadia, H.K. and S.J. Siegel, *Poly Lactic-co-Glycolic Acid (PLGA) as Biodegradable Controlled Drug Delivery Carrier*. *Polymers*, 2011. **3**(3): p. 1377-1397.
145. Hudson, D. and A. Margaritis, *Biopolymer nanoparticle production for controlled release of biopharmaceuticals*. *Critical Reviews in Biotechnology*, 2014. **34**(2): p. 161-179.
146. Khan, I., et al., *PLGA Nanoparticles and Their Versatile Role in Anticancer Drug Delivery*. 2016. **33**(2): p. 159-193.
147. Mohammadi-Samani, S. and B. Taghipour, *PLGA micro and nanoparticles in delivery of peptides and proteins; problems and approaches*. *Pharmaceutical Development and Technology*, 2015. **20**(4): p. 385-393.
148. Zununi Vahed, S., et al., *Targeted cancer drug delivery with aptamer-functionalized polymeric nanoparticles*. *Journal of Drug Targeting*, 2018: p. 1-8.
149. Kitchell, J.P. and D.L. Wise, *Poly(lactic/glycolic acid) biodegradable drug—polymer matrix systems*, in *Methods in Enzymology*. 1985, Academic Press. p. 436-448.
150. Chung, T.-W., et al., *Different ratios of lactide and glycolide in PLGA affect the surface property and protein delivery characteristics of the PLGA microspheres with hydrophobic additives*. *Journal of Microencapsulation*, 2006. **23**(1): p. 15-27.

151. Prakapenka, A.V., H.A. Bimonte-Nelson, and R.W. Sirianni, *Engineering poly(lactic-co-glycolic acid) (PLGA) micro- and nano-carriers for Controlled Delivery of 17 $\beta$ -Estradiol*. *Annals of biomedical engineering*, 2017. **45**(7): p. 1697-1709.
152. Klose, D., et al., *PLGA-based drug delivery systems: Importance of the type of drug and device geometry*. *International Journal of Pharmaceutics*, 2008. **354**(1): p. 95-103.
153. Gentile, P., et al., *An overview of poly(lactic-co-glycolic) acid (PLGA)-based biomaterials for bone tissue engineering*. *International journal of molecular sciences*, 2014. **15**(3): p. 3640-3659.
154. Babu, A., et al., *Chemodrug delivery using integrin-targeted PLGA-Chitosan nanoparticle for lung cancer therapy*. *Scientific reports*, 2017. **7**(1): p. 14674-14674.
155. He, Z., et al., *Co-delivery of cisplatin and paclitaxel by folic acid conjugated amphiphilic PEG-PLGA copolymer nanoparticles for the treatment of non-small lung cancer*. *Oncotarget*, 2015. **6**(39): p. 42150-42168.
156. Menon, J.U., et al., *Dual-Drug Containing Core-Shell Nanoparticles for Lung Cancer Therapy*. *Scientific reports*, 2017. **7**(1): p. 13249-13249.
157. Wang, X., et al., *Efficient lung cancer-targeted drug delivery via a nanoparticle/MS system*. *Acta Pharmaceutica Sinica B*, 2018. **9**(1): p. 167-176.
158. Ayalasonmayajula, S.P. and U.B. Kompella, *Subconjunctivally administered celecoxib-PLGA microparticles sustain retinal drug levels and alleviate diabetes-induced oxidative stress in a rat model*. *European Journal of Pharmacology*, 2005. **511**(2): p. 191-198.
159. Lü, J.-M., et al., *Current advances in research and clinical applications of PLGA-based nanotechnology*. *Expert review of molecular diagnostics*, 2009. **9**(4): p. 325-341.
160. Sun, X., et al., *Poly(Lactic-co-Glycolic Acid): Applications and Future Prospects for Periodontal Tissue Regeneration*. *Polymers*, 2017. **9**(6): p. 189-208.
161. Kuzmov, A. and T. Minko, *Nanotechnology approaches for inhalation treatment of lung diseases*. *Journal of Controlled Release*, 2015. **219**: p. 500-518.
162. Reed, M.D., et al., *Aerosolised 5-azacytidine suppresses tumour growth and reprogrammes the epigenome in an orthotopic lung cancer model*. *British Journal Of Cancer*, 2013. **109**(7): p. 1775–1781.
163. Carvalho, T.C., S.R. Carvalho, and J.T. McConville, *Formulations for Pulmonary Administration of Anticancer Agents to Treat Lung Malignancies*. *Journal of Aerosol Medicine and Pulmonary Drug Delivery*, 2011. **24**(2): p. 61-80.
164. Ajay, G. and K. Nadezhda, *Paclitaxel (Taxol) and Taxoid Derivates for Lung Cancer Treatment: Potential for Aerosol Delivery*. *Current Cancer Drug Targets*, 2003. **3**(4): p. 287-296.

165. Lee, W.-H., et al., *Inhalation of nanoparticle-based drug for lung cancer treatment: Advantages and challenges*. Asian Journal of Pharmaceutical Sciences, 2015. **10**(6): p. 481-489.
166. Ungaro, F., et al., *Engineered PLGA nano- and micro-carriers for pulmonary delivery: challenges and promises*. Journal of Pharmacy and Pharmacology, 2012. **64**(9): p. 1217-1235.
167. d'Angelo, I., F. Quaglia, and F. Ungaro, *PLGA carriers for inhalation: where do we stand, where are we headed?* Therapeutic Delivery, 2015. **6**(10): p. 1139-1144.
168. Ungaro, F., et al., *Dry powders based on PLGA nanoparticles for pulmonary delivery of antibiotics: Modulation of encapsulation efficiency, release rate and lung deposition pattern by hydrophilic polymers*. Journal of Controlled Release, 2012. **157**(1): p. 149-159.
169. Tomoda, K., et al., *Preparation and properties of inhalable nanocomposite particles for treatment of lung cancer*. Colloids and Surfaces B: Biointerfaces, 2009. **71**(2): p. 177-182.
170. Qiao, J.-B., et al., *Aerosol delivery of biocompatible dihydroergotamine-loaded PLGA-PSPE polymeric micelles for efficient lung cancer therapy*. Polymer Chemistry, 2017. **8**(9): p. 1540-1554.
171. Moura, C.C., et al., *Co-association of methotrexate and SPIONs into anti-CD64 antibody-conjugated PLGA nanoparticles for theranostic application*. International Journal of Nanomedicine, 2014. **9**: p. 4911-4922.
172. Margareth R. C. Marques, R.L., May Almukainzi, *Simulated biological fluids with possible application in dissolution testing*. Dissolution Technologies, 2011. **18**(3): p. 15-28.
173. Dhand, C., et al., *Methods and strategies for the synthesis of diverse nanoparticles and their applications: a comprehensive overview*. RSC Advances, 2015. **5**(127): p. 105003-105037.
174. Wong, T.-S., B. Brough, and C.-M. Ho, *Creation of functional micro/nano systems through top-down and bottom-up approaches*. Molecular & cellular biomechanics : MCB, 2009. **6**(1): p. 1-55.
175. Resham, C., T. Giovanni, and M.G. Andreas, *Emerging Use of Nanotechnology in the Treatment of Neurological Disorders*. Current Pharmaceutical Design, 2015. **21**(22): p. 3111-3130.
176. Yu, H.-D., et al., *Chemical routes to top-down nanofabrication*. Chemical Society Reviews, 2013. **42**(14): p. 6006-6018.
177. Khanna, V.K., *Bottom-up Nanofabrication*, in *Integrated Nanoelectronics: Nanoscale CMOS, Post-CMOS and Allied Nanotechnologies*. 2016, Springer India: New Delhi. p. 397-417.
178. Alshamsan, A., *Nanoprecipitation is more efficient than emulsion solvent evaporation method to encapsulate cucurbitacin I in PLGA nanoparticles*. Saudi pharmaceutical journal : SPJ : the official publication of the Saudi Pharmaceutical Society, 2014. **22**(3): p. 219-222.
179. Xu, Q., et al., *Scalable method to produce biodegradable nanoparticles that rapidly penetrate human mucus*. Journal of controlled release : JCR, 2014. **193**: p. 1-10.

- official journal of the Controlled Release Society, 2013. **170**(2): p. 279-286.
180. Maria, G.N.-A., et al., *Single Emulsion-Solvent Evaporation Technique and Modifications for the Preparation of Pharmaceutical Polymeric Nanoparticles*. Recent Patents on Drug Delivery & Formulation, 2012. **6**(3): p. 209-223.
  181. Schmitz-Antoniak, C., *X-ray absorption spectroscopy on magnetic nanoscale systems for modern applications*. Reports on Progress in Physics, 2015. **78**(6).
  182. Li, Y. and D. Boraschi, *Endotoxin contamination: a key element in the interpretation of nanosafety studies*. Nanomedicine, 2016. **11**(3): p. 269-287.
  183. Li, Y., M. Fujita, and D. Boraschi, *Endotoxin Contamination in Nanomaterials Leads to the Misinterpretation of Immunosafety Results*. Frontiers in immunology, 2017. **8**: p. 472-472.
  184. Li, Y., et al., *Bacterial endotoxin (lipopolysaccharide) binds to the surface of gold nanoparticles, interferes with biocorona formation and induces human monocyte inflammatory activation*. Nanotoxicology, 2017. **11**(9-10): p. 1157-1175.
  185. Gorbet, M.B. and M.V. Sefton, *Endotoxin: The uninvited guest*. Biomaterials, 2005. **26**(34): p. 6811-6817.
  186. Unger, R.E., et al., *Human endothelial cell-based assay for endotoxin as sensitive as the conventional Limulus Amebocyte Lysate assay*. Biomaterials, 2014. **35**(10): p. 3180-3187.
  187. Yaneva, Z. and N. Georgieva, *Chapter 5 - Physicochemical and morphological characterization of pharmaceutical nanocarriers and mathematical modeling of drug encapsulation/release mass transfer processes*, in *Nanoscale Fabrication, Optimization, Scale-Up and Biological Aspects of Pharmaceutical Nanotechnology*, A.M. Grumezescu, Editor. 2018, William Andrew Publishing. p. 173-218.
  188. Danaei, M., et al., *Impact of Particle Size and Polydispersity Index on the Clinical Applications of Lipidic Nanocarrier Systems*. Pharmaceutics, 2018. **10**(2): p. 57-75.
  189. Filipe, V., A. Hawe, and W. Jiskoot, *Critical evaluation of Nanoparticle Tracking Analysis (NTA) by NanoSight for the measurement of nanoparticles and protein aggregates*. Pharmaceutical research, 2010. **27**(5): p. 796-810.
  190. Menon, J.U., et al., *Polymeric nanoparticles for pulmonary protein and DNA delivery*. Acta biomaterialia, 2014. **10**(6): p. 2643-2652.
  191. Athanasiou, K.A., G.G. Niederauer, and C.M. Agrawal, *Sterilization, toxicity, biocompatibility and clinical applications of polylactic acid/polyglycolic acid copolymers*. Biomaterials, 1996. **17**(2): p. 93-102.
  192. Hillegass, J.M., et al., *Assessing nanotoxicity in cells in vitro*. Wiley interdisciplinary reviews. Nanomedicine and nanobiotechnology, 2010. **2**(3): p. 219-231.

193. Jan, E., et al., *High-Content Screening as a Universal Tool for Fingerprinting of Cytotoxicity of Nanoparticles*. ACS Nano, 2008. **2**(5): p. 928-938.
194. Foroozandeh, P. and A.A. Aziz, *Insight into Cellular Uptake and Intracellular Trafficking of Nanoparticles*. Nanoscale research letters, 2018. **13**(1): p. 339-339.
195. Gobbo, O.L., et al., *Magnetic Nanoparticles in Cancer Theranostics*. Theranostics, 2015. **5**(11): p. 1249-1263.
196. Rezvantab, S., et al., *PLGA-Based Nanoparticles in Cancer Treatment*. Frontiers in pharmacology, 2018. **9**: p. 1260-1260.
197. Sharma, N., P. Madan, and S. Lin, *Effect of process and formulation variables on the preparation of parenteral paclitaxel-loaded biodegradable polymeric nanoparticles: A co-surfactant study*. Asian Journal of Pharmaceutical Sciences, 2016. **11**(3): p. 404-416.
198. Jelvehgari, M., et al., *Fabrication and in vitro evaluation of Ketotifen Fumarate-loaded PLGA nanoparticles as a sustained delivery system*. Iranian Journal of Pharmaceutical Research, 2017. **16**(1): p. 22-34.
199. Madani, F., et al., *Investigation of Effective Parameters on Size of Paclitaxel Loaded PLGA Nanoparticles*. Adv Pharm Bull, 2018. **8**(1): p. 77-84.
200. Park, K., *Facing the truth about nanotechnology in drug delivery*. ACS nano, 2013. **7**(9): p. 7442-7447.
201. Potenza, M.A.C., et al., *Single particle optical extinction and scattering allows real time quantitative characterization of drug payload and degradation of polymeric nanoparticles*. Scientific reports, 2015. **5**: p. 18228-18228.
202. Ramalho, M.J. and M.C. Pereira, *Preparation and Characterization of Polymeric Nanoparticles: An Interdisciplinary Experiment*. Journal of Chemical Education, 2016. **93**(8): p. 1446-1451.
203. Ling, Y., et al., *Dual docetaxel/superparamagnetic iron oxide loaded nanoparticles for both targeting magnetic resonance imaging and cancer therapy*. Biomaterials, 2011. **32**(29): p. 7139-7150.
204. Fernández Fernández, E., et al., *Biopolymer-Based Nanoparticles for Cystic Fibrosis Lung Gene Therapy Studies*. Materials, 2018. **11**(1): p. 122-137.
205. Lopalco, A., et al., *Oxcarbazepine-loaded polymeric nanoparticles: development and permeability studies across in vitro models of the blood-brain barrier and human placental trophoblast*. International journal of nanomedicine, 2015. **10**: p. 1985-1996.
206. *Zeta Potential Analysis of Nanoparticles*. 2012 [cited 2019; Available from: [https://cdn.shopify.com/s/files/1/0257/8237/files/nanoComposix\\_Guidelines\\_for\\_Zeta\\_Potential\\_Analysis\\_of\\_Nanoparticles.pdf](https://cdn.shopify.com/s/files/1/0257/8237/files/nanoComposix_Guidelines_for_Zeta_Potential_Analysis_of_Nanoparticles.pdf)].
207. Hsu, M.N., et al., *Sustained release of hydrophobic drugs by the microfluidic assembly of multistage microgel/poly (lactic-co-glycolic acid) nanoparticle composites*. Biomicrofluidics, 2015. **9**(5): p. 052601-052601.

208. Kohane, D.S., *Microparticles and nanoparticles for drug delivery*. Biotechnology and Bioengineering, 2007. **96**(2): p. 203-209.
209. Bazile, D.V., et al., *Body distribution of fully biodegradable [14C]-poly(lactic acid) nanoparticles coated with albumin after parenteral administration to rats*. Biomaterials, 1992. **13**(15): p. 1093-1102.
210. Lu, Y.-C., W.-C. Yeh, and P.S. Ohashi, *LPS/TLR4 signal transduction pathway*. Cytokine, 2008. **42**(2): p. 145-151.
211. Alexander C, R.E., *Bacterial lipopolysaccharides and innate immunity*. Journal of Endotoxin Research 2001. **7**(3): p. 167-202.
212. Parrillo, J.E., *Pathogenetic Mechanisms of Septic Shock*. New England Journal of Medicine, 1993. **328**(20): p. 1471-1477.
213. FDA. *Guidance for Industry Pyrogen and Endotoxins Testing: Questions and Answers*. 2012 [cited 2018; Available from: <https://www.gmp-compliance.org/gmp-news/fda-publishes-q-a-guidance-on-endotoxin-and-pyrogen-testing>.
214. Mohamed, B.M., et al., *Activation of stress-related signalling pathway in human cells upon SiO<sub>2</sub> nanoparticles exposure as an early indicator of cytotoxicity*. Journal of Nanobiotechnology, 2011. **9**(1): p. 29-43.
215. Movia, D., et al., *Screening the Cytotoxicity of Single-Walled Carbon Nanotubes Using Novel 3D Tissue-Mimetic Models*. ACS Nano, 2011. **5**(11): p. 9278-9290.
216. MANDELKOW, R., et al., *Detection and Quantification of Nuclear Morphology Changes in Apoptotic Cells by Fluorescence Microscopy and Subsequent Analysis of Visualized Fluorescent Signals*. Anticancer Research, 2017. **37**(5): p. 2239-2244.
217. Johnson, V.L., et al., *Effector caspases are dispensable for the early nuclear morphological changes during chemical-induced apoptosis*. Journal of Cell Science, 2000. **113**(17): p. 2941-53.
218. Guggenheim, E.J., et al., *Comparison of Confocal and Super-Resolution Reflectance Imaging of Metal Oxide Nanoparticles*. PloS one, 2016. **11**(10): p. e0159980-e0159980.
219. Tong, L., et al., *Synthesis and application of superparamagnetic iron oxide nanoparticles in targeted therapy and imaging of cancer*. Frontiers of Medicine, 2011. **5**(4): p. 379-387.
220. Calero, M., et al., *Characterization of interaction of magnetic nanoparticles with breast cancer cells*. Journal of Nanobiotechnology, 2015. **13**(1): p. 1-15.
221. Grabowski, N., et al., *Toxicity of surface-modified PLGA nanoparticles toward lung alveolar epithelial cells*. International Journal of Pharmaceutics, 2013. **454**(2): p. 686-694.
222. Gao, W., et al., *Nanoparticle-based local antimicrobial drug delivery*. Advanced Drug Delivery Reviews, 2018. **127**: p. 46-57.
223. Mansour, H.M., Y.-S. Rhee, and X. Wu, *Nanomedicine in pulmonary delivery*. International journal of nanomedicine, 2009. **4**: p. 299-319.

224. Lin, X., et al., *Promote potential applications of nanoparticles as respiratory drug carrier: insights from molecular dynamics simulations*. *Nanoscale*, 2014. **6**(5): p. 2759-2767.
225. Agu, R.U., et al., *The lung as a route for systemic delivery of therapeutic proteins and peptides*. *Respiratory research*, 2001. **2**(4): p. 198-209.
226. Danhier, F., et al., *PLGA-based nanoparticles: An overview of biomedical applications*. *Journal of Controlled Release*, 2012. **161**(2): p. 505-522.
227. Pritchard, J.N., et al., *Mesh nebulizers have become the first choice for new nebulized pharmaceutical drug developments*. *Therapeutic Delivery*, 2018. **9**(2): p. 121-136.
228. [cited 2019; Available from: <https://www.aerogen.com/aerogen-solo-3/>.
229. Awad, S., S.P. Allison, and D.N. Lobo, *The history of 0.9% saline*. *Clinical Nutrition*, 2008. **27**(2): p. 179-188.
230. Dentice, R.L., M.R. Elkins, and P.T.P. Bye, *Adults with cystic fibrosis prefer hypertonic saline before or during airway clearance techniques: a randomised crossover trial*. *Journal of Physiotherapy*, 2012. **58**(1): p. 33-40.
231. Zhou, Q., et al., *Emerging inhalation aerosol devices and strategies: Where are we headed?* *Advanced Drug Delivery Reviews*, 2014. **75**: p. 3-17.
232. Alfredo, G.-A., *A European Perspective on Orally Inhaled Products: In Vitro Requirements for a Biowaiver*. *Journal of Aerosol Medicine and Pulmonary Drug Delivery*, 2014. **27**(6): p. 419-429.
233. Lu, D., et al., *International Guidelines for Bioequivalence of Locally Acting Orally Inhaled Drug Products: Similarities and Differences*. *The AAPS journal*, 2015. **17**(3): p. 546-557.
234. Mohan, M., et al., *Evaluation of Abbreviated Impactor Measurements (AIM) and Efficient Data Analysis (EDA) for Dry Powder Inhalers (DPIs) Against the Full-Resolution Next Generation Impactor (NGI)*. *AAPS PharmSciTech*, 2017. **18**(5): p. 1585-1594.
235. Marple, V.A., et al., *Next Generation Pharmaceutical Impactor (A New Impactor for Pharmaceutical Inhaler Testing). Part I: Design*. *Journal of Aerosol Medicine*, 2003. **16**(3): p. 283-299.
236. Abdelrahim, M.E. and H. Chrystyn, *Aerodynamic Characteristics of Nebulized Terbutaline Sulphate Using the Next Generation Impactor (NGI) and CEN Method*. *Journal of Aerosol Medicine and Pulmonary Drug Delivery*, 2009. **22**(1): p. 19-28.
237. *Inhalation and nasal drug products: Aerosols, sprays, and powders-performance quality tests*. [cited 2019; Available from: [https://www.drugfuture.com/Pharmacopoeia/usp38/data/v38332/usp38nf33s2\\_c601.html](https://www.drugfuture.com/Pharmacopoeia/usp38/data/v38332/usp38nf33s2_c601.html).
238. Varshosaz, J., et al., *Development of dry powder inhaler containing tadalafil-loaded PLGA nanoparticles*. *Research in pharmaceutical sciences*, 2017. **12**(3): p. 222-232.
239. Said-Elbahr, R., et al., *Nebulizable colloidal nanoparticles co-encapsulating a COX-2 inhibitor and a herbal compound for treatment of*

- lung cancer*. European Journal of Pharmaceutics and Biopharmaceutics, 2016. **103**: p. 1-12.
240. Selvam, P., I.M. El-Sherbiny, and H.D.C. Smyth, *Swellable Hydrogel Particles for Controlled Release Pulmonary Administration Using Propellant-Driven Metered Dose Inhalers*. Journal of Aerosol Medicine and Pulmonary Drug Delivery, 2011. **24**(1): p. 25-34.
241. Patton, J.S. and P.R. Byron, *Inhaling medicines: delivering drugs to the body through the lungs*. Nature Reviews Drug Discovery, 2007. **6**: p. 67.
242. Song, X., et al., *Effects of Temperature and Humidity on Laser Diffraction Measurements to Jet Nebulizer and Comparison with NGI*. AAPS PharmSciTech, 2015. **17**(2): p. 380-388.
243. Salt, K., C.A. Noble, and K.A. Prather, *Aerodynamic Particle Sizing versus Light Scattering Intensity Measurement as Methods for Real-Time Particle Sizing Coupled with Time-of-Flight Mass Spectrometry*. Analytical Chemistry, 1996. **68**(1): p. 230-234.
244. Totoki, S., et al., *Quantitative laser diffraction method for the assessment of protein subvisible particles*. Journal of pharmaceutical sciences, 2015. **104**(2): p. 618-626.
245. *Laser Diffraction (LD)*. [cited 2019; Available from: <https://www.malvernpanalytical.com/en/products/technology/light-scattering/laser-diffraction>].
246. Forbes, B., et al., *In Vitro Testing for Orally Inhaled Products: Developments in Science-Based Regulatory Approaches*. The AAPS journal, 2015. **17**(4): p. 837-852.
247. Costa, R., et al., *Influence of ventilator settings on patient-ventilator synchrony during pressure support ventilation with different interfaces*. Intensive Care Medicine, 2010. **36**(8): p. 1363-1370.
248. Kacmarek, R.M., *The Mechanical Ventilator: Past, Present, and Future*. Respiratory Care, 2011. **56**(8): p. 1170-80.
249. Dugernier, J., et al., *Aerosol delivery with two ventilation modes during mechanical ventilation: a randomized study*. Annals of intensive care, 2016. **6**(1): p. 73-73.
250. Dugernier, J., et al., *SPECT-CT Comparison of Lung Deposition using a System combining a Vibrating-mesh Nebulizer with a Valved Holding Chamber and a Conventional Jet Nebulizer: a Randomized Cross-over Study*. Pharmaceutical Research, 2017. **34**(2): p. 290-300.
251. Esquisabel, A., et al., *Pulmonary drug delivery: a review on nanocarriers for antibacterial chemotherapy*. Journal of Antimicrobial Chemotherapy, 2015. **70**(11): p. 2945-2955.
252. Chan, J.G.Y., et al., *Advances in device and formulation technologies for pulmonary drug delivery*. AAPS PharmSciTech, 2014. **15**(4): p. 882-897.
253. Zhou, Q., et al., *Inhaled formulations and pulmonary drug delivery systems for respiratory infections*. Advanced Drug Delivery Reviews, 2015. **85**: p. 83-99.
254. Arzu, A., et al., *Performance Comparisons of Jet and Mesh Nebulizers Using Different Interfaces in Simulated Spontaneously Breathing Adults*

- and Children. Journal of Aerosol Medicine and Pulmonary Drug Delivery*, 2015. **28**(4): p. 281-289.
255. Fink, J.B., *Aerosol therapy in children: challenges and solutions AU - Ari, Arzu. Expert Review of Respiratory Medicine*, 2013. **7**(6): p. 665-672.
  256. Dolovich, M.B. and R. Dhand, *Aerosol drug delivery: developments in device design and clinical use. The Lancet*, 2011. **377**(9770): p. 1032-1045.
  257. Ari, A. and R.D. Restrepo, *Aerosol Delivery Device Selection for Spontaneously Breathing Patients: 2012. Respiratory Care*, 2012. **57**(4): p. 613-626.
  258. Fink, J.B., *Guidelines for aerosol devices in infants, children and adults: which to choose, why and how to achieve effective aerosol therapy AU - Ari, Arzu. Expert Review of Respiratory Medicine*, 2011. **5**(4): p. 561-572.
  259. Waldrep, J.C. and R. Dhand, *Advanced Nebulizer Designs Employing Vibrating Mesh/Aperture Plate Technologies for Aerosol Generation. Current Drug Delivery*, 2008. **5**(2): p. 114-119.
  260. Ari, A., *Jet, Ultrasonic, and Mesh Nebulizers: An Evaluation of Nebulizers for Better Clinical Outcomes. Eurasian Journal of Pulmonology*, 2014. **16**: p. 16: 1-7.
  261. Labiris, N.R. and M.B. Dolovich, *Pulmonary drug delivery. Part I: physiological factors affecting therapeutic effectiveness of aerosolized medications. British journal of clinical pharmacology*, 2003. **56**(6): p. 588-599.
  262. Dugernier, J., et al., *Aerosol delivery during invasive mechanical ventilation: a systematic review. Critical care (London, England)*, 2017. **21**(1): p. 264-264.
  263. Kok, T., et al., *Small-molecule inhibitors of macrophage migration inhibitory factor (MIF) as an emerging class of therapeutics for immune disorders. Drug Discovery Today*, 2018. **23**(11): p. 1910-1918.
  264. Howard, B.A., et al., *Translating biomarkers into clinical practice: prognostic implications of cyclophilin A and macrophage migratory inhibitory factor identified from protein expression profiles in non-small cell lung cancer. Lung Cancer*, 2004. **46**(3): p. 313-323.
  265. Xu, L., et al., *Current developments of macrophage migration inhibitory factor (MIF) inhibitors. Drug Discovery Today*, 2013. **18**(11): p. 592-600.
  266. Janos, G. and L. Tamas, *Macrophage Migration Inhibitory Factor (MIF) Tautomerase Inhibitors as Potential Novel Anti-Inflammatory Agents: Current Developments. Current Medicinal Chemistry*, 2009. **16**(9): p. 1091-1114.
  267. Wang, C., et al., *Macrophage migration inhibitory factor promotes osteosarcoma growth and lung metastasis through activating the RAS/MAPK pathway. Cancer Letters*, 2017. **403**: p. 271-279.
  268. Guo, Y., et al., *Functional disruption of macrophage migration inhibitory factor (MIF) suppresses proliferation of human H460 lung cancer cells by caspase-dependent apoptosis. Cancer cell international*, 2013. **13**(1): p. 28-28.

269. Zhang, B., et al., *Role of Macrophage Migration Inhibitory Factor in the Proliferation of Smooth Muscle Cell in Pulmonary Hypertension*. *Mediators of Inflammation*, 2012. **2012**: p. 1-10.
270. Ioannou, K., et al., *ISO-66, a novel inhibitor of macrophage migration, shows efficacy in melanoma and colon cancer models*. *International journal of oncology*, 2014. **45**(4): p. 1457-1468.
271. Zapatero, M.C., et al., *Discovery of Novel Inhibitors of the Tautomerase Activity of Macrophage Migration Inhibitory Factor (MIF)*. *Journal of Biomolecular Screening*, 2016. **21**(5): p. 446-458.
272. Rajasekaran, D., et al., *Targeting distinct tautomerase sites of D-DT and MIF with a single molecule for inhibition of neutrophil lung recruitment*. *FASEB journal : official publication of the Federation of American Societies for Experimental Biology*, 2014. **28**(11): p. 4961-4971.
273. Marte, B., *Cell division and cancer*. *Nature*, 2004. **432**: p. 293.
274. Lan, H., et al., *Macrophage migration inhibitory factor (MIF) promotes rat airway muscle cell proliferation and migration mediated by ERK1/2 and FAK signaling*. *Cell Biology International*, 2018. **42**(1): p. 75-83.
275. Cui, J., et al., *Macrophage migration inhibitory factor promotes cardiac stem cell proliferation and endothelial differentiation through the activation of the PI3K/Akt/mTOR and AMPK pathways*. *International journal of molecular medicine*, 2016. **37**(5): p. 1299-1309.
276. Zhang, Y., et al., *Macrophage migration inhibitory factor mediates hypoxia-induced pulmonary hypertension*. *Molecular medicine (Cambridge, Mass.)*, 2011. **18**(1): p. 215-223.
277. Tan, W., et al., *Inhibition of human lung H460 cell proliferation by siRNA-mediated macrophage migration inhibitory factor (MIF) blocking*. *European Respiratory Journal*, 2013. **42**(Suppl 57): p. P3113.
278. Simpson, K.D., D.J. Templeton, and J.V. Cross, *Macrophage Migration Inhibitory Factor Promotes Tumor Growth and Metastasis by Inducing Myeloid-Derived Suppressor Cells in the Tumor Microenvironment*. *The Journal of Immunology*, 2012. **189**(12): p. 5533-5540.
279. White, E.S., et al., *Macrophage Migration Inhibitory Factor and CXC Chemokine Expression in Non-Small Cell Lung Cancer. Role in Angiogenesis and Prognosis*, 2003. **9**(2): p. 853-860.
280. Lue, H., et al., *Rapid and transient activation of the ERK MAPK signalling pathway by macrophage migration inhibitory factor (MIF) and dependence on JAB1/CSN5 and Src kinase activity*. *Cellular Signalling*, 2006. **18**(5): p. 688-703.
281. Lue, H., et al., *Activation of the JNK signalling pathway by macrophage migration inhibitory factor (MIF) and dependence on CXCR4 and CD74*. *Cellular signalling*, 2011. **23**(1): p. 135-144.
282. Rosano, G.L. and E.A. Ceccarelli, *Recombinant protein expression in Escherichia coli: advances and challenges*. *Frontiers in microbiology*, 2014. **5**: p. 172-172.

283. Joseph, D., J.P. Gonsky, and S.W. Blain, *Macrophage Inhibitory Factor-1 (MIF-1) controls the plasticity of multiple myeloma tumor cells*. PLOS ONE, 2018. **13**(11): p. e0206368.
284. Tawadros, T., et al., *Release of macrophage migration inhibitory factor by neuroendocrine-differentiated LNCaP cells sustains the proliferation and survival of prostate cancer cells*. 2013. **20**(1): p. 137-186.
285. Djudjaj, S., et al., *Macrophage Migration Inhibitory Factor Mediates Proliferative GN via CD74*. Journal of the American Society of Nephrology : JASN, 2016. **27**(6): p. 1650-1664.
286. Al-Abed, Y. and S. VanPatten, *MIF as a disease target: ISO-1 as a proof-of-concept therapeutic*. Future Medicinal Chemistry, 2011. **3**(1): p. 45-63.
287. Ferlay, J., et al., *Estimating the global cancer incidence and mortality in 2018: GLOBOCAN sources and methods*. International Journal of Cancer, 2019. **144**(8): p. 1941-1953.
288. Uramoto, H. and F. Tanaka, *Recurrence after surgery in patients with NSCLC*. Translational lung cancer research, 2014. **3**(4): p. 242-249.
289. Trivedi-Parmar, V. and W.L. Jorgensen, *Advances and Insights for Small Molecule Inhibition of Macrophage Migration Inhibitory Factor*. Journal of Medicinal Chemistry, 2018. **61**(18): p. 8104-8119.
290. Cruzs, S.M. and F.R. Balkwill, *Inflammation and cancer: advances and new agents*. Nature Reviews Clinical Oncology, 2015. **12**(10): p. 584-96.
291. Simpson, K.D., D.J. Templeton, and J.V. Cross, *Macrophage migration inhibitory factor promotes tumor growth and metastasis by inducing myeloid-derived suppressor cells in the tumor microenvironment*. Journal of immunology (Baltimore, Md. : 1950), 2012. **189**(12): p. 5533-5540.
292. Wang, D., et al., *Upregulation of macrophage migration inhibitory factor promotes tumor metastasis and correlates with poor prognosis of pancreatic ductal adenocarcinoma*. Oncology reports, 2018. **40**(5): p. 2628-2636.
293. Fukaya, R., et al., *MIF Maintains the Tumorigenic Capacity of Brain Tumor-Initiating Cells by Directly Inhibiting p53*. Cancer Research, 2016. **76**(9): p. 2813-2823.
294. Fingerle-Rowson, G., et al., *The p53-dependent effects of macrophage migration inhibitory factor revealed by gene targeting*. Proceedings of the National Academy of Sciences of the United States of America, 2003. **100**(16): p. 9354-9359.
295. Zhang, Y., et al., *Inhibition of macrophage migration inhibitory factor (MIF) tautomerase activity suppresses microglia-mediated inflammatory responses*. Clinical and Experimental Pharmacology and Physiology, 2016. **43**(11): p. 1134-1144.
296. Lubetsky, J.B., et al., *The Tautomerase Active Site of Macrophage Migration Inhibitory Factor Is a Potential Target for Discovery of Novel Anti-inflammatory Agents*. Journal of Biological Chemistry, 2002. **277**(28): p. 24976-24982.
297. da Silva, A.L., et al., *New perspectives in nanotherapeutics for chronic respiratory diseases*. Biophysical reviews, 2017. **9**(5): p. 793-803.

298. Champion, J.A. and S. Mitragotri, *Role of target geometry in phagocytosis*. Proceedings of the National Academy of Sciences of the United States of America, 2006. **103**(13): p. 4930-4934.
299. Wu, L., J. Zhang, and W. Watanabe, *Physical and chemical stability of drug nanoparticles*. Advanced Drug Delivery Reviews, 2011. **63**(6): p. 456-469.
300. Biddiscombe, M.F. and O.S. Usmani, *Is there room for further innovation in inhaled therapy for airways disease?* Breathe (Sheffield, England), 2018. **14**(3): p. 216-224.
301. Meyer-Siegler, K.L., et al., *Macrophage migration inhibitory factor (MIF) gene polymorphisms are associated with increased prostate cancer incidence*. Genes And Immunity, 2007. **8**(8): p. 646-708.
302. Li, H., et al., *Gastric cancer susceptibility in gastric cancer relatives: Attributable risks of Macrophage migration inhibitory factor promoter polymorphism and Helicobacter pylori*. Cytokine, 2012. **60**(2): p. 346-351.
303. Castañeda-Moreno, V.A., et al., *MIF functional polymorphisms (-794 CATT5-8 and -173 G>C) are associated with MIF serum levels, severity and progression in male multiple sclerosis from western Mexican population*. Journal of Neuroimmunology, 2018. **320**: p. 117-124.
304. Wu, S., et al., *Macrophage migration inhibitory factor promoter polymorphisms (-794CATT5-7) as potential biomarker for early-stage cervical cancer*. Journal of Obstetrics and Gynaecology Research, 2017. **43**(3): p. 571-579.
305. Zhang, C., et al., *A functional macrophage migration inhibitory factor promoter polymorphism is associated with reduced diffusing capacity*. American Journal of Physiology-Lung Cellular and Molecular Physiology, 2019. **316**(2): p. L400-L405.
306. Mizue, Y., et al., *Role for macrophage migration inhibitory factor in asthma*. Proceedings of the National Academy of Sciences of the United States of America, 2005. **102**(40): p. 14410-14415.

## Appendix

- **Ampicillin sodium salt** (stock con. 50 mg/ml, working con. 50 µg/ml)
  1. Ampicillin (100 mg)
  2. dH<sub>2</sub>O (2 ml)
  3. Vortex 30 seconds
  4. filter (0.22 µm) under laminar hood and aliquate 100 µl in microtube
  5. Store -20°C/1 year or 4°C/3 months.
  
- **LB broth 1000 ml**
  1. LB broth (25 gr)
  2. dH<sub>2</sub>O 1000 ml
  3. Autoclave
  4. Cool medium to ~50°C add 1 ml Ampicillin 50 mg/ml
  5. Store 4°C
  
- **LB agar (1000 ml)**
  1. LB agar (40 g)
  2. dH<sub>2</sub>O (1000 ml) and heat to boiling
  3. Autoclave
  4. Cool medium to ~50°C add 1 ml Ampicillin (50 mg/ml)
  5. Aliquot 25 ml/ Petri dish
  6. 4 hours incubation in room temperature (RT)
  7. Cover by foil and store at 4°C
  
- **IPTG (100 mM)**
  1. IPTG (0.24 gr)
  2. dH<sub>2</sub>O (10 ml)
  3. filter sterilize (0.22 µm)
  4. Aliquots and store at -20°C for 4 months
  
- **TBE buffer (5X)**
  1. Tris base 32.4 g
  2. Boric acid 16.5 g
  3. EDTA 2.7 g
  4. H<sub>2</sub>O (300 ml)
  5. Adjust pH 8.0-8.5 (with NaOH)
  6. Adjust to 1000 ml
  
- **SDS PAGE running buffer (10X, 1 Lit)**
  1. SDS (10 g)
  2. Tris Base (30.30 g)
  3. Glycine (144 g)
  4. Adjust to 1000 ml
  5. Store at 4 °C

- **Fixation solution (500 ml)**
  1. dH<sub>2</sub>O (400 ml)
  2. Glacial Acetic acid 100 ml
  3. Methanol (500 ml)
  4. Store RT/ use before one month
  
- **Staining solution (1000 ml)**
  1. dH<sub>2</sub>O 450 ml
  2. Glacial Acetic acid (100 ml)
  3. Coomassie® Brilliant blue R 250 (3g)
  4. Methanol (450 ml)
  5. Filter the solution
  6. Store at RT
  
- **Destining solution (1000 ml)**
  1. dH<sub>2</sub>O 750 ml
  2. Methanol 150 ml
  3. Glacial Acetic acid 100 ml
  4. Store at RT and protect direct light
  
- **Glycerol Stock**
  1. Inoculate a single colony in medium with appropriate antibiotics
  2. Incubate at 37°C, shaker 200 rpm, overnight
  3. Overnight bacteria (0.8 ml) + sterile Glycerol (0.2 ml)
  4. Vortex vigorously
  5. Store at -80°C
  
- **HCl (4% solution)**
  1. dH<sub>2</sub>O (96 ml)
  2. HCl (4 ml)
  
- **Potassium Ferrocyanide (4% solution)**
  1. Potassium Ferrocyanide (4 gr)
  2. Adjust to 100 ml by dH<sub>2</sub>O
  
- **Potassium ferrocyanide solution, HCl : Potassium Ferrocyanide 4% (1:1)**
  1. HCl (4% solution) (20 ml)
  2. Potassium Ferrocyanide (4% solution) (20 ml)
  
- **Iron-detection reagent**
  1. Ferrozine (6.5 mM)
  2. Neocuproine (6.5 mM)
  3. Ammonium acetate (2.5 M)
  4. Ascorbic acid (1 M)
  5. Dissolved in water (100 ml)